

Dynamic modelling of offshore monopile decommissioning

A study into the first moments of complete removal of monopiles

Diederik Joris Martinus Meijer

Master of Science Thesis - Offshore Engineering



Dynamic modelling of offshore monopile decommissioning

A study into the first moments of complete removal of monopiles

Diederik Joris Martinus Meijer

to obtain the degree of Master of Science
at the Delft University of Technology,
to be defended on Wednesday October 19, 2022 at 13:00 PM.

| | |
|-------------------|---|
| Student number: | 4565649 |
| Project duration: | December 6, 2021 – September 6, 2022 |
| Thesis committee: | Prof. Dr. ² Andrei Metrikine, TU Delft, Chairman |
| | Dr. ir. Bart Ummels, TU Delft, supervisor |
| | ir. Evangelos Kementzetzidis, TU Delft, supervisor |
| | ir. Jan Gruijters, Allseas Engineering group |

An electronic version of this thesis is available at <http://repository.tudelft.nl/>.
Cover page from edf-renouvables [1].

Preface

This master thesis report is the final part of my masters program Offshore and Dredging Engineering at Delft University of Technology. The process of conducting the research in this report has not been without the occasional hurdles, and without the help of my many supervisors, family members and friends I would have despaired long ago. I am happy and proud to have made it this far and would like to thank the following people in particular.

Bart Ummels, my daily supervisor from TU Delft, for your continuous support and attention during the whole process, especially when things got hard. Your decisive way of pointing out what I have achieved and your way of finding the right words for what I wanted to say during the last year will not soon be forgotten. Also from TU Delft, I want to thank professor Metrikine, for your continuous enthusiasm about the project. Your way of drawing conclusions during our meetings has helped me a great deal to scope this thesis the right way and head in the right direction.

Jan Gruijters, from Allseas Engineering, for consistently challenging me to think about modelling techniques and acting as a talking post for when I needed to organise my mind. The many hours spent spouting ideas on a whiteboard will not soon be forgotten, and your urge to be consistent and thorough made me not plagiarize myself, for which I want to express my gratitude. Thank you also for providing me with knowledge about offshore operations and your realistic approach of things.

From Allseas, I want to thank Jeroen Breukels as well, for making time for our weekly meetings even though your attention was almost always required elsewhere during that time. Additionally, Niels Mallon cannot remain unmentioned as you consistently kept on challenging me to try to understand my own models and for 'Nielsing' me from time to time.

Finally, the support that I have received time and time again from my family and friends has helped me through this final part of my student life. Thank you all for your continued love and support along this long journey, I hope to see you soon!

Diederik Joris Martinus Meijer
Delft, October 2022

Abstract

The offshore wind sector in Europe has grown significantly over the past 20 years. Following this surge in number of installations, the first generation of turbines is reaching its end-of-life (EOL) phase and thought needs to be put into end-of-life strategies. As the market for lifetime extension is still in its infancy and re-powering is economically unappealing, decommissioning is the most obvious solution. The tower, Rotor Nacelle Assembly (RNA) and electrical cables will most likely be removed by reverse-installation methods, as well as the Transition Piece (TP). Removal of the monopile foundation however, is considerably more difficult due to the large embedded length of the pile in the soil. The common way of decommissioning such piles in industry (mostly the Oil & Gas (O&G) industry) is to cut them at or below the seabed and leave the remaining stumps in place. This research investigates more sustainable methods that remove the foundation completely, as this is more in line with the modern circular economy and regulations, i.e., OSPAR, are getting more stringent, focusing on complete removal of all offshore structures in the future.

To remove the entire monopile foundation using only a blunt uplift force, tremendous amounts of force are required. It is thus desired to lower this extraction force by some technique to reduce soil resistance. This research investigates the possibility of reducing soil resistance surrounding monopiles by utilizing pitch and heave vessel motions. Such motions can induce an harmonic force on the monopile during the first moments of lifting. The hypothesis is that low frequency oscillations of about 0.1 Hz can induce plastic strain accumulation of the soil, resulting in permanent displacement of the pile. This hypothesis is tested by constructing two models, one describing vessel motion in MATLAB, and the other describing the pile-soil interaction under cyclic loading, which is modelled in the open source software OpenSees. An extensive market study is performed to find a representative maximum set of dimensions of the first generation of monopiles installed offshore. Monopiles with a grouted connection to the transition piece are considered as first generation monopiles, and it is these monopiles that are of interest to the study because they need to be removed the first. The vessel considered in this research is the Pioneering Spirit and the crane its Jacket Lift System (JLS), due its large lifting capacity. After delineating to the monopile size and the vessel, assumptions are made regarding the extraction process. A cranemaster is added to the system to avoid slack in the lines and a connection tool between the crane wire cables and the monopile is selected, assuming a rigid connection between the two.

The results indicate that applying a low frequency cyclic load to a monopile can result in the accumulation of plastic strain of the soil and, consequently, to larger monopile displacements than in monotonic load cases of the same magnitude. In the simulations performed in this research, this effect, called cyclic degradation, is observed to be more intense in sands than in clays. It is observed that plastic strain is largest when large forces are applied to the model, hence it is desired to maximize the combination of tension and amplitude of the applied cyclic force. The effect of cyclic degradation however, is stronger if the forcing frequency is increased to a value near the resonance frequency of the pile-soil system. This value lies in the region of 4 to 8 Hz, depending on the force input characteristics because of the non-linear behavior of soils. Achieving frequency multiplication of the input force has been considered in both active and passive ways. It is concluded that only active frequency multiplication may deliver the needed cyclic degradation, since passive frequency multiplication diminishes the amplitude of the cyclic force, driving up the resonance frequency of the pile-soil system even further. The applicability of the pile-soil model, and thus these conclusions, is only valid during the first moments of lifting, when displacements are relatively small.

The results obtained in this thesis are the result of a relatively conservative soil dynamics model and a non-conservative hydrodynamical model. The reliability of the results could be further improved if the two models are combined in a co-simulation, where at every time-step the pile displacement and vessel motion are determined. Additionally, expanding the OpenSees model so that accurate representations of large pile displacements are included, will allow for calculation of longer simulations, where the pile is completely removed from the soil. The hydrodynamic model can be improved by using an entire sea-state as input.

Contents

| | |
|---|------|
| Abstract | v |
| List of Tables | xi |
| List of Figures | xiii |
| Nomenclature | xvii |
| 1 Introduction | 1 |
| 1.1 Offshore wind | 1 |
| 1.2 Monopile | 2 |
| 1.3 End-Of-Life | 3 |
| 1.4 Allseas Engineering | 6 |
| 1.5 Objective and scope | 6 |
| 1.6 Methodology | 8 |
| 1.7 Thesis structure | 8 |
| 2 Literature study | 9 |
| 2.1 Regulations | 9 |
| 2.1.1 International | 9 |
| 2.1.2 National | 10 |
| 2.2 Economics | 10 |
| 2.3 Current decommissioning methods | 11 |
| 2.3.1 Partial removal | 11 |
| 2.3.1.1 Diamond wire cutting | 11 |
| 2.3.1.2 Abrasive water jet cutting | 12 |
| 2.3.1.3 Other methods | 13 |
| 2.3.2 Complete removal methods | 13 |
| 2.3.2.1 Vibration assisted decommissioning | 13 |
| 2.3.2.2 External and internal dredging | 14 |
| 2.3.2.3 Jetting | 14 |
| 2.3.2.4 Buoyancy lifting | 14 |
| 2.3.2.5 Hydraulic pile extraction | 14 |
| 2.4 Reverse installation methods | 15 |
| 2.4.1 Vibrational installation | 15 |
| 2.4.2 Gentle Driving of Piles | 15 |
| 2.5 Conclusion | 15 |
| 3 Monopile delineations and procedure prerequisites | 17 |
| 3.1 Monopile size delineation | 17 |
| 3.2 JLS to monopile connection | 18 |
| 3.2.1 Balltec lifting solutions | 18 |
| 3.2.2 Righini | 19 |
| 3.3 Avoiding snap loads | 19 |
| 3.3.1 Cranemaster | 19 |
| 3.3.2 Tensioning procedure | 21 |
| 3.4 Conclusion | 21 |
| 4 Monopile extraction forces | 23 |
| 4.1 Soil structure and classification | 23 |
| 4.2 Set-up | 24 |
| 4.3 Plug formation | 25 |

| | | |
|-------|--|----|
| 4.4 | Extraction force | 25 |
| 4.4.1 | Unit skin friction resistance cohesive soils | 27 |
| 4.4.2 | Unit skin friction resistance in sands | 28 |
| 4.4.3 | Monopile and soil plug weight | 29 |
| 4.5 | Load cases | 30 |
| 4.6 | Soil behavior under cyclic loading | 31 |
| 4.6.1 | Non-linearity of soils. | 31 |
| 4.6.2 | Cyclic loading | 31 |
| 4.6.3 | Liquefaction | 32 |
| 4.6.4 | t-z curves | 33 |
| 4.6.5 | Hysteresis | 34 |
| 4.6.6 | Progressive failure | 35 |
| 4.7 | Conclusion | 35 |
| 5 | Vessel Model | 37 |
| 5.1 | Introduction | 37 |
| 5.1.1 | Pioneering Spirit | 38 |
| 5.2 | Model set-up | 39 |
| 5.2.1 | Methodology. | 40 |
| 5.2.2 | Equations of motion | 40 |
| 5.2.3 | Added mass and damping | 41 |
| 5.2.4 | Natural frequency validation. | 42 |
| 5.2.5 | Calibration of forcing terms | 43 |
| 5.3 | Steel cable-wire modelling | 44 |
| 5.3.1 | Steel wire stiffness | 44 |
| 5.3.2 | Steel Wire Damping | 45 |
| 5.4 | Cranemaster | 46 |
| 5.5 | Conclusion | 47 |
| 6 | Pile-soil interface modelling | 49 |
| 6.1 | Modelling pile-soil interaction | 49 |
| 6.1.1 | T-z springs | 50 |
| 6.1.2 | Pile elements. | 51 |
| 6.2 | Integrator types | 52 |
| 6.2.1 | Newmark method | 52 |
| 6.2.2 | Hilber-Hughes-Taylor | 53 |
| 6.2.3 | Generalized- α | 53 |
| 7 | Results and Discussion | 55 |
| 7.1 | Vessel model results. | 55 |
| 7.2 | Hysteresis | 56 |
| 7.3 | Varying amplitude | 56 |
| 7.4 | cyclic vs monotonic load | 57 |
| 7.5 | Varying tension | 58 |
| 7.6 | Resonance frequency | 59 |
| 7.7 | Clay vs Sand. | 60 |
| 7.8 | Discussion | 61 |
| 7.8.1 | Vessel model | 61 |
| 7.8.2 | Soil model | 62 |
| 8 | Conclusion | 65 |
| 9 | Recommendations for further research | 67 |
| 9.1 | General recommendations | 67 |
| 9.2 | Vessel model development | 68 |
| 9.3 | Soil dynamic model development. | 68 |
| 9.4 | Frequency multiplication device | 69 |
| 9.4.1 | Passive systems | 69 |
| 9.4.2 | Active systems | 72 |

| | | |
|-------|--|-----|
| A | Offshore wind farm market analysis of MP and TP dimensions | 75 |
| B | Monopile to transition piece connections | 77 |
| B.1 | Grout connections | 77 |
| B.2 | Bolted connection | 80 |
| B.3 | Slip-joint | 80 |
| B.4 | Integrated TP | 81 |
| B.5 | C1 wedge connection | 82 |
| C | Monopile condition at EOL | 83 |
| C.1 | What does the structural integrity of a monopile look like after design life is reached? | 83 |
| D | AQWA data | 87 |
| E | Vessel model validation and sensitivity analysis | 91 |
| E.1 | RAOs | 91 |
| E.1.1 | The JONSWAP spectrum | 92 |
| E.2 | Response spectrum | 93 |
| E.3 | Fixity effect on added mass and damping | 94 |
| E.3.1 | Pitch and heave data real time lift | 95 |
| E.4 | Sensitivity analysis | 96 |
| F | Resonance frequency | 99 |
| G | Mesh convergence study | 101 |
| H | OpenSees code | 103 |
| H.1 | Vessel model | 103 |
| H.2 | OpenSees model main code | 107 |
| H.3 | MATLAB functions in order of usage of main file for OpenSees model | 108 |
| | Bibliography | 115 |

List of Tables

| | | |
|-----|--|-------|
| 1 | List of abbreviations | xvii |
| 2 | List of symbols | xviii |
| 1.1 | End-Of-Life options for offshore wind turbines [2]. | 4 |
| 1.2 | Previously decommissioned offshore wind farms, prototype projects disregarded [3]. EAWJ stands for External Abrasive Waterjet, IAWJ stands for Internal Abrasive Waterjet. | 5 |
| 1.3 | SWOT analysis of Allseas Engineering Group. | 6 |
| 3.1 | Dimensions and other relevant parameters for the case study monopile used in this research. | 17 |
| 4.1 | Soil type classification by particle size in mm [4]. | 23 |
| 4.2 | Left: Classification of sands per relative density and friction angle [5]. Right: Classification of cohesive soils per undrained shear strength according to ISO 14688-2:2004, 5.3, Table 5 [4]. | 24 |
| 4.3 | Nomenclature soil dynamics [6]. | 26 |
| 4.4 | Input parameter for sand calculations [6–9]. | 28 |
| 4.5 | Partially submerged weight of the case study MP and marine growth. | 30 |
| 4.6 | Submerged weight of soil plug. | 30 |
| 4.7 | Load cases, all units are in MN. | 30 |
| 5.1 | Pioneering Spirit specifications. | 39 |
| 5.2 | Pioneering Spirit parameters used as inputs in the vessel model, including the frequency dependent parameters added mass, hydrodynamic damping and damping ratio. | 42 |
| 5.3 | Pioneering Spirit parameters used as inputs in the vessel model during the natural frequency validation. Frequency dependent parameters added mass, hydrodynamic damping and damping ratios used in the natural frequency validation of the model. | 42 |
| 5.4 | Theoretical and model damped and undamped radial natural frequencies. | 43 |
| 5.5 | JLS main hoist steel wire properties. | 45 |
| 5.6 | Parameters for steel wire stiffness and damping calculations and the damping entered in the model as b_c | 46 |
| 6.1 | Initial tangent vs internal friction angle for sands with extrapolated values [10], and initial tangent with corresponding undrained shear strength for clays [11]. | 50 |
| 6.2 | Elastic beam column command input parameters. | 52 |
| 6.3 | Newmark method input parameters [12] and corresponding names of methods. | 53 |
| 6.4 | HHT input parameters [12]. | 53 |
| 6.5 | Generalized- α method parameters. | 54 |
| A.1 | European offshore wind farm monopile dimensions and parameters for the five largest countries in the offshore wind sector in Europe. Farm capacity less than 50 MW is not considered. Blue = UK, Green = Germany, Orange = Netherlands, Red = Belgium, Yellow = Denmark. BF = Bolted Flange. | 75 |
| A.2 | Table continued, thick line below Humber Gateway shows the boundary between the first and second generation of monopiles as it is assumed in this thesis. | 76 |
| E.1 | Adjusted added mass and damping values for pitch in fixed and free condition. | 95 |
| E.2 | Fast-Fourier-Transform results of Tyra data in Figure E.5. | 96 |
| E.3 | Added mass and damping sensitivity analysis input parameters varying both with $\pm 20\%$. Results are given as the largest amplitude in the resulting crane-master force. | 96 |
| G.1 | Data obtained in mesh convergence study. | 102 |

List of Figures

| | | |
|------|---|----|
| 1.1 | Red line: installed capacity of offshore wind turbines in Europe as of June 2021 [13]. Bars: annual installed capacity in Europe. | 1 |
| 1.2 | Amount of offshore wind turbines reaching 20-years of operation per year in Europe [14]. | 2 |
| 1.3 | Offshore wind turbine components with a monopile foundation [15]. | 2 |
| 1.4 | Common foundation types used for offshore wind turbines [16]. | 3 |
| 1.5 | Flowchart of the decommissioning process of an offshore wind turbine in three stages, orange blocks: preliminary stage, grey blocks: decommissioning stage, green blocks: post-decommissioning stage [17], the blue block highlights the focus of this thesis. | 3 |
| 1.6 | The Jacket Lift System on the Pioneering Spirit with its two beams and six main hoist systems with a capacity of 5000 tons each[18]. The total capacity of the JLS is still 20.000 tons, since not all six main hoist systems can operate at maximum capacity at the same time. | 7 |
| 2.1 | A diamond wire cutter in action. The diamond wire that cuts through the pipe is circulating around the pulleys, creating friction between the diamond particles in the wire and the pile itself [18]. | 12 |
| 2.2 | Abrasive water jet cutters, left: External Abrasive WaterJet cutter (EAWJ), right: Internal Abrasive WaterJet cutter [19]. | 12 |
| 2.3 | Decommissioning methods aiming at complete removal of the foundation as proposed by Hinzmann et al. [20]. | 13 |
| 3.1 | Balltec LiftLOK lifting tool [21]. | 18 |
| 3.2 | F LLI Righine lifting tool [22]. | 19 |
| 3.3 | Example of a 1200 ton cranemaster [23]. | 20 |
| 3.4 | Force vs stroke relation of a 1000t cranemaster [23]. | 20 |
| 3.5 | Force vs stroke speed relation of a 1000t cranemaster [23]. | 20 |
| 3.6 | Slack overlength during the tensioning procedure. The black line represents the motion the JLS beam tip over time which has a period of 10 seconds and amplitude of 0.75 meters. | 21 |
| 4.1 | Two different angles of internal friction in sands, left: high ϕ , right: low ϕ [24]. | 24 |
| 4.2 | Axial shaft resistances in plugged and unplugged scenarios, tensile shaft resistance given for constant skin friction over depth. | 26 |
| 4.3 | Shaft friction resistance in cohesive soils for a) an unplugged pile and b) a plugged pile. | 28 |
| 4.4 | Shaft friction resistance in sands for a) an unplugged pile and b) a plugged pile. | 29 |
| 4.5 | Types of cyclic loading [25]. | 32 |
| 4.6 | Cyclic shaft failure regime overview. Y-axis: amplitude of cyclic loading over ultimate static capacity. X-axis: mean of cyclic loading over ultimate static capacity, N_f is the number of cycles [26]. | 33 |
| 4.7 | A non-linear t-z curve [25]. | 34 |
| 4.8 | Visualization of t-z curve modelling often used in axial pile-soil models [27]. | 34 |
| 4.9 | Hysteresis behavior under one-way cyclic loading. This figure is created with MATLAB with a simplified version of the model. Excitation force is $100\sin(0.1*2\pi t)$ (MN). | 34 |
| 4.10 | Progressive failure along a pile in clay. | 35 |
| 5.1 | Vessel motions overview and definition [28]. | 38 |
| 5.2 | Global coordinate system of the Pioneering Spirit and definition of vessel dimensions. | 38 |
| 5.3 | Schematic overview of vessel model. | 39 |
| 5.4 | The Jacket Lift System on the Pioneering Spirit with its two beams and six main hoist systems with a capacity of 5000 tons each[18]. The total capacity of the JLS is still 20.000 tons, since not all six main hoist systems can operate at maximum capacity at the same time. | 40 |

| | | |
|-----|---|----|
| 5.5 | Example of a motion report for the CoG for a sea state of $H_s = 2.5\text{m}$, $T_z = 6\text{ s}$ | 41 |
| 5.6 | Validation of vessel model by natural frequency check in Heave and Pitch. | 43 |
| 5.7 | Heave and pitch motion simplification in CoG as obtained from a motion report. | 44 |
| 5.8 | Damping and stiffness cranemaster versus stroke length and speed visualized. | 47 |
| 6.1 | Schematic overview of the FEM model that is modelled in OpenSees. | 49 |
| 6.2 | Construction of a t-z element as proposed by Boulanger et al. [29]. | 51 |
| 7.1 | Output of the vessel model in terms of cranemaster force. Together with the ramp-up, the force represented in the right graph serves as the input of the pile-soil model. | 55 |
| 7.2 | Response of OpenSees model to force input of Figure 7.1b, showing hysteresis behavior. | 56 |
| 7.3 | Results of pile-soil model to input force amplitude variation. Top and bottom left figures: applied force versus time, top red line represents the ultimate capacity of the pile equal to 89.1 MN, the bottom red line highlights the maximum applied force, equal to 80.4 MN in all cases. Bottom right: topnode displacement vs number of cycles for all three cases. | 57 |
| 7.4 | Response of model to monotonic load of 80.4 MN with a ramp-up. Left: force measured in top element of pile vs time, right: displacement vs time response. | 58 |
| 7.5 | Results of varying tension and its effect on final displacement of the topnode. Left: example of the input force, with τ_{ult} and tensional part represented by red horizontal lines. Right: topnode displacement vs number of cycles for three different tension forces. | 58 |
| 7.6 | Resonance frequency of the pile-soil model for different input forces, a) constant amplitude and b) arbitrary forces including constant tension of 70 MN. On the y-axis the amplitude of topnode displacement at steady-state is plotted. | 59 |
| 7.7 | Resonance frequency analysis of the pile-soil model for different input forces, a) constant amplitude and b) arbitrary forces including constant tension of 70 MN. On the y-axis the sum of amplitude of force in all soil spring elements is plotted. | 60 |
| 7.8 | Force vs displacement curves showing the difference in response to cyclic loads of clays and sands. In both cases the exact same cyclic load was applied. | 60 |
| 9.1 | Example of a Frequency up-Converter using impact coupling to multiply the input frequency [30]. This type of up-converter is commonly used as a motion energy harvester in a wristwatch. | 70 |
| 9.2 | Force vs displacement graphs showing model response to frequency multiplication and amplitude reduction, | 71 |
| 9.3 | Force vs displacement graph as a result of a sinusoidal input force of the form: $112 + 8\sin(0.52\pi t)$ | 71 |
| 9.4 | Overview of a vibratory hammer [31]. The eccentric masses create the harmonic force and are in this case driven by a hydraulic power unit. | 72 |
| 9.5 | Representation of how rotation of an eccentric mass translates to a cyclic force [31]. | 72 |
| B.1 | Different types of transition piece to monopile connection [32]. | 77 |
| B.2 | Typical grouted MP-TP connection [33]. | 78 |
| B.3 | Shear keys in a grouted TP-MP connection [34]. | 79 |
| B.4 | Double slip joint [35]. | 81 |
| B.5 | C1 Wedge connection between MP and TP [36]. | 82 |
| C.1 | Important zones of MP and TP regarding corrosion [37]. | 84 |
| D.1 | Inertia matrix of PS at a draft of 17 meters. | 87 |
| D.2 | Frequencies as input in AQWA in iterative process, resulting outputs are response frequencies. Coinciding frequencies marked red and taken as natural frequency in that DOE. | 87 |
| D.3 | Frequencies as input in AQWA in iterative process with corresponding critical damping values in percentages. At the natural frequency, critical damping is selected. | 88 |
| D.4 | ANSYS data used to determine the added mass and damping in heave. | 88 |
| D.5 | ANSYS data used to determine the added mass and damping in pitch. | 89 |
| E.1 | RAOs of heave amplitude for wave directions 45, 90, 120 and 150 degrees for both the Centre Of Gravity and the starboard beam tip. | 92 |

| | | |
|-----|--|-----|
| E.2 | Response spectrum at CoG and starboard beam tip for wave directions 45, 90, 120 and 150 degrees. | 93 |
| E.3 | Single significant amplitudes in centre of gravity and beam tip for different wave directions. . . | 94 |
| E.4 | Heave and pitch displacements and velocities of vessel for fixed and free conditions. | 95 |
| E.5 | PS Heave and pitch motion during tensioning procedure of Tyra jacket lift. At around 27 minutes the tensioning starts, ater 32 minutes it is complete and the remainder of the plot is ballasting. . | 96 |
| F.1 | Nodal displacement vs forcing frequency for the topmost node after 50 seconds of simulation. . | 99 |
| G.1 | Force-displacement graphs with varying number of elements used to construct the monopile. Number of elements from top left to bottom right: 10, 100, 200, 500, 1000, 2000. | 101 |
| G.2 | Convergence of topnode displacement and computational time versus number of pile elements. | 102 |

Nomenclature

Table 1: List of abbreviations

| Abbreviation | Description |
|--------------|--|
| API | American Petroleum Institute |
| BEIS | Business, Energy & Industrial strategy |
| CH | Chung and Hulbert integration method |
| CoF | Centre of Floatation |
| DNV | Det Norske Veritas |
| DOF | Degrees Of Freedom |
| EAWJ | External Abrasive Water Jet |
| EIA | Environmental Impact Analysis |
| EOL | End-Of-Life |
| FFT | Fast-Fourier-Transform |
| FLS | Fatigue Limit State |
| GDP | Gentle Driving of Piles |
| GW | GigaWatt |
| HFO | High Frequency Oscillator |
| HHT | Hilber-Hughes-Taylor integration method |
| HKZ | Hollandse Kust Zuid |
| HSE | Health, Safety and Environment |
| HYPE | Hydraulic Pile Extraction |
| IAWJ | Internal Abrasive Water Jet |
| ILT | Internal Lifting Tool |
| JLS | Jacket Lift System |
| IMO | International Maritime Organization |
| ISO | International Standardization Organization |
| LAT | Lowest Astronomical Tide |
| LFO | Low Frequency Oscillator |
| MP | Monopile |
| MN | MegaNewton |
| MW | MegaWatt |
| OWEZ | Offshore Wind farm Egmond aan Zee North-East Atlantic Protection of the |
| OSPAR | Marine Environment convention, name stems from Oslo-Paris agreement |
| O&G | Oil and Gas |
| O&M | Operation and Maintenance |
| PS | Pioneering Spirit |
| RAO | Response Amplitude Operator |
| RNA | Rotor Nacelle Assembly |
| RUL | Remaining Useful Lifetime |
| SWOT | Strengths, Weaknesses, Opportunities & Threats |
| TLS | Topside Lift System |
| TP | Transition Piece |
| ULS | Ultimate Limit State |
| UNCLOS | United Nations Convention on the Law of the Sea |
| WTG | Wind Turbine Generator |

Table 2: List of symbols

| Symbol | Description | Unit |
|----------------|---|------------------|
| ρ_w | Density of water | kg/m^3 |
| g | gravity constant | m/s^2 |
| γ'_{mg} | Submerged unit weight of marine growth | kN/m^3 |
| ρ_{mg} | Density of marine growth | kg/m^3 |
| V_{mg} | Volume of marine growth | m^3 |
| t_{mg} | Thickness marine growth | mm |
| L_{emb} | Embedded pile length | m |
| V_{emb} | Embedded pile volume | m^3 |
| L_{sub} | Submerged pile length | m |
| L_{dry} | Emmersed pile length | m |
| ρ_{st} | Density of S355 steel | kg/m^3 |
| I_{xx} | Pile moment of inertia around x-axis | m^4 |
| I_{yy} | Pile moment of inertia around y-axis | m^4 |
| I_{zz} | Pile moment of inertia around z-axis | m^4 |
| t | Wall thickness | mm |
| R_t | Total resistance force to be overcome | kN |
| $Q_{r,t}$ | Total axial, tensional resistance | kN |
| D_o | Outside diameter of the monopile | m |
| z_s | Depth coordinate downward from the seabed | m |
| L_{fill} | Inside length of the monopile filled with soil | m |
| A_o | Monopile outside area | m^2 |
| A_i | Monopile inside area | m^2 |
| W_{mp} | Monopile weight, partially submerged | kN |
| W_{mg} | Weight of marine growth | kN |
| W_{sp} | Weight of soil plug | kN |
| $f_{o,t}(z)$ | Outside unit skin friction under tension, function of depth | Pa |
| $f_{i,t}(z)$ | Inside unit skin friction under tension, function of depth | Pa |
| $c_u(z)$ | Undrained shear strength at depth z | Pa |
| α | Adhesion factor | - |
| Ψ | Consolidation factor | - |
| $\sigma'_v(z)$ | Effective vertical stress | Pa |
| K_0 | Coefficient of lateral earth pressure at rest | - |
| β | Skin friction factor | - |
| f_{lim} | Limit unit skin friction | Pa |
| D_r | Relative density | - |
| δ | Angle of friction between soil particle and pile shaft | - |
| z_{50} | Displacement at which 50% of the ultimate capacity of the soil is reached | Pa |
| t_{ult} | Ultimate capacity as force, used as input of the t-z elements in OpenSees | N |
| E_s | Initial tangent of t-z curve | N/m^3 |
| t_i^p | Plastic part of force in t-z element at time = i | N |
| t_i^e | Elastic part of force in t-z element at time = i | N |
| z_i^p | Plastic part of displacement of t-z element at time = i | m |
| z_i^e | Elastic part of displacement of t-z element at time = i | m |
| c | Constant controlling the tangent modulus at the start of plastic yielding in OpenSees t-z element | - |
| n | Exponent controlling the sharpness of the $t - z^p$ curve | - |
| C_e | Constant defining the normalized elastic stiffness | - |
| b_{crit} | Critical damping | kg/s v kgm/s |
| ζ | Dimensionless damping coefficient | - |

| | | |
|------------|---|--------------------|
| δ | Logarithmic decrement of damping | - |
| EA_{eff} | Stiffness times effective area of steel wire cables | N |
| L_w | Length of steel wire cable of JLS | m |
| ω_1 | Radial frequency of heave forcing term | rad/s |
| ω_2 | Radial frequency of pitch forcing term | rad/s |
| a_{33} | Heave added mass of vessel | kg |
| a_{55} | Pitch added mass of vessel | kg |
| b_{33} | Heave damping of vessel | kg /s |
| b_{55} | Pitch damping of vessel | kg m/s |
| ω_d | Damped natural frequency | rad/s |
| ω_n | Undamped natural frequency | rad/s |
| c_{33} | Vessel heave stiffness | kg/s ² |
| c_{55} | Vessel pitch stiffness | kgm/s ² |
| z | Vessel heave displacement | m |
| θ | Vessel pitch rotation | rad |
| u | Main hoist vertical displacement | m |
| k_{cm} | Cranemaster stiffness | kg/s ² |
| b_{cm} | Cranemaster damping | kg /s |
| F_a | Amplitude of heave forcing | N |
| M_a | Amplitude of pitch moment | Nm |
| m_h | Mass of main hoist block | kg |

Introduction

1.1. Offshore wind

The Paris Agreement, signed in 2015, is a renowned agreement between 195 countries that signed a treaty to tackle the problem of climate change. It was agreed in this treaty that global warming should be limited to less than two degrees Celsius above pre-industrial levels [38]. To reach this goal, three strategies are to be employed, consisting of the reduction of CO₂ emissions, shift the balance of the global energy mix more toward renewable energy, and increase energy efficiency [39]. In the matter of increasing the share of renewable energy in the global energy mix, the offshore wind industry shows great potential.

The wind industry has seen a rapid growth over the last decades. What started with turbines being placed mainly on land, has shifted towards more and more turbines being placed offshore in the last two decades. This shift is partly explained because the availability of potential onshore wind farm sites is decreasing, and many people regard onshore wind turbines as visual pollution. The shift to offshore wind turbines makes sense when one considers the fact that on sea, the wind energy potential is much larger, and winds are steadier. Following these facts, it is no surprise that the offshore wind energy industry has seen a rapid growth over the last two decades. As can be seen from Figure 1.1, during the last decade alone, installations have surged and the total installed capacity has risen to over 25 Gigawatts (GW) on the European continental shelf [13]. The Dutch government intends to actively pursue the increase in offshore wind energy capacity in the coming decades to realise the climate targets for 2030 and 2050 [38].

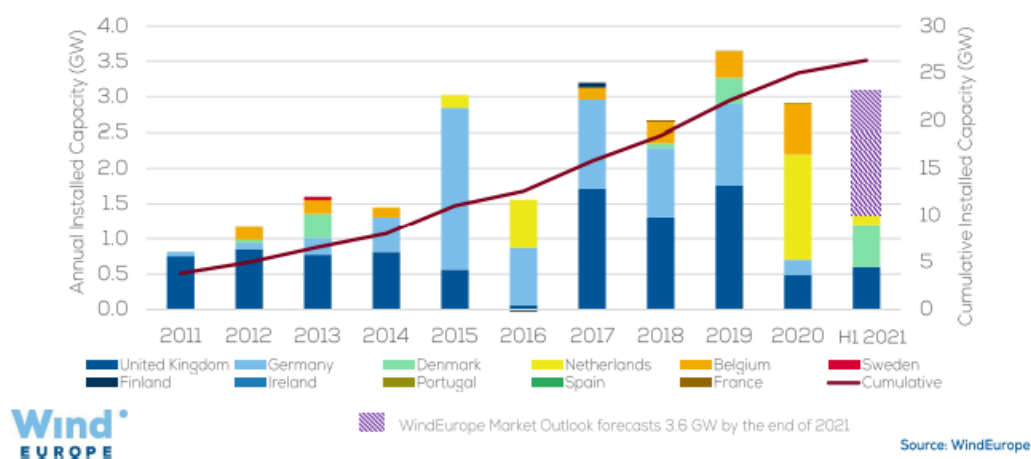


Figure 1.1: Red line: installed capacity of offshore wind turbines in Europe as of June 2021 [13]. Bars: annual installed capacity in Europe.

As the market continues to grow and more and more wind turbines are being installed in ever deeper waters, the North Sea slowly becomes packed with wind turbines. While currently the design life of wind turbines is increasing, with new foundations and inter array cabling being designed for 30 to 40 years, older, first generation turbines have been designed to last for 20 to 25 years [40]. Consequently, these older turbines are reaching their end-of-life (EOL) phase. This can be seen from Figure 1.2, an increasing amount of turbines reaches its 20th year of operation during the coming decade.

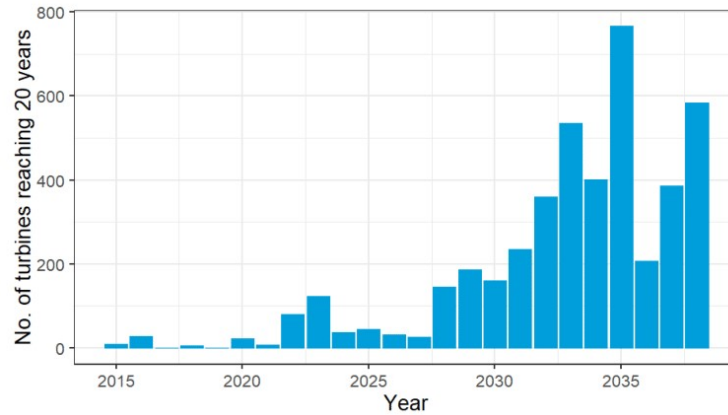


Figure 1.2: Amount of offshore wind turbines reaching 20-years of operation per year in Europe [14].

1.2. Monopile

An offshore wind turbine consists of three main parts, Figure 1.3. There is the Wind Turbine Generator (WTG), which consists of the blades, rotor, nacelle and the tower. The rotor and nacelle combination is often referred to as Rotor Nacelle Assembly (RNA). This part of the wind turbine is concerned with energy production, and only experiences aerodynamic loads. The tower rests on the Transition Piece (TP), connecting it to the foundation. The transition piece consists of several important components, mainly for entering and exiting the turbine for maintenance. It houses among other things, a boat landing, entry ladders, a davit crane used for handling heavy equipment during maintenance, lights and an entry door. Important considerations at the time for having a TP on top of a Monopile (MP) was the requirement of installing secondary steel after installation of the MP itself because the accelerations that occur during installation can damage the secondary steel [41]. Since the grouted connection between the MP and TP, which was frequently utilized in the early years of the offshore wind industry, has a number of drawbacks (Appendix B), in this thesis it is assumed that the TP has been entirely removed before beginning the monopile removal process.

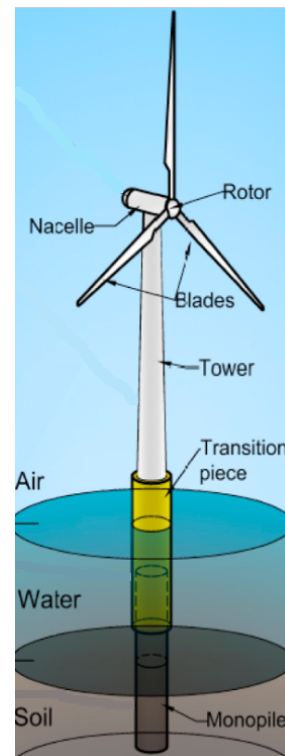


Figure 1.3: Offshore wind turbine components with a monopile foundation [15].

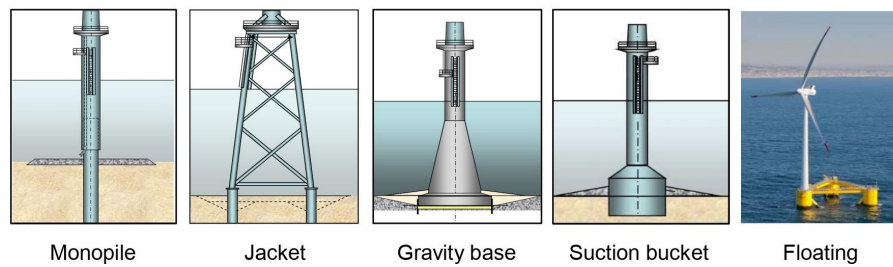


Figure 1.4: Common foundation types used for offshore wind turbines [16].

The transition piece is connected to the foundation, which keeps the structure in place. There are several options for foundation types, the most popular ones being the monopile, jacket, Gravity Based Structure (GBS), suction buckets and floating solutions, Figure 1.4. The monopile has established a dominant position in the market over the last years due to its ease of manufacturability, installation and transportation, resulting in over 80% of all wind turbines utilizing the substructure [42]. While previously it was believed that monopiles were only viable up to water depths of 30 meters, new research and industry experience has shown that the monopile is feasible in water depths of 50 meters [43].

1.3. End-Of-Life

When EOL of a wind farm is reached, the decommissioning phase starts. This process consists of three phases [17], which are visualized in a flowchart in Figure 1.5. Firstly, in the preliminary stage, planning takes place and permits are obtained. During this stage, the different EOL options are explored, financial resources are acquired, and an Environment Impact Assessment (EIA) is made. This is then followed by the decommissioning process itself where the farm is dismantled and transported to shore. The process of decommissioning is most likely to follow a reverse installation process [17], except for the foundation, since reversing foundation installation is not as straightforward. Finally, a monitoring stage follows, where the owner of the farm is obliged to routinely check up on any remaining structures at the site and the conditions of the seabed [44].

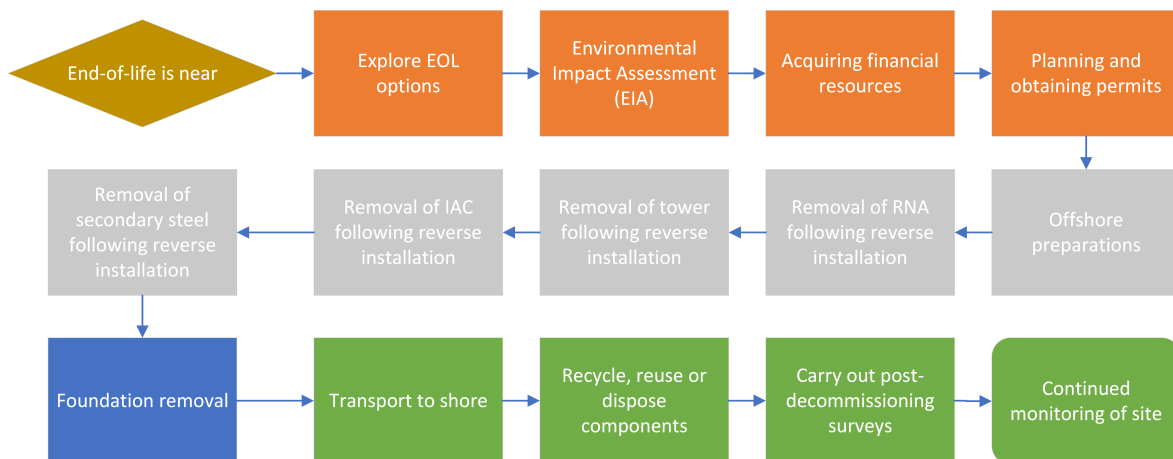


Figure 1.5: Flowchart of the decommissioning process of an offshore wind turbine in three stages, orange blocks: preliminary stage, grey blocks: decommissioning stage, green blocks: post-decommissioning stage [17], the blue block highlights the focus of this thesis.

Before the choice is made to decommission a wind farm, other possible EOL options are investigated. The most common options are shown in Table 1.1. As the offshore wind industry is still relatively new, its focus has mainly been on improving installation techniques and achieving operational efficiency [17]. As a result, EOL strategies have been relatively unattended to, and more research needs to be done to find cost-effective, safe and technical solutions [17].

Table 1.1: End-Of-Life options for offshore wind turbines [2].

| | |
|-----------------------|---|
| Lifetime extension | Extending the operating lifetime of a wind farm, increasing the number of years electricity is produced with the existing turbines, without making significant repairs. |
| (Partial) Re-powering | Removing the tower and RNA and replacing these with (more powerful) newer units, partial repowering is often called refurbishment in literature. |
| Decommissioning | Removing the tower, transition piece and foundation entirely. |
| Alternative use | Look for alternative uses of the remaining foundations (e.g. a fish farm or an artificial reef). |

Lifetime extension

Offshore wind turbine foundations are often designed for longer than 20 years, making lifetime extension a possibility if the tower, RNA and other critical components also offer enough structural integrity [15]. To see if this is feasible, the Remaining Useful Lifetime (RUL) must be determined [2], which is a parameter that quantifies the remaining safe operation time. The RUL can be increased by replacing critical components, but determining the RUL properly is tough as it depends on uncertain factors such as failure rates of critical components [2] and assessing the Fatigue Limit State (FLS) at the end of a turbines lifetime is not an easy job. Apart from these drawbacks, lifetime extension is the most cost effective of the EOL options, as it immediately increases revenue and costs are low compared to other EOL options [45]. Because of the difficulty in assessing the structural state of offshore turbines, lifetime extension is not a popular EOL option, with Vindeby wind farm being the only offshore wind farm whose lifetime was extended, by a period of six years. This could change in the future if good inspection and Operation and Maintenance (O&M) strategies are combined with up to date structural health monitoring systems [45].

Re-powering

There are two different types of re-powering, complete and partial re-powering. In complete re-powering, both the Wind Turbine Generator (WTG) and the foundation are removed and replaced by units with a higher capacity. In partial re-powering, the old WTG is removed and more powerful turbine is placed on the old foundation [44]. Because complete re-powering includes foundation removal, it is considered as decommissioning. By partial repowering, a wind farms lifetime can typically be extended longer than by lifetime extension, which is why operators often first look to re-power ahead of extending the lifetime of a wind farm. Countries with limited availability of offshore wind farm sites like Denmark and Germany tend to lean toward re-powering if possible [2]. Whether re-powering is selected as the EOL strategy depends mainly on regulations and subsidies. The UK market for re-powering for instance, is almost nonexistent, as all subsidies for re-powered wind farms have been terminated. As of 2017, only six European countries include the definition of re-powering in their legislation [13], making it very difficult to obtain permits. Just as is the case for lifetime extension, the market for re-powering remains small as the rapid growth of rated power of turbines makes installing smaller turbines unappealing from a cost-benefit perspective and installing larger turbines on smaller foundations is simply not possible [41]. To the authors knowledge, no large scale re-powering on offshore wind farms has been conducted to date.

Alternative uses

Another option is to not remove the foundations at all and to declare the site a natural reserve. This way the marine life that has accumulated on and around the structure can live in peace without being disturbed by decommissioning and vessel operations. However, current regulations do not allow for leaving the foundations in-situ and operators of wind farms are obliged to restore the seabed to its original condition. Another factor here is that the option for alternative use of foundations is highly site specific and it is difficult to include it in a comprehensive strategy.

Sometimes a combination of the available EOL options is best, and a farm might first be re-powered or its lifetime is extended before decommissioning inevitably comes along [45]. As of 2022, only five offshore wind farms have been decommissioned, Table 1.2.¹

Table 1.2: Previously decommissioned offshore wind farms, prototype projects disregarded [3]. EAWJ stands for External Abrasive Waterjet, IAWJ stands for Internal Abrasive Waterjet.

| Wind farm | Operator | Capacity | Pile diameter (m) | Pile length (m) | Water depth (m) | Removal method | decommissioning date | Cut location w.r.t. seabed (m) |
|------------------------|--|----------|-------------------|-----------------|-----------------|-------------------------------|----------------------|--------------------------------|
| Robin Rigg | E. ON | 2x 3MW | 4.5 | 35 | 30 - 40 | EAWJ | 2015 (2008-2015) | +2 |
| Yttre Stengrund | Vattenfall | 5x 2MW | 3.5 | 34 - 37 | 2-5 | Diamond wire cutting | 2015 (2001-2015) | unknown |
| Lely | Vattenfall | 4x 0.5MW | 3.2 - 3.7 | 26 | 3-4 | Vibratory lifting | 2016 (1994-2014) | no cut |
| Utgrunden | Vattenfall | 7x 1.5MW | 3.0 | 33.7 | 7.1 - 9.9 | IAWJ | 2018 (2000-2018) | unknown |
| Blyth | E. ON, Shell, Vattenfall and Border Wind | 2x 2MW | 3.5 | 33 | 6 - 11 | Hydraulic cylinders, IAWJ cut | 2019 (2000-2019) | -0.5 |

As can be seen from the table, the foundations of wind turbines are often not removed completely, and a cut is made below, at or above the seabed, leaving the remaining foundation in place. Removing the entirety of the foundation yields significant challenges, as will be demonstrated over the remainder of this thesis. The foundations of the Lely wind farm in the IJsselmeer are the only ones that have been removed completely, using a vibratory hammer. Nowadays, permits dictate that the owner of a wind farm restores the seabed to its original state, with some even going further, demanding removal of all elements. The Borssele I & II permit for instance, demands that the permit holder "will dismantle and remove all elements of the wind farm within two years at the latest" [46].

Within the next five to ten years, the demand for decommissioning will increase rapidly and, as Topham et al. [14] conclude, most wind farm contractors, developers, and owners have little to no plan on how to handle the decommissioning process. These two facts make the need for research into decommissioning methods abundantly clear and show that the involved stakeholders need to investigate their options in an EOL scenario. Even though permits require a decommissioning plan, these plans often lack sufficient planning, depth, and adequate financial foresight leading owners to grossly underestimate decommissioning costs. On top of that, after the creation of these plans during the design phase of the project, they often end up on a shelf without being updated while technology advances. This leads to outdated plans from a technical and logistical point of view [47]. The need for a decommissioning strategy is clear but what aspects should be included in such a plan remains the question. Because the decommissioning process itself does not create any revenue, apart from recycling of scrap steel, it is in an owners best interest to find a method that is low-cost and efficient, reducing offshore operational time [16, 47]. As most wind farms nowadays consist of more than 70 wind turbines Table A.1 (Appendix A), it is evident that providing a quick and logistically optimal solution is key [48]. An EOL plan should also aim to minimize risks and be applicable to different conditions like monopile dimensions and soil conditions. On top of that, from a Health, Safety and Environment (HSE) point of view, the plan should aim to reduce impact on the environment and personnel involved in the operation. In order to include all these aspects in a decommissioning plan, adequate planning and anticipation is necessary. Before such a detailed decommissioning plan can be constructed it is of importance to look at the available technical options regarding removal of monopiles.

Research done by Stapel [19], analysed the state-of-the-art decommissioning methods currently being used in the offshore wind industry to remove monopiles, and lessons can be learnt from his findings. After comparing and analysing different removal tools he selected a tool that is mounted on the seabed making use of mud mats, which uses hydraulic cylinders and a hole-beam connection with the MP to remove the latter from the seabed completely. The following specific aspects may be considered challenging to align with the objectives of efficient removal, as they were described above:

1. Mud mat displacement - When extracting the monopile from the seabed, the soil surrounding the monopile can become unstable. This affects the mud mats on which the removal tool is standing, and the tool is likely to sink into the ground askew. The uncertainty and risk of such an event and its consequence is significant.

¹Here only wind farms with a monopile (MP) foundation are considered, gravity based foundations and jackets are disregarded as monopiles make up 80% of foundations in use today [13]

2. Use of hydraulics subsea - Even though a bio-degradable lubricant such as glycol [49] is to be used, the use of hydraulics below the water is sub-optimal. Spillage is always a big risk, especially if the operation is to be carried out in frequent succession, and hefty fines are imposed in such an event [50, 51].
3. Logistics - The immersion of the tool and the numerous amount of times the tool needs to drill a hole in the MP and insert a beam makes it a time consuming process and it is unlikely that the method is able to carry out decommissioning at a fast enough pace to be commercially viable.

All in all, these aspects make the proposed method inefficient and logistically challenging. An important finding is that complete removal using blunt force is incredibly difficult to achieve with any existing vessel currently on the market. Consequently, reducing soil resistance in any way possible is not only desirable but necessary to achieve decommissioning in a feasible matter. This thesis will thus investigate ways to reduce this resistance.

1.4. Allseas Engineering

This graduation project is carried out at TU Delft and for Allseas Engineering Group. Allseas is one of the major offshore pipelay and subsea construction companies in the world. Over the last decade they have entered the offshore Oil and Gas (O&G) decommissioning market by removing topsides using their Topside Lift System (TLS) on board of their specialized Pioneering Spirit (PS) vessel. Updating the vessel, it is now fit to also remove jackets using the Jacket Lift System (JLS). A high-level Strengths, Weaknesses, Opportunities and Threats (SWOT) analysis of Allseas is made to illustrate the possibilities for Allseas to enter the decommissioning market in the offshore wind industry. In the table the term day-rate is used, which is the price of chartering a vessel for a single day.

Table 1.3: SWOT analysis of Allseas Engineering Group.

| | Strengths | Weaknesses |
|----------|---|---|
| Internal | <ul style="list-style-type: none"> Fleet with heavy lifting capacity Significant experience in Offshore Operations Innovation minded In-house engineering & Building own equipment | <ul style="list-style-type: none"> Expensive vessels, high day-rates Limited applicability of ships to wind Limited experience in offshore wind sector |
| | Opportunities | Threats |
| External | <ul style="list-style-type: none"> Increase in decommissioning demand Increase in dimensions & Weight of monopiles Early decommissioning of some farms leading to quicker growth of decommissioning market than expected | <ul style="list-style-type: none"> Demand for low cost decommissioning solution Low cost competitors Re-powering or lifetime extension |

The main challenge for Allseas to enter the offshore wind market is the size of their vessels and subsequently their high day-rates. This calls for efficient and fast solutions, that are widely applicable to different types of wind farms.

1.5. Objective and scope

The objective of this thesis is to explore and model possible ways to completely decommission monopiles and investigate the possibility of reducing the soil resistance surrounding monopiles by making use of vessel motion. The response of a volume of soil to cyclic loading (i.e. loading where the magnitude of the force changes over time in a harmonic pattern) is different from its response to monotonic loading. Since vessel motion is often described by harmonics, the force that comes from wave oscillations is also a harmonic and can be categorized as cyclic loading. A model between a monopile and a floating vessel will be made to study the interaction between the harmonic motion of the vessel and the response of soils to the cyclic load that the motion causes. The following main research objective describes the essence of the research:

"Developing a dynamical interaction model between the Pioneering Spirit and a monopile describing the first moments of a complete removal, with an emphasis on soil-resistance reduction by utilizing vessel movement."

To this end the following sub-questions/objectives will be answered:

1. What does a monopile to be decommissioned look like?

2. What static forces need to be overcome to remove the monopile?
3. How can the vessel motions be modelled?
4. How can the pile-soil interface be modelled?
5. What are the key dynamic parameters in the vessel-pile-soil model that influence the reduction in ultimate capacity due to cyclic loading?

Each of these sub-questions will be addressed in a separate chapter of the following work. In order to limit the research to realistic proportions, the following scope is defined.

As a first delineation, the choice to look only at monopiles is made, as during the last decade the monopile has become the industry standard, with 80% of Wind Turbine Generators employing the foundation. On top of this, the Pioneering Spirit is selected as the vessel. This vessel has one of the (if not) largest lifting capacities in the world and if decommissioning MPs with this vessel is not possible, it will not be possible with the proposed procedure with any other vessel.

Secondly, it is assumed that all parts located above the monopile itself are removed. The WTG components, consisting of rotor blades, nacelle, hub, tower and subsea cables have already been removed prior to the start of monopile removal. The Transition Piece, access platforms and any J-tubes have also been removed, leaving only the monopile and scour protection in place. The WTG components are most likely to be decommissioned following a reverse installation method, where the installation vessel will most probably be used to remove these components in the reverse order as during installation [44]. The focus of the study is on grouted MP-TP connections that have been cut-off, as this type of connection is mostly used in the first generation of offshore wind turbines and these MPs are the first to be decommissioned in the coming years. For more information on MP-TP connections and reasoning behind the choice to look at first generations monopiles, reference is made to Appendix B.

As a third delineation, it is assumed that the connection between the monopile and the crane is rigid, meaning that no slip can occur and displacements of one of the components result in an immediate and equal displacement of the other. On top of this delineation, it is assumed that during the proposed procedure, all lifting connections can withstand all involved forces. It is thus assumed that the structural integrity of all involved components remains intact. The last delineation consists of the assumption that horizontal motions of the monopile are relatively small, since the embedded length of the pile is long and almost constant during the first seconds of lifting. This large embedded length ensures that there is little to no horizontal motion of the monopile in the soil and consequently, horizontal motion of the pile during the extraction process will not be considered.

Finally, the vessel that will be used in this research is the Pioneering Spirit, Figure 1.6, since the 20.000 ton lifting capacity of its JLS is one of the only cranes in the world that has a chance to overcome the enormous resistance forces involved in complete monopile removal. Even though the TLS has a larger lifting capacity, the JLS is selected for the procedure, as it allows for an easier connection to monopiles because of its main hoist block, Figure 1.6, and the fact that it can achieve much larger vertical displacements than the TLS because it is fitted with steel wire cables and winches.



Figure 1.6: The Jacket Lift System on the Pioneering Spirit with its two beams and six main hoist systems with a capacity of 5000 tons each[18]. The total capacity of the JLS is still 20.000 tons, since not all six main hoist systems can operate at maximum capacity at the same time.

1.6. Methodology

To find answers to the main research objective and questions, the following methodology will be followed. Firstly, extensive market research is performed, to get a feel for typical monopiles that are to be decommissioned in the following years. Secondly, the static ultimate capacity (i.e. the force that keeps the pile in place) is determined. Then two models are built, one describing the monopile in the soil and its behavior under loading, the other describing the vessels motion and a force that is exerted on the monopile. The monopile is modelled in the open source geotechnical Finite Element Method (FEM) software, OpenSees. This software is selected because of the convenient way it is able to describe the path-dependent response of soils to cyclic loading. OpenSees operates using the .tcl language from regular text files, but in this thesis it is operated from MATLAB, to allow for easy parametrization. The hydrodynamic model is built in MATLAB, representing the vessel and its response to excitation. The model is calibrated by Allseas data on the movement of the PS, called motion reports, as well as the Response Amplitude Operators (RAOs). The vessel model consists of mass-spring-damper elements that are fixed to the monopile, which at that moment in time is still rigidly attached to the ground. The output of the vessel model is a force that is representative for this fixed condition. This output force is then used as an input for the soil model in OpenSees. This means that the two models will be run separately, meaning that no co-simulation and information exchange between the two models occurs during the simulation.

The choice for MATLAB as the vessel model is threefold. Firstly, MATLAB is very powerful at modelling mass-spring-damper models with its ode45 function and running parametrizations (i.e. running the model with different sets of inputs) is easy. Secondly, the OpenSees model is driven from MATLAB as well and modelling both in the same software results in better compatibility. Finally, Allseas has scores of readily available MATLAB files containing data and describing behavior of the PS, making MATLAB the obvious choice.

1.7. Thesis structure

This section lists a clear overview of what the structure of this thesis to provide a clear understanding of what is discussed in which chapter.

Chapter 1. Introduces the offshore wind market and the problem statement of this research. The research questions are presented as well as the methodology and a short introduction of the company.

Chapter 2. State-of-the-art of the wind turbine decommissioning market, discusses the economical and legislative motivators for decommissioning, as well as the available techniques in industry to remove monopiles.

Chapter 3. Further defines the scope, makes delineations on the decommissioning procedure, and presents the case study used in this research.

Chapter 4. A theoretical background on soil behavior under cyclic and monotonic loading and basic calculations determining the ultimate static capacity of monopiles.

Chapter 5. Discusses the theory behind the vessel model, providing the reader with knowledge to understand the build-up of the model.

Chapter 6. Goes into the OpenSees soil model, discussing the general layout of the model and calibrations of parameters. Also discusses some of the possible numerical integrators available in OpenSees.

Chapter 7. Results and discussion.

Chapter 8. Conclusions.

Chapter 9. Recommendations and delineations

The chapters in this thesis are kept as brief as possible to provide the reader with the most essential information to understand the methods used and interpret the results and conclusion. Extensive background information on decommissioning of monopiles, industry standards, MATLAB and OpenSees codes and other informative but non-vital information for such an understanding is provided in the appendices.

2

Literature study

This chapter addresses the state-of-the-art of the offshore wind decommissioning sector. It provides the reader more background information surrounding decommissioning in a non-technical way.

2.1. Regulations

There are numerous international and national organisations offering binding and non-binding guidelines regarding offshore wind farm decommissioning. This section discusses the authorities in play in offshore wind farm decommissioning, the guidelines and frameworks they prescribe and how much they are complied with by wind farm operators and owners. From a legislative point of view, the most important aspect for this thesis is whether or not piles should be removed entirely or can be cut and removed partly which will consequently be the focus of this paragraph.

2.1.1. International

Internationally, sea conventions do not have great authority to enforce their own regulations, limiting their effectiveness [52]. Nevertheless, they are of importance, since national governmental bodies often base national regulations on these types of conventions. The most important parties for the North Sea are:

- United Nations Convention on the Law of the Sea (UNCLOS)
- International Maritime Organization (IMO)
- Convention for the Protection of the Marine Environment of the North-East Atlantic (or OSPAR, which stands for Oslo - Paris)

UNCLOS

The leading international convention providing regulation regarding matters at sea is the United Nations Convention on the Law of the Sea (UNCLOS). The top five key players in the offshore wind sector in Europe, consisting of the UK, Germany, The Netherlands, Belgium and Denmark, have all agreed to the UNCLOS mandates [53]. UNCLOS is the closest to an international regulatory framework as one can get and in article 60 of the 1985 convention, mention is made of the obligation to remove installations or structures which are abandoned [54]. The specific text states:

"Any installations or structures that are abandoned or disused shall be removed to ensure safety of navigation, taking into account any generally accepted international standards established in this regard by the competent international organization. Such removal shall also have due regard to fishing, the protection of the marine environment and the rights and duties of other States. Appropriate publicity shall be given to the depth, position and dimensions of any installations or structures not entirely removed [54]."

International Maritime Organization

The IMO gives more clear and defined guidance regarding the removal of offshore installations on the continental shelf. The IMO counts 175 member states and their 1989 report recommends that the affiliated countries take the guidelines it prescribes into account. Concerning decommissioning of offshore structures, it

states that structures installed after the 1st of January 1998, weighing less than 4000 tons in air and standing in less than 100-meters water depth should be entirely removed unless one of the following exemptions is applicable [55]:

1. The structure can serve a new use.
2. The structure can be left there without causing unjustifiable interference with other uses of the sea.
3. Removing the structure entirely would involve extreme cost, technical in-feasibility, or an unacceptable risk to personnel or the marine environment.

From Table A.1 in Appendix A, it is obvious that all to date installed monopiles weigh less than 4000 tons in air and do not stand in water depths larger than 100 meters, meaning they should be removed as far as the IMO is concerned. The first exemption does not apply on the basis that cut-off stumps in the seabed do not serve anyone any use and the second because of the fact that the site becomes inoperable for future offshore wind farms, burning one's own fingers as a sustainable engineering company. The third argument is the hardest to refute as the costs and the technical feasibility of complete removal are uncertain and up for debate, and permit holders often invoke this as an argument to remove partly rather than completely [56–59].

Convention for the Protection of the Marine Environment of the North-East Atlantic

OSPAR aims to assist operators in the North-East Atlantic to identify potential harmful environmental cts that offshore operations might have [60]. Its regulations are based on the UNCLOS and IMO guidelines but is legally binding for the signatories. On the disposal of disused offshore installations it states that leaving disused installations in place is prohibited if they weigh less than 10.000 tons in air [61]. On top of that, a trend can be seen where their regulations are getting more stringent, pushing for complete removal of all offshore structures [62].

2.1.2. National

As mentioned before, national governments often base legislation on the previously discussed international organisations. Governments enforce this legislation by specifying permit contents, asking for decommissioning programmes and asking owners to come up with bank guarantees with the purpose of financing decommissioning in the final stages of the farms lifetime [41]. In the UK for example, a final version of a decommissioning report must be delivered to the department for Business, Energy & Industrial Strategy (BEIS), no less than six months in advance of construction, and its standard "should not fall below that of the IMO" [63]. The department also states that the exception due to extreme costs is not normally considered acceptable when it is the sole reason being cited for partial decommissioning [63]. Topham et al. [17] found however, that most submitted programmes are simplistic and underestimate costs. In the article, the absence of a clear regulatory framework counts as one of the four main challenges of decommissioning offshore wind farms in the near future [14]. Of the other top five countries in the offshore wind sector, only the Netherlands and Denmark ask for a bank guarantee [64]. The Belgian government has not adopted specific regulations regarding decommissioning, due to the considerable uncertainties involved in the issue [64].

2.2. Economics

The economics of offshore wind farms mainly revolve around production, installation, and maintenance, as these practices create revenue for its owners and developers. Little attention is paid to the removal of wind farms because it occurs a long way down the road, and it is expected that removal techniques improve significantly over the lifetime of a farm. This has a negative effect on the cost estimation of the decommissioning process, as costs are massively underestimated [16] and these higher costs are especially unwelcome since the farm has stopped generating revenue when the decommissioning stage commences. As Kaiser [65] rightfully mentions, time spent on offshore operations in general should be kept at a minimum to reduce costs, risks and to increase operationability. To achieve all these goals, the number of offshore operations should be kept at a minimum and removal should aim at removal of the whole structure at once, maximizing onshore disassembly rather than offshore disassembly [65]. It is thus in all stakeholders' best interest to decommission and transport the foundations of a wind farm as complete and fast as possible.

[16], [41] Note that costs are also deliberately underestimated by permit holders because the permit warrants them to set aside funds for decommissioning during the operational phase of a farm to make sure they do not face problems with payment during the decommissioning phase. In the UK, savings are obliged to start

during the early or middle part of the operational phase, in the Netherlands this is even earlier, starting from the first year of operation and for at least ten years [66]. For instance, in the Borssele I & II permit it is stated that the owner must put forward a bank guarantee of 120.000 € per MW, and these savings shall commence before proof of electricity is obtained [46]. This value shall also be raised by 1-2% annually to account for indexing. In the case of Windpark Fryslân, the bank guarantee had to be increased each month in accordance with the anticipated parallel increase of costs for removal, as to ensure that at any time of construction the project could be decommissioned [41]. This means that owners have to account for reservations in their bookkeeping, retaining them from using that money for other projects and increasing overall project costs. In order to show this financial availability, owners must first conduct an analysis of the decommissioning costs and this cost is often underestimated to keep these required savings at a minimum. Not only is this undervaluation of costs harmful for the economics of the business case, but it also refrains stakeholders from being stimulated to reduce the cost of decommissioning, something they would be very willing to do if costs were estimated properly. Other factors that make decommissioning of wind farms a business clouded in uncertainty is its dependence on (future) vessel day-rates, which are highly dependent on the current market prices of, e.g. fuel and personnel [16]. Still, it is clear that the future costs of decommissioning are getting increased attention from governments and project owners.

Lastly, an important note is made by Smith [16] who notes that in the oil and gas industry, it is the norm to go for partial removal rather than complete removal, and most decommissioning reports do not even consider complete removal. For offshore wind farms, the sheer amount of scrap steel that would be left in-situ can even be an argument to opt for complete removal, as the embedded length of a monopile often accounts for more than half of the total length, see Table A.1 in Appendix A. With the current price for scrap steel surging to 350 euros per ton [67], removing the complete foundation rather than cutting and removing partly seems interesting. It must be noted, however, that with high costs of vessels, offshore equipment and personnel, it would not appear likely that there will be a business case for decommissioning - minimization of economic costs will be the sole focus.

2.3. Current decommissioning methods

The current decommissioning methods for monopiles can be split into two parts, those used for partial removal of monopiles and those used in complete removal. As was discussed earlier, all but one wind farm have been partially removed by cutting, with the exclusion of Lely wind farms complete removal by a vibratory hammer. Firstly, the state-of-the-art cutting methods will be discussed, and secondly, complete removal concepts are considered.

2.3.1. Partial removal

In the Oil and Gas (O&G) decommissioning industry, two main cutting techniques are often used to cut jacket legs or other steel structures that need to be disconnected before the structure can be lifted. Those techniques are diamond wire cutting, which can only be applied externally, and Abrasive Water Jet cutting, which can be used Internally (IAWJ) or Externally (EAWJ). There are other options, like using shear cutting and explosives to disconnect structures, but those are not used as much as the others for reasons that will be explained in the following section. All cutting techniques require preparations of the pile section to be cut, including marine growth and coral removal, and marking of the cut section, which may result in an increase in offshore operational time [68].

2.3.1.1. Diamond wire cutting

In diamond wire cutting, Figure 2.1, the cut is a consequence of friction build up between the wire and the monopile and almost no vibrations occur, pollution is low and the method is cost-effective. Due to it only being applicable as an external cutting method, good access to the cutting area is necessary to make a cut [17], meaning that dredging of soil surrounding the pile is necessary if a cut below the seabed is desired. Another downside of external cutting is that it has a limited operational depth because of the fact that the dredging/excavating tool has an operational limit below which the accuracy decreases. On top of that, the marine environment is influenced as you remove a lot of sand, and, even less desirable, diver operations are more likely in external cutting operations [69]. Consequently, external cutting is predominantly used in shallow waters [69]. Despite these downsides, Topham et al. expect [17] diamond wire saw cutting will be the preferred cutting technique in the future "as piles should not be too complicated to wrap around, it is economical, and there is little marine disruption."



Figure 2.1: A diamond wire cutter in action. The diamond wire that cuts through the pipe is circulating around the pulleys, creating friction between the diamond particles in the wire and the pile itself [18].

2.3.1.2. Abrasive water jet cutting

In Abrasive Water Jet (AWJ) cutting an abrasive is added to a high velocity water jet to cut through the monopile. Abrasive water jet cutting can be applied both internally, and externally, allowing for a more versatile approach during the cutting operation, leading to shorter preparation times because of lower dredging volumes. It is more expensive than diamond wire cutting and the addition of abrasive particles makes it a less environmentally friendly option as these particles fly off into the surrounding water. Another downside of abrasive water jet cutting is that it is a relatively slow method with the cutting process taking up to 30 hours in the case of the Amrumbank offshore met mast which had a diameter of 2.8 meters at the cut location [70]. During this last project the cutting tool was not properly aligned resulting in the necessity of a second cut, increasing operation time by 4 hours. They did, however, use a relatively environmental friendly abrasive made up mainly of Almandine. The company RGL, which specializes in AWJ cutting tools for offshore operations, is able to cut piles of up to 4 meters in diameter while DECO company has cut piles up to 3 meter diameter and claims to have designed a cutter for use up to 10 meters diameter. In 2014 the maximum diameter for Internal Abrasive Waterjet (IAWJ) Cutting was only 2.3 meters, showing a significant increase in recent years [58].



Figure 2.2: Abrasive water jet cutters, left: External Abrasive WaterJet cutter (EAWJ), right: Internal Abrasive WaterJet cutter [19].

2.3.1.3. Other methods

In the onshore cutting industry, shear cutting is regularly used as an alternative to the above mentioned methods. It is a very fast, non polluting method, but the equipment has not yet been designed for the offshore industry, is expensive, has not yet been used in vertical structures, and has not been designed for the large dimensions of monopiles [71]. On top of that, scaling this method is more difficult than the aforementioned options [71]. A fourth cutting method that will not be discussed here is making use of explosives to cut the monopile, as it disturbs the environment a great deal and a long time of planning is necessary to ensure safe operation.

The newest XXL monopiles can reach diameters up to 10 meters [44]. Comparing this to the 2 meter diameter piles of jackets used in the oil and gas sector [41], it becomes obvious that the existing cutting technologies must be developed further in order to be able to cut these large monopiles. All the downsides discussed in this section can be avoided, simply by switching to complete removal.

2.3.2. Complete removal methods

Figure 2.3 shows an overview of available methods to achieve complete removal of monopile foundations as proposed by Hinzmann et al. [20]. These do not comprise all available methods but mentions all methods that are currently being looked into and are at a technology readiness level that allows it to be implemented in the coming five to ten years. In this figure, the following methods are visualized; I: Removal by monotonic load, without reduction of soil resistance, II: Removal aided by resistance reduction using high-frequency vibrations, III: Resistance reduction using internal dredging, IV: reduction by high-pressure water jetting along the monopile sides, V: reduction by overpressure of water inside the pile and finally VI: reduction by overpressure of air inside the pile. These will be elaborated upon in the following sections.

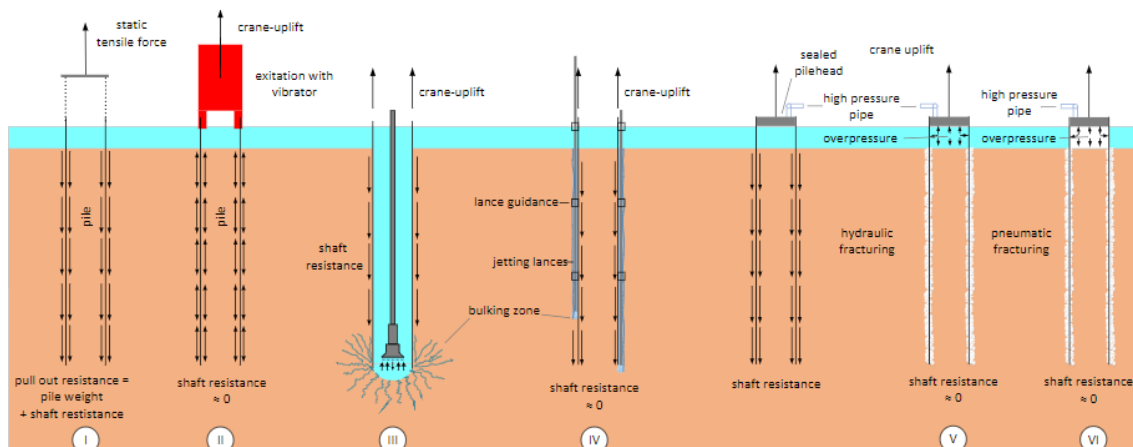


Figure 2.3: Decommissioning methods aiming at complete removal of the foundation as proposed by Hinzmann et al. [20].

2.3.2.1. Vibration assisted decommissioning

Using vibration techniques to decommission monopiles, is one of the most promising techniques according to Hinzmann et al. [69]. By vibrating the pile, the shear resistance of the pile-soil interface is reduced and consequently, the ultimate capacity of the soil diminished. An elaboration on the exact behavior of soils under vibrational (or cyclic) loads can be found in chapter 4. Vibration assisted lifting techniques have been used by Cabboi et al. [72] to remove the tower of a wind turbine that was connected to the monopile using a slip-joint. Electric shakers placed on the inside of the tower excite the tower locally at its first natural frequency, which was determined with a numerical FEM model and compared to field hammer tests and modal analyses. Hydraulic jacks were used to lift the tower initially, a crane then transported the tower onto a barge. The first circumferential shell modes, characterizing the dynamic of the slip joint was identified and during the decommissioning process excited. Vibratory lifting was also used during decommissioning of Lely windfarm and. Although Dieseko Group used their most heavy vibratory equipment for the job, it showed potential for scale-up [44]. CAPE HOLLAND decommissioning is also testing a vibratory removal method. They have already removed a slip joint test pile at the Princess Amalia wind farm two times in 2018, and then removed it

completely in 2021. Vibratory lifting also shows great potential from a noise pollution point of view, as noise emissions stay below 140 dB, well below the threshold of the North Sea of 160 dB at 750 meters of the source [46].

2.3.2.2. External and internal dredging

An obvious solution to reducing soil resistance of monopiles during the extraction procedure, is removing the soil altogether. This can be done both externally, or internally on the soil plug. While this sounds like a good option for soil resistance reduction, in practice, the amount of soil that would need to be excavated is large, and the extraction of one monopile would already be time-consuming. In the decommissioning report of the UK wind farm Greater Gabbard, it is estimated that the excavation hole increases by two meters in diameter for every meter of dredging depth [57], resulting in a hole with a diameter of 70 meters for the 35 meter embedded piles. During the decommissioning of a complete wind farm, about 50 to 100 monopiles will have to be decommissioned, which makes this method inefficient from an operationability point of view. Dredging can be combined with other methods such as jetting and vibratory lifting, making it interesting to keep researching the method.

2.3.2.3. Jetting

A promising method of installation being developed by GBM works is reducing soil resistance around a monopile using water jets [69]. By jetting water along the side of the pile both internally and externally, the soil particles lose their structure and connection to the monopile resulting in a reduction of shear force, which in turn reduces the required uplift force to completely remove the pile. The proposed method by GBM is to be faster, and more silent than conventional installation methods and demonstrations have shown that deeper and faster penetration can be achieved using the method [73]. GBM plans to have the installation method operational in 2025 [73]. Jetting can also be used in partial removal, to reduce the uplift force on the small part of the monopile that is embedded in the seabed.

2.3.2.4. Buoyancy lifting

Another method of lifting a submerged structure is by creating a buoyant force that is exerted on the structure [69]. This can be achieved by submerging deflated bags and attaching these to the structure below the waterline. Inflating the bags then creates the necessary buoyant force to lift the structure.

Several problems arise for the application of this method to monopiles. Firstly, as will be calculated in the following chapters, the forces involved in complete monopile removal are simply too large to be overcome by buoyancy alone. Secondly, while buoyancy assisted decommissioning in jackets has potential, it shows less promise to the application of monopiles as the possibilities of connecting the buoyant bags to the structure are lower. The outsides of a monopile are flat, and smoothly curved, leaving little to points of attachment for a buoyant bag. Because of these limitations, buoyant decommissioning can at the most only be used as a secondary, assisting method, in addition to a primary method of decommissioning.

2.3.2.5. Hydraulic pile extraction

Another method is to close all holes and gaps by installing a pile cap on the top of the monopile, fill the pile with water, and put the inside under pressure [69]. Increasing the pressure yields a pushing force against the pile cap (top) and the bottom, creating an upward driving force. A crane can help to overcome any additional pile resistance. A project that aims to do exactly this, is the Hydraulic Pyle Extraction-Scale Tests (HyPE-ST) project, a project that is carried out by the GROW consortium, which is now testing at meso-scale. The costs of decommissioning using this method should be lower, as the required cranes and vessels can be smaller and time spent offshore is lower than in conventional methods [74]. Recent tests at scale 1:20 and 1:30 for an eight meter diameter monopile, where four different soil conditions were investigated being medium dense sand, dense sand, medium stiff clay and layered soil, tested the technique and gathered data on extraction pressure, flow, pile displacement, pore-water pressure and plug displacement. The tests showed promising results and proved the concept at lab scale. Key takeaways from the tests are that the breakout pressure is highly dependent on the soil type and layout surrounding the monopile [74]. Especially when low permeable soil is present inside the pile, breakout pressure surges and can become problematic. The consortium concluded that additional tests and research are necessary before full scale tests can commence. On the positive side, the tests demonstrated that complete removal is possible almost completely silent and with little to no impact on the seabed.

2.4. Reverse installation methods

Looking at installation methods can be of interest for thinking of new decommissioning methods. The conventional way of installing monopiles, both on- and offshore, is hydraulic pile driving, also called hammering [75]. During this hammering, a great deal of noise is generated which causes harm to surrounding fish and mammals. A study by Kikuchi [76] found that at the source point of sound, noise emissions can reach over 210 dB. On top of that, the spectrum of these noise emission is broad-banded, meaning that a lot of frequencies are present. Consequently, these sound emissions are harmful to all types of mammals and fish. It is hard to make use of hydraulic pile driving in the decommissioning of monopiles, hence this section focuses on more environmentally friendly and promising installation methods from a decommissioning point of view. Another installation method that is hard to reverse into a decommissioning method is blue piling. Blue piling is an installation method devised by IHC IQIP and TU Delft, aiming to reduce noise pollution. Large water masses are accelerated over a long period of time, creating a pushing force on the monopile. This way, pile accelerations are kept at a minimum and noise reduction of 20 decibels is achieved compared to conventional hammer installation methods. Blue piling will also not be considered in the following section.

2.4.1. Vibrational installation

Vibratory pile driving is an existing technique and an approved method for pile and vertical plate installation onshore [69] and it shows great promise regarding noise mitigation. A hammer is rigidly fixed to the top of the pile and this hammer contains 2 or more eccentric masses. Rotation of these masses results in excitation of the pile and ultimately motion of the pile. In vibratory pile driving the shear resistance of the soil is reduced by constant up and down motion of the pile. This way a state of soil liquefaction is reached because the soil loses particle structure and shaft resistance tends toward zero. The remaining required lifting power is just the (submerged) weight of the pile and the hammer. More information of the behavior of soils under cyclic loads follows in chapter 4.

2.4.2. Gentle Driving of Piles

The Gentle Driving of Piles (GDP) project is another project undertaken by the GROW consortium which commenced in 2018. It aims to improve drivability and reduce noise emissions and driving loads during installation of the next generation, XXL monopiles [77]. The newly designed shaker for the project makes use of simultaneous low and high frequency vibrations, exciting monopiles in two different modes at once. Offshore operation time can be reduced and costs kept at a minimum because expensive and time consuming noise mitigation methods are redundant. Another important goal of the GDP project is to ensure that the method still produces the necessary soil bearing capacity in order for the monopile to be able to resist all environmental forces over its lifetime. After promising results were achieved in lab tests, a larger scale field test commenced at Maasvlakte II [77]. Now that testing at Maasvlakte II is finished, three main findings can be identified [78]:

1. The stiffness of the soil against installations is much higher in the GDP case than for the regular installation cases which were also done, namely installation via vibrational hammer and impact hammers.
2. The GDP method needs more energy than normal installation methods. Because of this a new shaker is being designed as the energy would become prohibitive at full scale.
3. The single frequencies that were expected from the shaker, are not observed in real life testing. There are also a lot of high (unexpected) harmonics induced during piling.

The lessons learnt from the project are significant for the continuation of the GDP project. After the GDP numerical models have been updated and verified, and parametric analysis of the obtained data has been carried out, the most important geotechnical and structural parameters for the GDP installation method can be identified. Understanding what parameters limit and govern the pile and the soil surrounding it during the GDP process will generate better understanding and this way, the GROW consortium is able to improve the technology in the future. The GDP method is expected to commence full scale testing in 2025.

2.5. Conclusion

This chapter has discussed the state-of-the-art of the offshore wind decommissioning industry. The main considerations surrounding complete and partial removal from a legislation point of view have been considered, and it can be concluded that while regulations are leaning toward complete removal, it is not yet

mandatory to do so since the numerous international regulatory frameworks are non-binding. On a national level, permits oblige wind farm developers and operators to decommission either completely or partly if it can be argued that complete removal is infeasible from a technical or financial point of view. The latter is done on a case-by-case basis. Regarding economics, it has been demonstrated that costs of decommissioning projects are deliberately underestimated so that owners do not have to set aside large funds meant for decommissioning. Current decommissioning methods to remove foundations partly have been discussed and the most used cutters in industry, consisting of the abrasive water jet and diamond wire cutter, considered. Complete removal methods for monopiles are still in their infancy and no large-scale method has been demonstrated to work at this moment. The most promising methods consist of vibration assisted decommissioning, jetting and hydraulic pile extraction. For the remainder of this thesis the focus will be on using vibrations to assist in complete removal of monopiles. More specifically, low frequency oscillations originating from vessel motion will be researched, as this is a novel topic of study and a research gap in literature exists.

3

Monopile delineations and procedure prerequisites

This chapter aims to answer the first sub-question: "What does a monopile to be decommissioned look like?". The chapter will firstly look at the geometry and main components of WTGs and present a case study, based on a worst-case scenario. Afterwards, possible connections tools to connect the cables to the monopile are considered and lastly, snap loads are discussed as well as methods on how these can be avoided.

3.1. Monopile size delineation

In order to estimate the key technical parameters of monopiles to be decommissioned in the next decade, an extensive market study of all currently installed offshore monopiles in Europe has been performed, Appendix A. When studying the table in Appendix A, it stands out that there is a certain distinction to be made in the way transition pieces are connected to monopiles. The first generation of offshore monopiles used grout to connect these two components, where the second and latest generation mostly use a bolted flange connection. An elaboration on the available MP-TP connection types and their advantages and disadvantages can be found in Appendix B. This appendix also explains the shift in industry from grouted to bolted connections. Because the first generation of monopiles is almost at the end of its lifetime, grouted connections will be the scope of this study. From an operational point of view, it is assumed that the TP has been removed from the MP, leaving only the open-ended monopile in place.

Table 3.1 presents the parameters of the case study monopile that will be used in this research from this point onward. The dimensions have been selected by looking at all monopile dimensions up to 2016 and selecting the largest values, in a worst-case scenario type of approach. The result is a conservative representative monopile for the first generation of monopiles so that if the proposed solution in this thesis works, it works on all first generation monopiles. Gemini, Gode wind 1 & 2, Dudgeon and Rentel wind farm have been excluded from this selection, as they are considered second generation wind farms, with a monopile length and diameter that lie consistently far away from the mean. The exact definition of second generation monopiles is undefined but size, connection method to TP and weight play a large role in the choice of classification.

Table 3.1: Dimensions and other relevant parameters for the case study monopile used in this research.

| | Value | Symbol | Unit |
|--------------------|-------|-------------|----------|
| Length | 75 | L_{mp} | m |
| Embedded length | 40 | L_{emb} | m |
| Outer diameter | 6.5 | $D_{o,t}$ | m |
| Wall thickness | 80 | t_{mp} | mm |
| Weight | 930 | W_{mp} | t |
| Density S355 steel | 7800 | ρ_{st} | kg/m^3 |

The length, embedded length, and outer diameter have been selected from Table 3.1 as the maximum occurring value. The wall thickness is determined by the American Petroleum Institute (API) standard, shown in Equation 3.1.

$$t = 6.35 + \frac{D_{o,t}}{100} \quad (3.1)$$

Where: t = wall thickness in millimeters
 $D_{o,t}$ = the outer diameter in millimeters

The wall thickness is rounded up from 71,35 to 80 mm to account for safety factors and corrosion, but still stay close to the worst-case principle. Elaboration on corrosion assumptions and calculations can be found in Appendix C. The weight of the monopile is then calculated and then checked with data from Appendix A to verify the result. Equations for monopile weight are elaborated on in chapter 4.

Only homogeneous soil layers will be considered in this thesis. Although in-situ heterogeneous soil conditions are often encountered, calculating extraction forces for the most dense soils will yield the most extreme extraction forces. By not considering different soil layers, the model is kept as generic as possible, not treading into a detailed location for just one wind farm. This is done to keep the model widely applicable, as taking a certain heterogeneous soil configuration as a case study would make the model less generally applicable. The effects of heterogeneous soil layer configurations on pile extraction are left for further research.

3.2. JLS to monopile connection

At the moment of writing, no connection tool between a monopile and crane hoist block that is able to withstand 200 MegaNewtons (MN) exists. This section investigates what connection tools are available in industry, and makes an estimation of the possibility to scale up those tools. Due to the large forces involved, the choice is made to look into Internal Lifting Tools (ILTs) rather than external clamping tools, as this would risk buckling of the pile. Other external connection tools, such as grommets, fall outside the scope of this research. The state-of-the-art ILT types are listed in the following sections.

3.2.1. Balltec lifting solutions

Balltec Lifting Solutions delivers lifting tools that minimise human intervention in critical operations from a safety point of view (e.g. the need for divers or working at heights). Their liftLOK tool is available for lifting capacities up to 3000 tons but can, according to them, be scaled up limitlessly. It utilizes a ball and taper gripping mechanism, which procedure is simple, to transfer the lifting force from the crane to the monopile, the tool is lowered inside the monopile and the balls are pushed out to partly deform the monopile, creating friction. Custom built LiftLOK tools can be manufactured upon request to suit project specific requirements. An advantage of this tool is that it has a fail-safe mechanism that only allows it to release under a zero-load condition. An example of the LiftLOK tool is shown in Figure 3.1. When the diameter of the pile increases, the number of balls in the tool also increases, inherently scaling up the lifting capacity of the tool. By tweaking the tools length, the desired uplift capacity can be acquired.



Figure 3.1: Balltec LiftLOK lifting tool [21].

3.2.2. Righini

The hydraulically operated ILT by Righini, Figure 3.2, has a vertical lifting capacity of 4000 tons in air [22]. The working principle is partly the same as for the Balltec solution, with the only difference being the extension of the black pads in Figure 3.2 creating the lifting capacity rather than balls. Just like the LiftLOK, scaling up the lifting capacity of this technology is also inherent with scaling its dimension. It is noted by the author that both these lifting tools are not designed for the dynamic interaction proposed in this research, and that considerable design modifications must be made to ensure safe operations. Nonetheless, a firm and rigid connection between the pile and crane is assumed for now, as the goal of this thesis is not design oriented.



Figure 3.2: F. LLI Righine lifting tool [22].

3.3. Avoiding snap loads

The nature of this thesis is to reduce soil resistance forces on monopiles utilizing harmonic vessel motion, therefore, relatively large vessel motions are desired and a rough sea state suits the operation better than a calm one. These conditions can lead to large crane tip motions in the vertical direction (heave) as will be shown in chapter 5. Because the pile is fixed with respect to the earth, these motions of the crane tip can cause the main hoist wires to go slack, because steel wires can only carry tensional forces, not compressive ones. Slack wires are especially undesired in offshore heavy lift operations, as they can give rise to large snap loads when the load suddenly falls down and re-tensions the wires. On top of that, the wires can also become entangled, endangering the safety of the operation. If the momentum of the load is large enough this can damage the wires, crane or the load itself and, in a worst-case scenario, the wires break and the load is lost. To prevent slack wires and make sure that the hoist wire always remains under tension, a cranemaster is added to the system, as well as a pre-tensioning procedure.

3.3.1. Cranemaster

This application calls for some allowance of vessel motion to be passed onto the pile head to apply a harmonic force. As will be shown in chapter 5 and Appendix E, the motion of the beam tip of the JLS in vertical direction has a significant amplitude of 0.75 meters. The elasticity of the steel wire cables of the JLS allow for about half a meter of strain but, since the wire is delayed by 20 falls, this results in only 0.025 meters of displacement of the lower main hoist block. This is not enough to make sure that the wires remain under tension and a second component is introduced, a cranemaster. A cranemaster is a passive heave compensation system, often used to diminish motions of loads with respect to vessel motion. The goal of the cranemaster in this case is to reduce the probability of slack wires and entanglement of the lines while still passing on the harmonic nature of the load pattern. Cranemasters come in all sorts and sizes and a 1000 ton system will be used and scaled as a case study for this thesis. The 1000 ton cranemaster is scaled to a 5000 ton unit, which is used six times, one for each main hoist block of the JLS beams. The 1000 ton unit has a weight of 50 tons, meaning that the total cranemaster weight used comes to 1500 tons if scaled linearly. A picture of a cranemaster in operation is provided in Figure 3.3. Another positive aspect of using a cranemaster is the fact that the stiffness and damping parameters can be selected arbitrarily. This way, the amplitude of the force that the cranemaster exerts on the monopile can be varied.



Figure 3.3: Example of a 1200 ton cranesmaster [23].

This table shows the upward force the cranesmaster exerts on the load for a specific stroke length, as well as a dampening force for a specific stroke speed. The data is visualized in Figure 3.4 and Figure 3.5 and with the help of these figures, the path-dependent cranesmaster force is determined in the model.

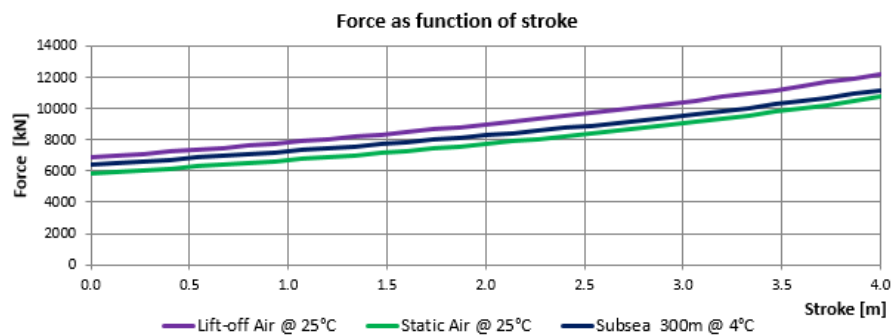


Figure 3.4: Force vs stroke relation of a 1000t cranesmaster [23].

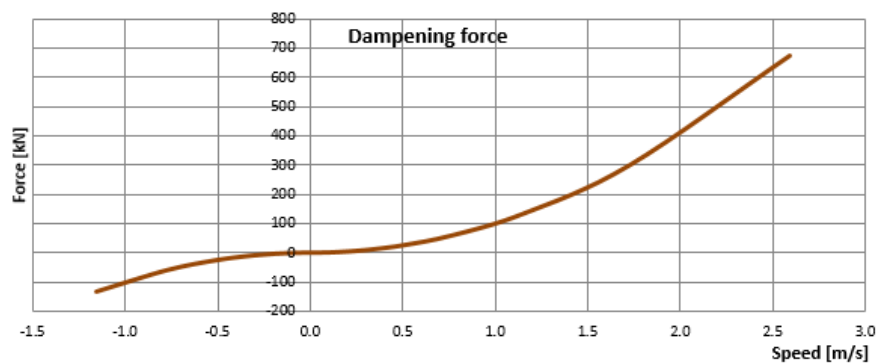


Figure 3.5: Force vs stroke speed relation of a 1000t cranesmaster [23].

3.3.2. Tensioning procedure

The cranemaster acts as a rigid element if the force on the monopile is below the force at a stroke of 0 in Figure 3.4 multiplied by the amount of cranemaster units that are used in the system. To avoid snap loads during the period of time where this force is not yet reached the following tensioning procedure is proposed.

From the vessel model that is constructed later in this thesis, it is known that the maximum vertical motion of the beam tip is 1.5 meters which occurs during an oscillation with a period of 10 seconds. The winches in the JLS beams that are responsible for retrieving the wire of the main hoist, operate at a maximum speed of 60 meters per minute. Because the wires consist of 20 falls, the main hoist block moves vertically with a speed of 3 meters per minute. This means that during one wave period, the cables can be retrieved by half a meter. At the start of the procedure, the wires are hanging slack and have an overlength of 1 meter so that all preparations can be carried out. This means that a vertical distance of 2.5 meters must be bridged when going from the slack to the tension case. The situation is sketched in Figure 3.6.

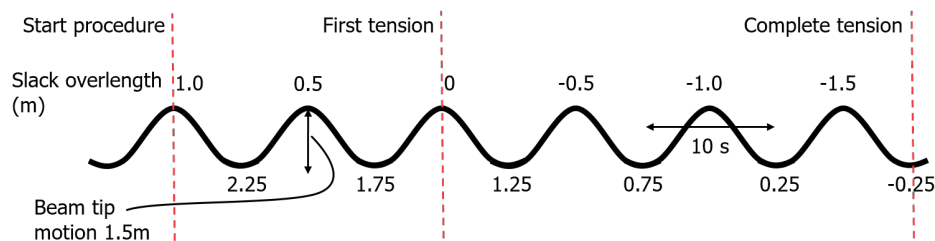


Figure 3.6: Slack overlength during the tensioning procedure. The black line represents the motion the JLS beam tip over time which has a period of 10 seconds and amplitude of 0.75 meters.

It can be observed from Figure 3.6 that it takes approximately 5.5 wave periods for the JLS winches to completely tension the cables and that during the tensioning procedure, the cables transition from slack to tension four times. Although this sounds like a problem, reality is much more forgiving than the conservative approach presented here because of the following reasons. Firstly, the 1.5 meter oscillation of the beam that is taken, is the 3-hour maximum motion of the beam tip, which means that it only occurs once every 3 hours. Taking a constant harmonic motion of 1.5 meters amplitude is therefore an extremely conservative approach. Secondly, the cables and JLS beams themselves are not rigid but behave elastically. This way, they also absorb some of the displacement of the beam tip. For example, if the JLS operates at half capacity (i.e. 10.000 tons), the wire cables give way 0.2 meters. Thirdly, at a certain moment in time in the later stage of the procedure, the force in the cranemaster will exceed its activation force and it will extend, absorbing the dynamic forces.

3.4. Conclusion

In this chapter the technical dimensions of the representative monopile have been defined using data obtained from extensive market research. A setup for monopile removal has been presented consisting of a rigid connection between the JLS cables and the monopile, as well as methods to avoid snap loads. The latter is achieved by implementing a cranemaster between the cables of the JLS and the monopile, which should, in combination with the proposed tensioning procedure, ensure that the steel wire ropes remain under tension at any moment during the decommissioning procedure.

4

Monopile extraction forces

This sub-question relates almost solely to soil dynamics. As mentioned in chapter 1, the embedded length of the monopile is quite large, the soil friction along the shaft will be significantly larger than the hydrodynamic and wind loads acting on the pile. The latter actions are thus disregarded, also based on the assumption that they exert mostly horizontal forces on the pile, rather than vertical forces.

4.1. Soil structure and classification

A volume of soil consists of grains, as well as pore water in the spaces between those grains. Most offshore soil conditions in shallow waters (up to 100 meters water depth) can be categorized in four soil types by their grain size. Table 4.1 shows the classification of soil types by their size according to the International Organization for Standardisation (ISO) standard ISO-14688-1 [4], which will be used in this research. A disparity between non-cohesive and cohesive soils is made because of their difference in behavior when monopiles are installed or extracted from the soil. For the remainder of this thesis, non-cohesive soils, consisting of sands, will be referred to as sands. Cohesive soils, consisting of clays and silts, will be referred to as cohesive soils. Even though sandy clays and silty sands also exist, these types of soil have not been considered in this research. The representative parameters of both types of soil that will be used for the remainder of this work are shown in Table 4.2.

Table 4.1: Soil type classification by particle size in mm [4].

| | Soil type | particle diameter (mm) |
|--------------|-----------|------------------------|
| Cohesive | Clay | < 0.002 |
| | Silt | 0.002 - 0.063 |
| Non-cohesive | Sand | 0.063 - 2.0 |
| | Gravel | 2.0 - 63.0 |

Sands, or non-cohesive soils, are characterised by their frictional properties. They fall apart without the presence of an external force to keep them together, like a wall or a barrier. This can best be imagined by a pile of marbles. The pile will collapse when there is no external force keeping them together. The most important geotechnical parameter for sands is the angle of internal friction ϕ and the relative density. The angle of internal friction dictates up to what angle the pile of marbles is able to support itself under the force of gravity and usually lies between 25 and 40 degrees [6], see Figure 4.1 and Table 4.2.

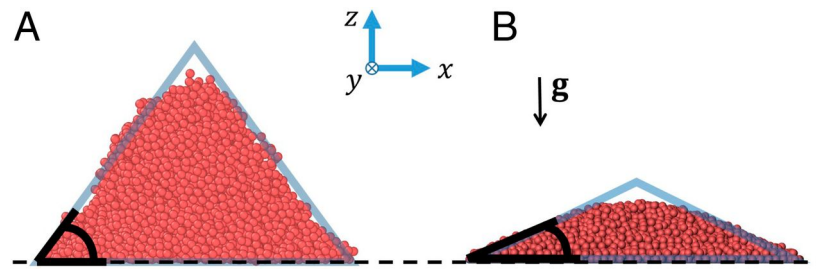


Figure 4.1: Two different angles of internal friction in sands, left: high ϕ , right: low ϕ [24].

Cohesive soils, consisting of clays and silts (and rocks), tend to adhere to themselves. In this type of soil, either cementing is present (in rock) or internal electrostatic forces exist between particles (clay). Logically, due to these internal forces, cohesive soils do not need external forces to stick together. Cohesive soils are best compared with butter. They are sticky and without an external force they keep together effectively by presence of internal forces and thus an external force is necessary to disintegrate the material [6]. The most important parameter in cohesive soils is the cohesive shear strength, $c_u(z)$, which completely determines the strength of the soil since theoretically, the angle of internal friction is 0. In Table 4.2, a range of values is shown for undrained shear strength of cohesive soil. In calculations, the middle value of each range is taken and for very hard clays, the largest value of the last range is taken into account as well.

Table 4.2: Left: Classification of sands per relative density and friction angle [5]. Right: Classification of cohesive soils per undrained shear strength according to ISO 14688-2:2004, 5.3, Table 5 [4].

| Sands | | | Cohesive soils | |
|------------|----------------------|----------------------------|----------------|----------------|
| Soil type | Relative density (%) | Friction angle, ϕ (°) | Soil type | $c_u(z)$ (kPa) |
| Very loose | < 20 | < 30 | Very soft | 10 - 20 |
| Loose | 20 - 40 | 30 - 35 | Soft | 20 - 40 |
| Compact | 40 - 60 | 35 - 40 | Firm | 40 - 75.0 |
| Dense | 60 - 80 | 40 - 45 | Stiff | 75 - 150 |
| Very dense | > 80 | > 45 | Hard | 150 - 300 |
| | | | Very hard | >300.0 |

Apart from grain size, pore water in between the spaces of the grains also play a large role in the behavior of soils to loads. The soil grains are a factor more compressible than the pore water, making the pore water resist an applied load first. When applying a load to a volume of soil, two scenarios can occur. In the first, where permeability, k , is low, the pore water is not able to flow away quick enough and the load is supported by the pore water, which is called the undrained condition. In the second scenario, where permeability is sufficiently high, the pore water is able to flow away and the load is carried by the internal grain stresses in the soil. This is called the drained condition. The undrained condition is unstable as the existing pressure gradient eventually forces the water out and the soil behaves as drained. During this process, the load is transferred from the pore water to the grains, and this is called consolidation; consolidation occurs in both sand and clay but at different time rates. This is how settlement is created, by draining the pore water from the soil, the volume of the soil is reduced. Overconsolidation is when a soil was subjected to large pressures in the past but is not anymore and has since been unable to expand after the pressure is removed. This results in the consolidation and internal stresses to be higher than one might expect from observing soil conditions. An example is that of a molten glacier, which has had an impact on the soil beneath, compacting it, but has melted away.

4.2. Set-up

It has been observed in industry that the bearing capacity (i.e. the amount of shear a pile can withstand without failure of the soil occurring) of a monopile at the end of its lifetime, is not the same as shortly after installation. This effect, named set-up, is most notable during the first days after installation but the effects continue for a longer period of time. When a pile is installed, the soil surrounding the pile fails gradually

as the pile treads deeper into the soil and this causes the End Of Initial Driving (EOID) shaft capacity to be lower than the design shaft capacity [79]. Shaft capacity is the part of a piles bearing capacity originating from soil friction between the soil and the pile its side interface. After installation, the soil settles and the bearing capacity increases. This effect is often attributed to thixotropy and pore pressure dissipation [80]. Thixotropy is an effect where materials that are viscous under static conditions flow over time when undergoing a (shear) stress. Pore pressure dissipation is the same as the earlier discussed consolidation. Other authors attribute the set-up effect to "the relaxation with time of a circumferential arching stress field, increasing the radial stresses developed on the shaft" [79]. Jardine et al. [79] found that the shaft capacity increased to more than double the value measured at EOID for dense sands. [81] Gavin et al. found that set-up appears to be independent of diameter and slenderness ratio (L/D). In clays, the time it takes for shaft capacity to return to the design value can be up to one year [82].

It must be noted that most, if not all field-experiments and research concerning set-up has been conducted for slender piles with small diameters compared to monopiles used in the offshore wind industry. While the effect of set-up is uncertain, knowledge of this subject is imperative for a safe and efficient decommissioning strategy for monopiles.

4.3. Plug formation

During installation of a monopile, soil is pushed into the open-ended bottom of the pile. Upon removal of the pile, this soil can either stay attached to the inside of pile or fall out and exert a frictional force on the inside of the pile, called skin friction. In the first, plugged scenario, the weight of the soil plug inside the monopile has to be accounted for in the load case. In the second, unplugged scenario, the inside skin friction that the soil imposes on the monopile has to be accounted for in the load case.

While some authors do not expect a pile plug to form in large diameter piles such as monopiles because of the large distance such a plug would have to span [69], in industry, there is a lot of uncertainty and debate regarding the matter. Even if a plug has not formed during installation, it can still form during the operational phase of the monopile by static loading [83], because of the absence of inertia of the soil column during this phase [84]. Other factors that influence plug formation are penetration depth [83], relative density of the soil [83], pile diameter [84], and pile velocity/acceleration during decommissioning [84]. Karlowski et al. [84] found that in sands, plugging is most likely to occur in dense sands, as these soils generally cause high internal shaft resistances.

Another factor adding to the uncertainty of plug formation upon monopile removal is that all previously performed experiments and field tests have been carried out for small piles of up to 2 meters in diameter. To the authors knowledge, no field tests or experiments have been carried out on large diameter monopiles. A more recent study by Chen et al. [85], made use of a numerical model of a 5 meter diameter monopile modelled in ABAQUS to investigate plug formation in large diameter, open-ended piles. One of the conclusions of their work was that plug formation is unlikely to occur in cohesive soils¹, but partial plug formation occurs in non-cohesive soils, particularly sands². This research however, looked into plug formation during installation, not decommissioning.

4.4. Extraction force

The following sections use notations and equations from the offshore handbook by Vugts [6], a nomenclature for this particular section is listed here in Table 4.3 for ease of reading.

¹the model used an undrained shear strength of 28 kPa

²An angle of internal friction of 36° was used

Table 4.3: Nomenclature soil dynamics [6].

| Symbol | Description | Unit |
|----------------|---|----------|
| t | Wall thickness | mm |
| R_t | Total resistance force to be overcome | kN |
| $Q_{r,t}$ | Total axial, tensile resistance | kN |
| $Q_{f_o,t}$ | Outside friction resistance | kN |
| $Q_{f_i,t}$ | Inside friction resistance | kN |
| D_o | Outside diameter of the monopile | m |
| z | Depth coordinate downward from the seabed | m |
| L_{emb} | Embedded length | m |
| L_{fill} | Inside length of the monopile filled with soil | m |
| A_o | Monopile outside area | m^2 |
| A_i | Monopile inside area | m^2 |
| W_{mp} | Monopile weight, partially submerged | kN |
| W_{mg} | Weight of marine growth | kN |
| W_{sp} | Weight of soil plug | kN |
| $f_{o,t}(z)$ | Outside unit skin friction under tension, function of depth | kPa |
| $f_{i,t}(z)$ | Inside unit skin friction under tension, function of depth | kPa |
| $c_u(z)$ | Undrained shear strength at depth z | kPa |
| ϕ | Internal angle of friction | $^\circ$ |
| α | Adhesion factor | - |
| Ψ | Consolidation factor | - |
| $\sigma'_v(z)$ | Effective vertical stress | kPa |
| K_0 | Coefficient of lateral earth pressure at rest | - |
| β | Skin friction factor | - |
| f_{lim} | Limiting unit skin friction | kPa |
| D_r | Relative density | - |
| δ | Angle of friction between soil particle and pile shaft | - |

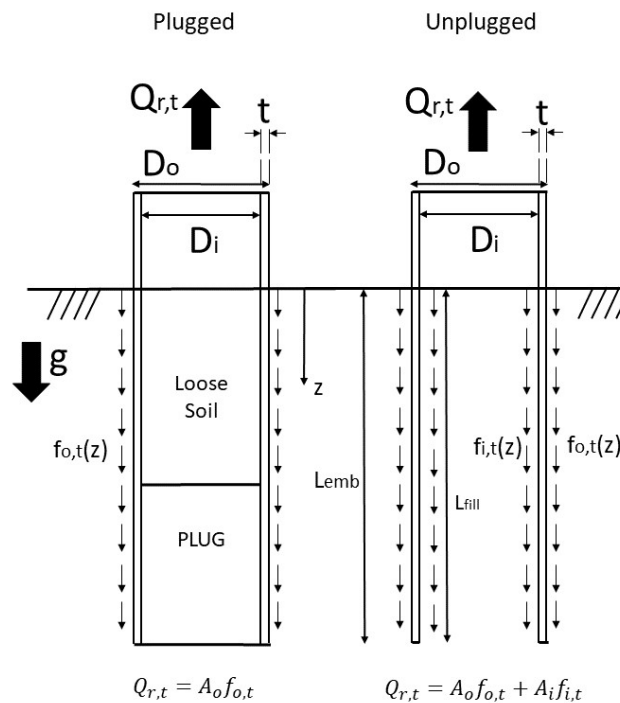


Figure 4.2: Axial shaft resistances in plugged and unplugged scenarios, tensile shaft resistance given for constant skin friction over depth.

Assuming that monopiles are open-ended, steel, tubular pipes with large diameters, the extraction force necessary to overcome the soil resistance is calculated in this section. For complete removal, the following resistances need to be overcome in order to extract the pile from the seabed.

- Axial shaft resistance, or shaft capacity, which varies with the soil type and density/hardness, soil unit weight etc.
- Weight of monopile, partially submerged, including submerged weight of marine growth.
- Submerged weight of pile plug, varying with soil type, density/hardness, soil weight, etc.

These forces are illustrated in Figure 4.2, where a distinction is made between a plugged and an unplugged scenario. In both the plugged and unplugged situation it is assumed that the inside of the monopile is completely filled with soil, leading to $L_{fill} = L_{emb}$. The total extraction force necessary to completely remove a monopile is shown in Equation 4.1

$$\begin{aligned} R_{t,plug} &= Q_{f_o,t} + W_{mp} + W_{mg} + W_{sp} \\ R_{t,unplug} &= Q_{f_o,t} + Q_{f_i,t} + W_{mp} + W_{mg} \end{aligned} \quad (4.1)$$

The pile shaft resistance under tension, $Q_{f,t}$ in Equation 4.2, represents the frictional force that a soil exerts on both the inside and the outside of the pile surface, when a tensional load is applied to the pile. It consists of the area of the pile multiplied by the soil's unit skin friction, which is dependent on soil type, submerged unit weight of the soil and depth, Equation 4.2. There is no distinction between the inside unit skin friction, $f_{i,t}$, and the outside unit skin friction, $f_{o,t}$, meaning that the top equation in Equation 4.2 only differs from the bottom one because it uses D_o rather than D_i [6]. The unit skin friction resistance is dependent on soil type and the next section discusses and calculates the value for sands and cohesive soils.

$$\begin{aligned} Q_{f_o,t} &= \pi D_o \int_0^{L_{emb}} f_{o,t}(z) dz \\ Q_{f_i,t} &= \pi D_i \int_0^{L_{emb}} f_{o,t}(z) dz \end{aligned} \quad (4.2)$$

4.4.1. Unit skin friction resistance cohesive soils

For cohesive soils the unit skin friction resistance is caused by adhesion between the soil particles and the monopile shaft. The API-RP-2A-WSD design standard for the design of offshore structures [7] prescribes the following equation to obtain the unit skin friction resistance Equation 4.3.

$$f(z) = \alpha c_u(z) \quad (4.3)$$

The adhesion factor, α , is dependent on the undrained shear strength, soil submerged unit weight, and the effective depth, and is defined as shown in Equation 4.4.

$$\alpha = \begin{cases} 0.5 \Psi^{-0.5}, & \text{for } \Psi \leq 1.0 \\ 0.5 \Psi^{-0.25}, & \text{for } \Psi > 1.0 \end{cases} \quad (4.4)$$

The consolidation factor, Ψ , is determined by Equation 4.5.

$$\Psi = c_u(z) / \sigma'_v(z) \quad (4.5)$$

Where: $\sigma'_v(z) = \gamma'_s z$ = effective vertical stress
 γ'_s = soil submerged unit weight, a value of 10 kN/m^3 is used.

The total shaft resistance can now be calculated using Equation 4.6 for the unplugged scenario, and Equation 4.7 for the plugged scenario, where e equals -0.5 or -0.25, depending on the value of Ψ in Equation 4.4.

$$\begin{aligned}
Q_{f_{o,t}} + Q_{f_{i,t}} &= \pi (D_0 + D_i) \int_0^{L_{emb}} f_{o,i}(z) dz \\
&= \pi (D_0 + D_i) \int_0^{L_{emb}} \alpha c_u(z) dz \\
&= \pi (D_0 + D_i) \int_0^{L_{emb}} 0.5 \left(\frac{c_u(z)}{\gamma'_s z} \right)^\epsilon dz \quad (4.6)
\end{aligned}
\qquad
\begin{aligned}
Q_{f_{o,t}} &= \pi D_o \int_0^{L_{emb}} f_o(z) dz \\
&= \pi D_o \int_0^{L_{emb}} \alpha c_u(z) dz \\
&= \pi D_o \int_0^{L_{emb}} 0.5 \left(\frac{c_u(z)}{\gamma'_s z} \right)^\epsilon dz \quad (4.7)
\end{aligned}$$

Plotting these formulas in Python yields the following graph, showing the total shaft friction vs embedment length.

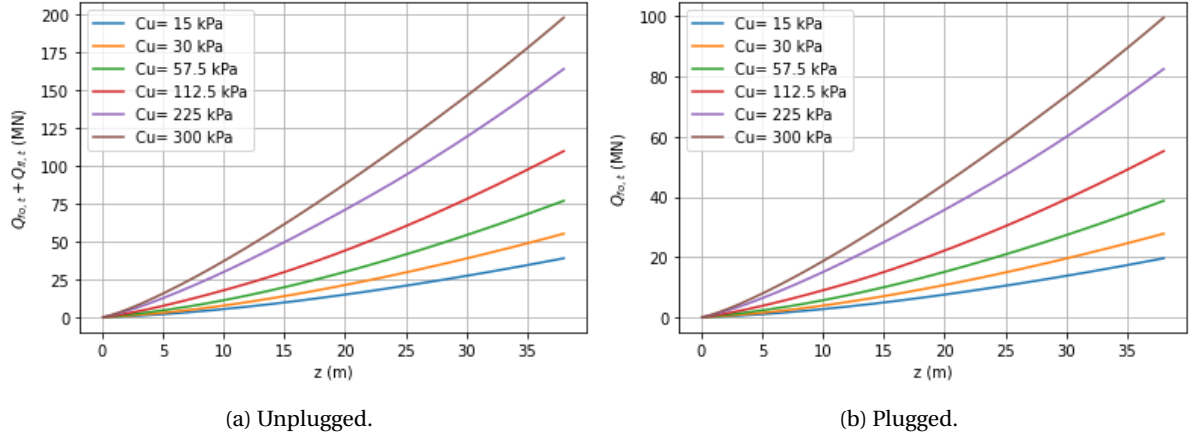


Figure 4.3: Shaft friction resistance in cohesive soils for a) an unplugged pile and b) a plugged pile.

4.4.2. Unit skin friction resistance in sands

In sands, or non-cohesive soils, the unit skin friction is determined by a single equation, Equation 4.8.

$$\begin{aligned}
f_{i,t}(z) &= f_{o,t}(z) \\
&= K_0 \sigma'_v(z) \tan(\delta) \\
&= \beta \sigma'_v(z) \leq f_{lim} \quad (4.8)
\end{aligned}$$

The unit skin friction resistance is caused by the horizontal effective stress, $K_0 \sigma'_v$, multiplied by the Coulomb friction, $\tan(\delta)$, or, in other terms, the horizontal effective stress multiplied by some value β . At large depths, the skin friction, f_z , no longer increases and the value is limited to f_{lim} [6]. The phenomenon behind this is not fully understood but might have something to do with the fact that under very high stresses the soil particles will readjust, lowering the stress. Values used in applying this equation come from several design standards and are summarized in Table 4.4.

Table 4.4: Input parameter for sand calculations [6–9].

| Sand type | f_{lim} (kPa) | $\beta^{[1]}$ |
|--------------|---------------------|---------------------|
| Very loose | 48.0 ^[2] | 0.21 ^[2] |
| Loose | 67.0 | 0.29 |
| Medium dense | 81.0 | 0.37 |
| Dense | 96.0 | 0.46 |
| Very dense | 115.0 | 0.56 |

[1] API-RP-2A-WSD & ISO 19902:2007-12-01 recommend to use these values for $f_{o,c}$, $f_{o,t}$ and f_i , DNV-OS-J101 recommends multiplying $f_{o,t}$ by 0.625. This is not done to stay close to the worst-case scenario that might be encountered offshore.

[2] Values come from DNV-OS-J101 [9] as both API & ISO recommend taking CPT profiles for such loose soils [6].

Using the skin friction from Equation 4.8, the total shaft resistance of a pile in sands can be found with Equation 4.9 for the unplugged scenario and Equation 4.10 for the plugged scenario. The depth at which the limit skin friction is reached, $z_{f,lim}$, and the shaft resistance thus increases linearly, lies between 20.5 and 23.0 meters for all soil types. The resulting total shaft resistances are plotted using python and shown in Figure 4.4.

$$\begin{aligned}
Q_{f_{o,t}} + Q_{f_{i,t}} &= \pi (D_o + D_i) \int_0^{L_{emb}} f_{i,o}(z) dz \\
&= \pi (D_o + D_i) \int_0^{z_{f,lim}} \sigma'_v(z) \beta dz + \pi (D_o + D_i) \int_{z_{f,lim}}^{L_{emb}} f_{lim} dz \\
&= \pi (D_o + D_i) \int_0^{z_{f,lim}} \gamma'_s z \beta dz + \pi (D_o + D_i) \int_{z_{f,lim}}^{L_{emb}} f_{lim} dz
\end{aligned} \tag{4.9}$$

$$\begin{aligned}
Q_{f_{o,t}} &= \pi D_o \int_0^{L_{emb}} f_o(z) dz \\
&= \pi D_o \int_0^{z_{f,lim}} \sigma'_v(z) \beta dz + \pi D_o \int_{z_{f,lim}}^{L_{emb}} f_{lim} dz \\
&= \pi D_o \int_0^{z_{f,lim}} \gamma'_s z \beta dz + \pi D_o \int_{z_{f,lim}}^{L_{emb}} f_{lim} dz
\end{aligned} \tag{4.10}$$

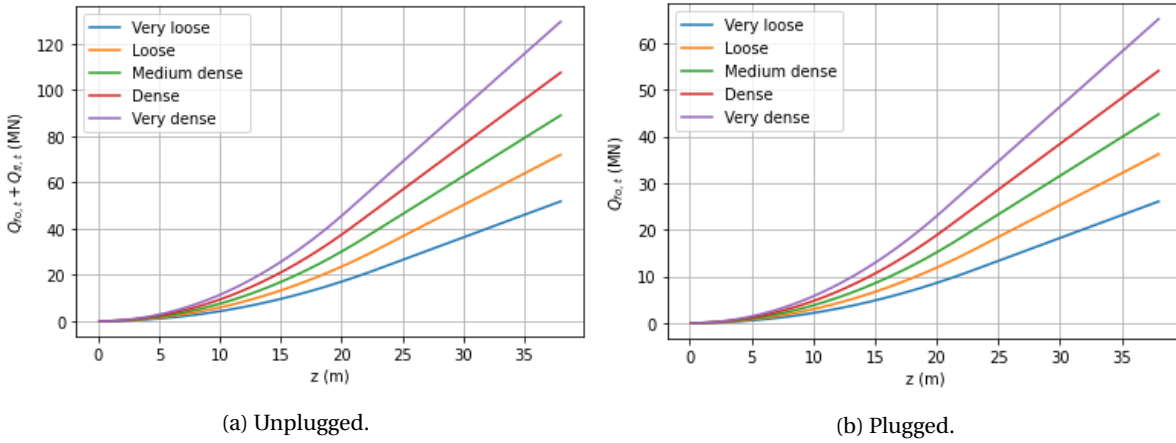


Figure 4.4: Shaft friction resistance in sands for a) an unplugged pile and b) a plugged pile.

4.4.3. Monopile and soil plug weight

The (submerged) weight of the monopile must also be added to obtain the total extraction force. The submerged part of the monopile experiences an upward buoyant force, reducing its weight. The monopile weight is calculated using Equation 4.11.

$$\begin{aligned}
W_{mp} &= W_{submerged} + W_{dry} \\
&= (\rho_{st} - \rho_w) g V_{emb} + \rho_{st} g V_{dry} \\
&= (\rho_{st} - \rho_w) g A (L_{emb} + L_{sub}) + \rho_{st} g A L_{dry}
\end{aligned} \tag{4.11}$$

Soon after a structures installation, its submerged part attracts living organisms that colonise the structure. These organisms, called marine growth, grow until a certain threshold thickness, which in the North Sea is 0.1 meters according to DNVGL-ST-0437 [86]. The density of marine growth is given as 1325 kg/m^3 , which leads to a unit submerged weight of marine growth of 2.94 kN/m^3 following Equation 4.12 [19]. The total

submerged weight of the marine growth is found by Equation 4.13 [19]. The weight of the monopile presented in chapter 3 and marine growth is shown in Table 4.5.

$$\gamma'_{mg} = (\rho_{mg} - \rho_w) g \quad (4.12)$$

$$\begin{aligned} W_{mg} &= V_{mg} \gamma'_{mg} \\ &= 0.25 \pi ((D_o + 2 t_{mg})^2 - D_o^2) L_{sub} \gamma'_{mg} \end{aligned} \quad (4.13)$$

Table 4.5: Partially submerged weight of the case study MP and marine growth.

| | Weight (MN) |
|---------------|-------------|
| Monopile | 8.63 |
| Marine growth | 0.20 |
| Total | 8.83 |

It must be noted that during the lift, more and more of the monopile emerges from the water and its weight increases. However, as the in air weight of the monopile is still much smaller than the soil resistance forces, this does not have to be included in the load case.

The submerged weight of an optional soil plug can be calculated using Equation 4.14 [19]. In this formula, the submerged unit weight of the soil is taken as 10 kN/m^3 . The result is listed in Table 4.6.

$$W_{sp} = V_{soil} \gamma'_s = 0.25 \pi D_i^2 L_{emb} \gamma'_s \quad (4.14)$$

Table 4.6: Submerged weight of soil plug.

| | Weight (MN) |
|-----------|-------------|
| Soil plug | 12.63 |

4.5. Load cases

With the preceding sections in mind, four different load cases for complete removal of monopiles can be distinguished. These load cases are made up of combinations of plugged and unplugged scenarios in either sands or cohesive soils and are listed in Table 4.7. The range given for the skin friction values represents the different soil compositions, i.e. density for sands and stiffness for cohesive soils. The effects of set-up over the duration of the pile its lifetime have not been included in this calculation.

Table 4.7: Load cases, all units are in MN.

| Load case | Skin friction | W_{sp} | $W_{mp} + W_{mg}$ | extraction force |
|--------------------|---------------|----------|-------------------|------------------|
| Cohesive plugged | 19.6 - 99.6 | 12.6 | 8.8 | 41.0 - 121.0 |
| Cohesive unplugged | 38.9 - 198.0 | - | 8.8 | 47.7 - 206.8 |
| Sand plugged | 28.2 - 70.2 | 12.6 | 8.8 | 49.6 - 91.6 |
| Sand unplugged | 56.0 - 139.5 | - | 8.8 | 64.8 - 148.3 |

From these ballpark figures for the ultimate static bearing capacity of a monopile in soils, a stress check can be performed on the case study monopile for the largest expected extraction force Equation 4.15. This simple check ensures that during the lifting operation, the stress on the monopile never exceeds the yield stress of the material. The yield stress for S355 steel commonly used in monopiles is 355 MPa. In lifting appliances, safety factors must be applied to the load case to allow for uncertainties. For tensile loads, the code for lifting appliances in a marine environment by Lloyd's [87] in section 4.2.17 prescribes a stress factor of 0.67 to be

applied to the failure stress, which is equal to the yield stress of the material for tension. This means that the allowable tensional stress in the monopile is 237.9 MPa.

$$\sigma = \frac{F}{A} = \frac{206.8e6}{1.6135} = 128.3 \text{ MPa} \quad (4.15)$$

The stress from this equation assumes that the extraction force that is exerted on the monopile is equally distributed over the entire cross-sectional area of the monopile equally. Whether this assumption is correct, depends on the state of the monopile at the end of its lifetime. Assuming that the LiftLok system that serves as the connection between the MP and the cranemaster allows for sufficient spreading of the pulling forces, the resulting stresses may be sufficiently low as not to rip the MP apart.

4.6. Soil behavior under cyclic loading

This section discusses the behavior of soils undergoing a deformation, stress and the theories involved in these processes. During the extraction process of a monopile, a lot of geotechnical phenomena are playing a role and not all of them can accurately be accounted for in this thesis. At the end of this thesis, an elaborate chapter discusses the limitations of the models used.

4.6.1. Non-linearity of soils

In marine environments, soils are saturated with water. This water fills the pores between grains and affects the behavior of soil when put under external loads. When a soil is externally loaded, it has a tendency to change its volume, but the interstitial fluid inhibits this tendency of volume change. Combined with other factors, e.g., grain structure (only in sands), hydraulic permeability and initial conditions (relative density, consolidation, over-consolidation) this leads soils to behave highly non-linear and visco-elastic-plastically [88]. The basic phenomena at hand for the non-linear response of soils to cyclic loads will be discussed in this chapter.

4.6.2. Cyclic loading

In offshore conditions, most loads exciting a monopile are cyclic. Much effort has been undertaken to understand the response of soils surrounding monopiles when they are excited by cyclic loads, but describing soil behavior under cyclic loading is more challenging than under monotonic loading. The effect of harmonic load patterns has been a subject of interest over the last decades, and numerous studies have been conducted concerning the response of the pile-soil interaction under harmonic loads. Cyclic loading affects the pore pressure and effective stresses in soils in such a way that soil strains, i.e., the displacement of soil under loading, can accumulate [25]. The interesting thing is that strain accumulation can occur at dynamic loads that are lower than the ultimate static capacity as calculated in section 4.5. Applying a cyclic force to a monopile under the right conditions can thus lead to a permanent displacement of the pile with respect to the soil [88]. The event where the pile starts to move as a result of dynamic loads that are lower than the ultimate static capacity will from now on be referred to as cyclic degradation of the capacity.

According to Poulos et al. [89], in clays, the origin of the degradation might come from changes in pore pressure in the soil adjacent to the pile or realignment of the clay particles adjacent to the pile.

One-way and two-way cyclic loading

The characteristics of the applied cyclic load have a large influence on the response of the soil. The most important characteristics are the amplitude of the forcing, the frequency, the number of cycles and the mode of the loading pattern [25]. Four general load cases of load patterns can be distinguished, Figure 4.5.

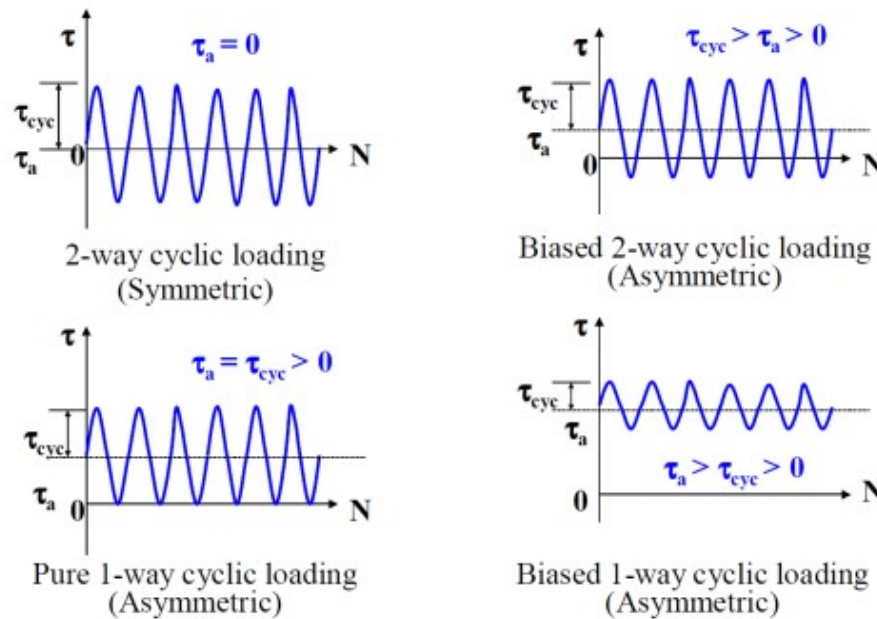


Figure 4.5: Types of cyclic loading [25].

These four generic load cases of shear stress under different modes of cyclic loading are defined as:

- **Two-way cyclic loading.** Under this type of loading, the sign of the load is changed over time. In practice this means that a pile will undergo both tensional and compressional stresses over the duration of one load cycle.
- **Biased two-way cyclic loading.** Two-way cyclic loading where the mean of the load is non-zero. There is still a reversal of the sign of the load during one load cycle.
- **One-way cyclic loading.** Under this type of cyclic loading, the sign stays constant over the duration of all load cycles of the load pattern. At the trough of the load pattern, the load is zero.
- **Biased one-way cyclic loading.** One-way cyclic loading at a certain mean. This thesis used biased one-way cyclic loading, since steel wires can only support tensional loads and no compressional loads.

During experiments, it has been observed that cyclic degradation is largest under two-way cyclic loading [25]. Because the steel wire cables of the main hoist of the JLS cannot exert any compressional forces, two-way cyclic loading cannot be applied and one-way cyclic loading without sign reversal must be applied.

4.6.3. Liquefaction

An important phenomenon that plays a role in cyclic degradation is liquefaction. This state of a soil arises when the contact area of soil particles is (partly) reduced, reducing shear forces inside the soil. Such an event might occur when drainage of a soil is slow (i.e. low permeability), or the rate at which shear force is applied is sufficiently high [25]. Under cyclic loading in such conditions, the soil particles will have a tendency to reorganize themselves and during that process, for small increments of time, they float in pore water and make no contact with neighbouring particles. Because water cannot carry a shear force, this results in a reduction of shear force on the pile interface. It is, however, improbable that liquefaction occurs at oscillation frequencies around 0.1 Hz, which is the vicinity of vessel motion frequencies due to wave excitation [90].

Other than liquefaction, phenomena that play a role in cyclic degradation are density, grain size distribution with respect to the direction of loading, strain amplitude, average stress and pre-loading history [91]. This all has an influence on the stiffness of the soil and subsequently, on the accumulation of displacement of the pile under cyclic loading. This is summarized in a figure by Tsuha et al. [26], who distinguishes three types of response of piles under axial cyclic loading, being a stable, meta-stable and unstable response, Figure 4.6.

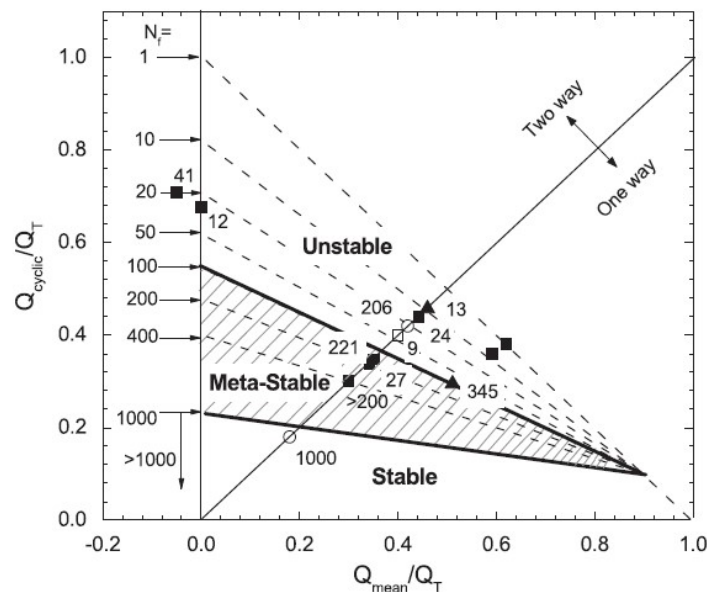


Figure 4.6: Cyclic shaft failure regime overview. Y-axis: amplitude of cyclic loading over ultimate static capacity. X-axis: mean of cyclic loading over ultimate static capacity, N_f is the number of cycles [26].

The behavior of a soil under loading in each of the three zones of the figure is as follows:

- In the stable zone, axial displacements accumulate very slowly and it takes hundreds of cycles before significant effects on capacity can be seen. In some cases, it has even been observed that shaft capacity increased to to cyclic loading in the stable regime [26].
- The unstable zone is defined by quick accumulation of displacements. The shaft capacity decreases enormously with reports by Tsuha et al. of the cyclic capacity being half that of the static capacity [26]. Failure is to be expected after 100 to 200 (two-way) load cycles.
- In the meta-stable zone failure develops after 100 to 1000 cycles.

4.6.4. t-z curves

Modelling the previously described complex behavior of soils, is tough and computationally expensive. In engineering applications, a simplification in the form of t-z curves is used. Such an approach is often relatively simple but still describes a soils response accurately enough for most applications. An example of a non-linear t-z curve is shown in Figure 4.7. The t-z elements are calibrated by this curve so that each spring responds with a certain shear force, τ , at a certain displacement, w . The shear force, or mobilized shaft resistance, increases with increasing spring deflection until it reaches a maximum value, the ultimate shaft capacity. This is the static ultimate shaft capacity, not the dynamic ultimate shaft capacity. In Figure 4.8, it can be seen that plastic displacement takes place at shear forces lower than the ultimate static capacity of the pile. By extending the model with more (uncoupled) springs, each with its own t-z curve to describe its behavior under axial loading, a more accurate response of the pile can be modelled. Such a type of model is known as a Beam on Non-linear Winkler foundation model.

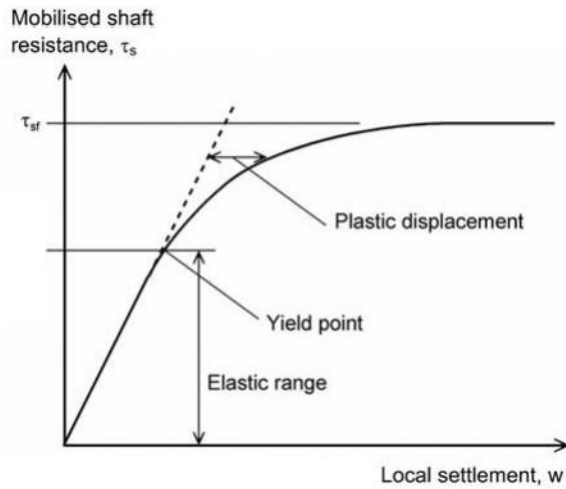


Figure 4.7: A non-linear t-z curve [25].

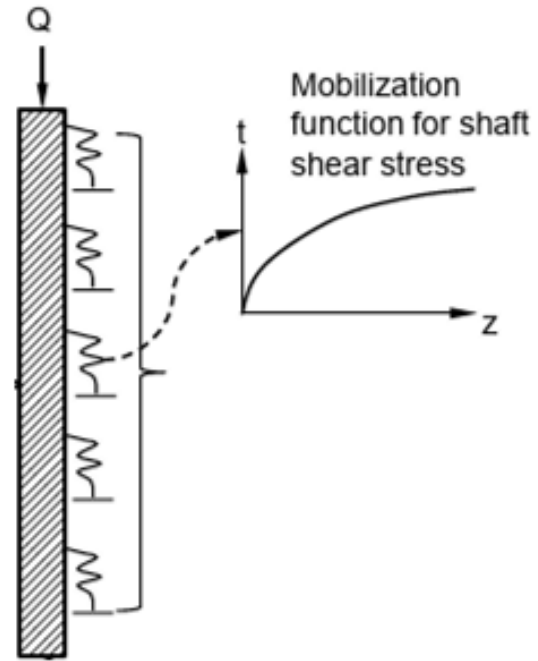
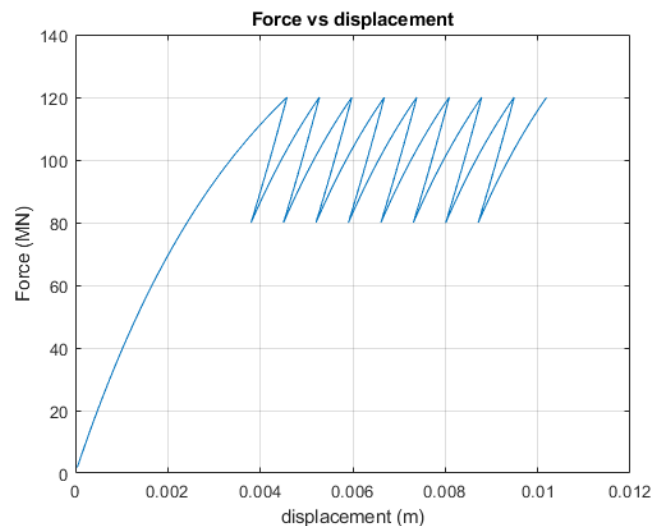


Figure 4.8: Visualization of t-z curve modelling often used in axial pile-soil models [27].

4.6.5. Hysteresis

The previously described t-z curve approach discussed the behavior of a pile under biased one-way cyclic axial loading. When a cyclic axial load is applied, the pile, and subsequently the t-z springs, behave differently. The mobilized shaft resistance in the t-z curve is increased and decreased during each cycle, resulting in loading and unloading of the springs. If the magnitude of the load stays within the elastic part of the curve, the load pattern over time will not show hysteresis, since there is no plastic displacement. If the plastic regime is reached, hysteresis occurs, and the pile starts to move because the plastic displacement is irreversible, Figure 4.9. The addition of repetitive plastic displacement is often referred to as strain accumulation in literature.

Figure 4.9: Hysteresis behavior under one-way cyclic loading. This figure is created with MATLAB with a simplified version of the model. Excitation force is $100\sin(0.1*2\pi t)$ (MN).

4.6.6. Progressive failure

Another important factor for modelling the response of piles to cyclic loading is that of progressive failure. Because the pile itself is made up of elastic material, it is able to elongate and shorten upon loading. The effect of this elongation, is that during the extraction process, along the embedded length of the pile, the mobilised shaft resistance differs. This is clearly illustrated in Figure 4.10, where it can be seen that the ultimate capacity of a rigid pile is higher than that of a flexible pile, as the soil surrounding the uppermost part of the pile has already reached the ultimate capacity and fails.

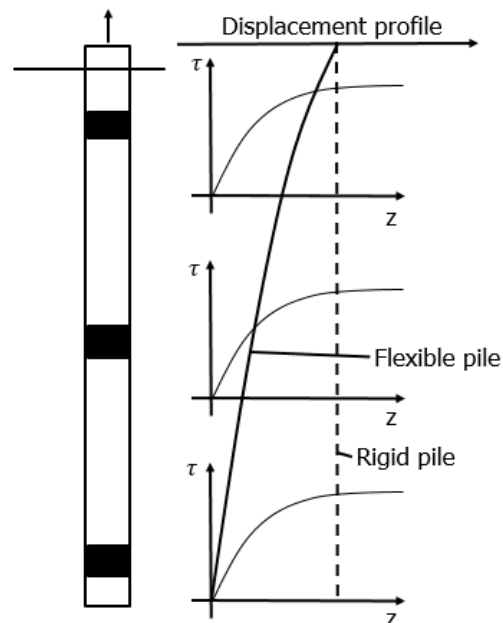


Figure 4.10: Progressive failure along a pile in clay.

4.7. Conclusion

This chapter introduced different soil types, classification of soils, and their most important geotechnical parameters that describe its behavior when loaded. The effects of set-up and principles behind plug formation have been discussed. Set-up is difficult to account for since research into monopile set-up is scarce and it is highly site specific. Plug formation is an uncertain phenomenon for the relatively large dimensions of piles considered in this research. Both the plugged and unplugged case are considered and the total extraction force is largest in the unplugged case. It can be concluded that the ultimate static capacity of piles in plugged situations is relatively low, and even the largest values in this case are well below the JLS capacity of 20.000 tons. The ultimate static capacity of piles is largest in stiff clays, with the total extraction force for the stiffest clay type considered being over 200 MN. Adding to that potential set-up and other time-dependent effects that may increase the bearing capacity of piles in soil, it can be concluded that the 20.000 ton lifting capacity of the JLS is unlikely to be enough to complete remove every first generation monopile in the North Sea.

The response of soils under cyclic loading is different than under static loading, as its non-linear and visco-elastic-plastic behavior allows for accumulation of displacements. The characteristics of the cyclic loading, such as amplitude, frequency, number of cycles, and mode of the loading pattern have a large influence on soil response. Liquefaction is a phenomenon that is able to greatly reduce the ultimate static capacity of piles, but it occurs at frequencies that are generally higher than those seen in vessel motion. The behavior of axial pile displacement in soils is often modelled by t - z curves, where the relationship between the mobilised shaft resistance, τ , and the pile settlement, w , describes the stiffness of the spring elements. These elements also allow for hysteresis to occur, which is a path-dependent phenomenon where plastic displacements accumulate. Progressive pile failure along the embedded depth of the pile also plays an important role in cyclic degradation of the soil, as the topmost part of the pile is able to elongate and gradually fail the soil along the embedded part of the pile.

5

Vessel Model

To prove the hypothesis of this thesis, namely that vessel motion can reduce soil resistance on monopiles during the removal process, it is necessary to understand what these vessel motions look like, to have a feeling for what the quantities of vessel displacement, velocity and acceleration are and how a representative force on the monopile can be constructed as an extraction force. This chapter discusses how vessel motion is modelled and how this is eventually translated to a force that can be used in the FEM model.

5.1. Introduction

The vessel model used in this thesis is a time domain analysis of a mass-spring-damper system that makes use of the vessel motion equation around the center of gravity, which is commonly used in rigid body dynamics, depicted in Equation 5.1.

$$(m_i + a_i)\ddot{x}_i + b_i\dot{x}_i + k_i x_i = F_a \sin(\omega_i t) \quad (5.1)$$

Where: $i = 1:6$, one of 6 degrees of freedom

x_i = Displacement of one of the six degrees of freedom (m)

m_i = mass or inertia for that degree of freedom (kg)

a_i = added mass for that degree of freedom (kg)

b_i = hydrodynamic damping for that degree of freedom (kg/s v kgm/s)

k_i = Hydrostatic stiffness in that degree of freedom (kg/s^2 v kgm/s^2)

F_a = Amplitude of forcing term or moment (N)

ω_i = Frequency of forcing term (rad/s)

For a freely floating vessel, this equation can describe vessel motion in each of its six degrees of freedom, therefore, to model all 6 degrees of freedom, 6 equations of motion are necessary. The degrees of freedom and their symbols are shown in Figure 5.1. The forcing term on the right hand side represents the Froude-Krylov force of the waves [28].

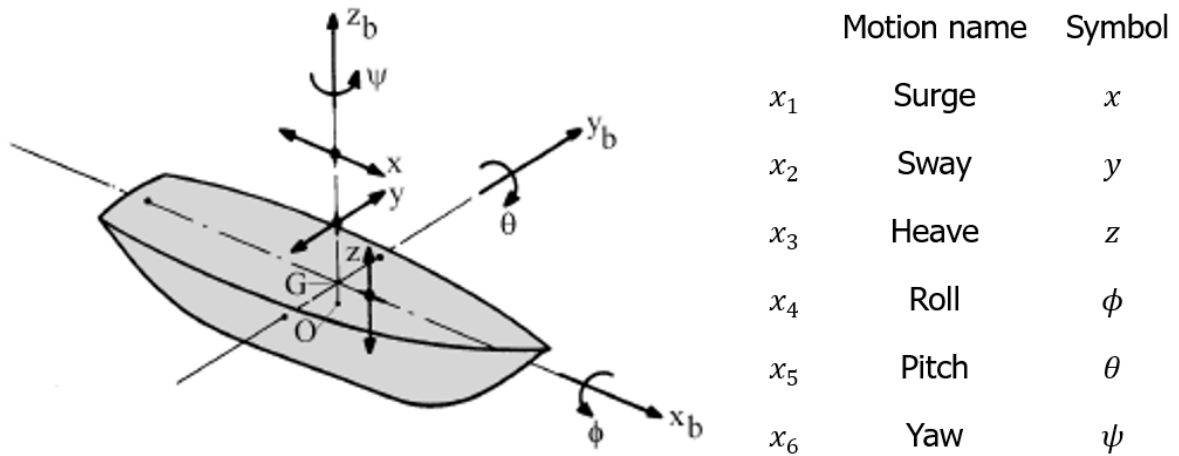


Figure 5.1: Vessel motions overview and definition [28].

5.1.1. Pioneering Spirit

This study makes use of Allseas' Pioneering Spirit as its case study vessel. Allseas has provided its specifications for this research and they are listed in Table 5.1. In this table, the beam tip coordinate represents the location of the end of the beam when the beams are tilted to a 110 degree angle w.r.t. the horizontal. The global coordinate system is shown in Figure 5.2 which also shows the main points of interest of the model. Note that this table does not yet list the added mass and damping of the vessel, as these are frequency dependent and will be determined later.

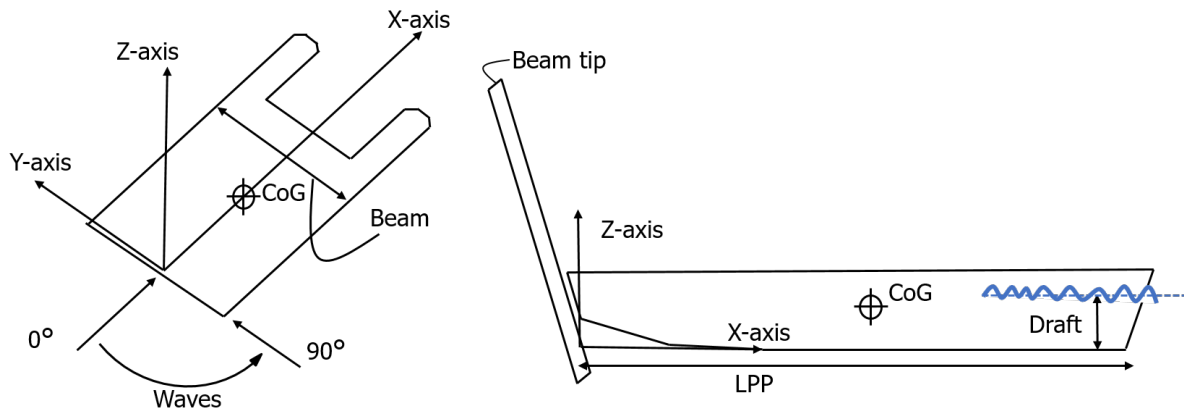


Figure 5.2: Global coordinate system of the Pioneering Spirit and definition of vessel dimensions.

Table 5.1: Pioneering Spirit specifications.

| Parameter | Symbol | value | unit |
|-------------------------------|--------------|-------|---------|
| Length between perpendiculars | $L_{PPL,PS}$ | 370 | m |
| Beam PS | B_{PS} | 123.5 | m |
| Draft PS | T_{PS} | 17.0 | m |
| Mass PS | m_{33} | | kg |
| Mass main hoist block | m_h | --- | kg |
| Points of interest | | | |
| Centre of gravity x | CoG_x | | m |
| Centre of gravity y | CoG_y | | m |
| Centre of gravity z | CoG_z | | m |
| Beam tip x | $B_{t,x}$ | | m |
| Beam tip y | $B_{t,y}$ | | m |
| Beam tip z | $B_{t,z}$ | | m |
| Dynamic properties | | | |
| Roll Inertia | m_{44} | | kgm^2 |
| Pitch Inertia | m_{55} | | kgm^2 |
| Yaw Inertia | m_{66} | | kgm^2 |
| Hydrostatic heave stiffness | c_{33} | | N/m |
| Hydrostatic pitch stiffness | c_{55} | | N/m |

The mass of the main hoist block is made up of the sum of four separate parts, being the lower block, lower cardan, swivel and trunnion. Together, the total mass comes to 189.6 tons, rounding up a value of 200 tons is taken for just one main hoist system. Every beam has 3 main hoist systems, coming to a total main hoist block mass of 1200 tons to account for both beams.

5.2. Model set-up

The vessel model is simplified to a 3 DOF system in order to keep the computations relatively simple while still capturing the main characteristics of vessel motion. A schematic overview of the model is shown in Figure 5.3.

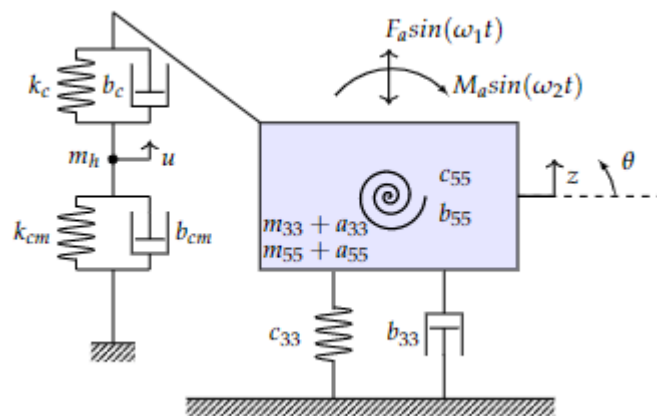


Figure 5.3: Schematic overview of vessel model.

The three degrees of freedom are heave and pitch of the vessel as well as vertical motion of the main hoist block, denoted by u . The model is made up of 2 sets of spring-dampers representing resistance to heave and pitch as well as 1 spring-damper representing the steel wire cables of the main hoist block of the JLS. Below these springs, another spring-damper represents a cranemaster. The two beams, steel wire cables and derrick hoist system of the JLS are all represented by the single spring-damper system k_c and b_c , quantification of these parameters follows later in the chapter. Likewise, six cranemasters are modelled by 1 representative stiffness and damping, k_{cm} and b_{cm} . These six cranemasters, each with a lifting capacity of 5000 tons, are each connected to one main hoist block, of which every beam has three blocks. See Figure 5.4 for clarification.



Figure 5.4: The Jacket Lift System on the Pioneering Spirit with its two beams and six main hoist systems with a capacity of 5000 tons each[18]. The total capacity of the JLS is still 20.000 tons, since not all six main hoist systems can operate at maximum capacity at the same time.

5.2.1. Methodology

The general procedure of creating the vessel model is as follows, firstly the vessel parameters are determined while the vessel is freely floating, meaning that the two spring-damper systems on the left side of Figure 5.3 are turned 'off'. The forcing terms are then calibrated so that the tip of the JLS beams makes the same motions as observed by Allseas' motion reports. Then the spring-dampers are turned 'on' again, which will have an influence on the motion of the vessel since the crane-master is fixed to the earth. The displacement of the crane head is then translated to a force using the stiffness and damping of the crane-master. The vessel model is modelled in MATLAB and the ode45 function is used to solve the equations of motion, since the problem is not extremely stiff.

5.2.2. Equations of motion

The equations of motion are determined making use of the Lagrange method. This method determines the energies present in the system and uses the Lagrangian to construct equations of motion. The Lagrangian is defined as $L = T - V$, where L represents the Lagrangian, T represents the kinetic energy and V the potential energy. Together with the dissipation of the system, D , the equations of motion of the system can be found by solving Equation 5.2 [92].

$$\frac{d}{dt} \left(\frac{\delta L}{\delta \dot{x}_i} \right) - \frac{\delta L}{\delta x_i} + \frac{\delta D}{\delta \dot{x}_i} = Q_i \quad (5.2)$$

Of the simple system shown in Figure 5.3 the following kinetic and potential energies are derived as well as the dissipation using Equation 5.3 to Equation 5.5.

$$T = \frac{1}{2}(m_{33} + a_{33})\dot{z}^2 + \frac{1}{2}(m_{55} + a_{55})\dot{\theta}^2 \quad (5.3)$$

$$V = \frac{1}{2}c_{33}z^2 + \frac{1}{2}c_{55}\theta^2 + \frac{1}{2}k_c(z - \theta l - u)^2 + \frac{1}{2}k_{cm}u^2 \quad (5.4)$$

$$D = \frac{1}{2}b_{33}\dot{z}^2 + \frac{1}{2}b_{55}\dot{\theta}^2 + \frac{1}{2}b_c(\dot{z}^2 - \dot{\theta}l - \dot{u}) + \frac{1}{2}b_{cm}\dot{u}^2 \quad (5.5)$$

Note that use has been made of the small angle approximation, which is a valid assumption as the stiffness of the Pioneering Spirit is substantial and pitch angles are expected to remain significantly small.

Equation 5.6 shows the equations of motion that are obtained in matrix form.

$$\begin{bmatrix} m_{33} + a_{33} & 0 & 0 \\ 0 & m_{55} + a_{55} & 0 \\ 0 & 0 & 0 \end{bmatrix} \begin{bmatrix} \ddot{z} \\ \ddot{\theta} \\ \ddot{u} \end{bmatrix} = \begin{bmatrix} F_a \sin(\omega_1 t) \\ M_a \sin(\omega_2 t) \\ 0 \end{bmatrix} - \begin{bmatrix} b_{33} + b_c & -b_c l & -b_c \\ -b_c l & b_{55} + b_c l^2 & b_c l \\ -b_c & b_c l & b_c + b_{cm} \end{bmatrix} \begin{bmatrix} \dot{z} \\ \dot{\theta} \\ \dot{u} \end{bmatrix} - \begin{bmatrix} c_{33} + k_c & -k_c l & -k_c \\ -k_c l & c_{55} + k_c l^2 & k_c l \\ -k_c & k_c l & k_c + k_{cm} \end{bmatrix} \begin{bmatrix} z \\ \theta \\ u \end{bmatrix} \tag{5.6}$$

5.2.3. Added mass and damping

Every vessel operating in a fluid, has an added mass that accounts for the fact that the body is not moving through air but water, and needs to accelerate some amount of the surrounding water as well. In vessel modelling this is accounted for by adding extra inertia to the system in the form of added mass. This term, which has the same unit as mass itself, is frequency dependent, which means that for every frequency at which the vessel moves, the added mass is different [28]. On top of that, added mass is also dependent on direction, meaning that the added mass matrix for a ship is a 6-by-6 matrix for every frequency of motion.

Another factor that has to be taken into account is hydrodynamic damping, which finds its origin in the fact that water is more viscous than air, causing energy to dissipate more quickly through the surrounding water [28]. Hydrodynamic damping is frequency and directional dependent as well, meaning that at every frequency, it is represented by a 6-by-6 matrix.

The added mass and hydrodynamic damping tables are known from analyses performed by Allseas using the hydrodynamic simulation software, Ansys AQWA. Calibration of the model is necessary to make sure that the correct added mass and damping values are selected. Since the added mass and damping are dependent on frequency, it is of importance to know the frequency at which the vessel will move. The Pioneering Spirit is a heavy vessel, with a large stiffness, and the free-floating vessel model is linear, so it can be expected that the frequency of the vessel motion in this model is equal to the excitation frequency of the forcing terms in Equation 5.6. The forcing frequency is based on data provided by Allseas on motions of the PS in a motion report. A motion report generates the 3-hours maxima of displacement, velocity, and acceleration for a specific point on the PS. An example of a motion report is given in Figure 5.5 and from the report, the forcing frequency of any DOF can be calculated using Equation 5.7. In this equation v and x are taken as the maximum values occurring for that DOF in a 3-hour time window and the equation assumes that the motion of the PS in this time-window is a perfect sinusoid.

$$\omega = \frac{v}{x} \tag{5.7}$$

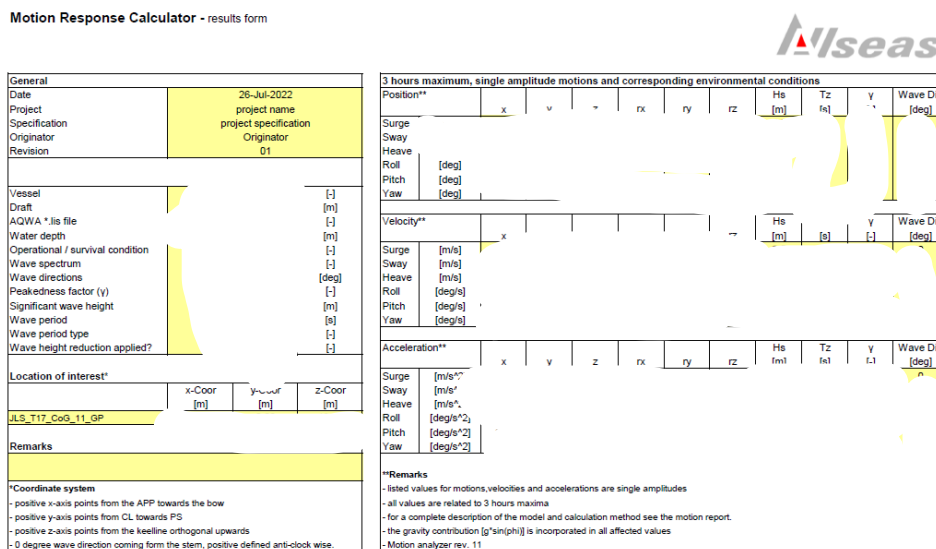


Figure 5.5: Example of a motion report for the CoG for a sea state of $H_s =$ m, $T_z =$ s.

After calculation of the forcing frequencies, and consequently the heave and pitch response frequencies of the vessel, the added mass and damping can be determined at those frequencies. This data comes from the aforementioned Ansys AQWA tables, the values can be found in Table 5.2, the data can be found in Appendix D. The data in this table is applicable for a draft of 17 meters and a water depth of 35 meters, corresponding to the Pioneering Spirit operating at maximum capacity with the JLS at a wind farm in relatively deep waters.

Table 5.2: Pioneering Spirit parameters used as inputs in the vessel model, including the frequency dependent parameters added mass, hydrodynamic damping and damping ratio.

| | Symbol | Heave | Pitch | Unit |
|-----------------------|------------|-------|-------|-----------------------|
| Hydrostatic stiffness | c_{ii} | | | $kg/s^2 \vee kgm/s^2$ |
| Forcing frequency | ω_f | | | rad/s |
| Added mass | a_{ii} | | | kg |
| Hydrodynamic damping | b_{ii} | | | $kg/s \vee kgm/s$ |

5.2.4. Natural frequency validation

A validation of the model can now be performed by setting the forcing terms, F_a and M_a , as well as the crane-master and cable terms k_c, k_{cm}, b_c, b_{cm} , equal to 0, so that only the spring and damping terms representing resistance to vessel motion in heave and pitch, remain active. Giving the model an initial displacement then results in an oscillation that damps out decreasingly with a frequency equal to the natural frequency of that degree of freedom. The undamped natural frequency and corresponding damping ratios are known from the Ansys AQWA data and listed in Figure 5.6. From the natural frequency and the corresponding critical damping ratio (see Appendix D), the added mass and damping can be calculated using Equation 5.8 and Equation 5.9. Using these as inputs into the model and giving an initial displacement results in the oscillation dying out at the natural frequency. The frequency of the model response will be slightly lower than the natural frequency listed in Table 5.3 because AQWA determines the undamped natural frequency and the model responds according to the damped natural frequency. The damped natural frequency, ω_d , can be calculated using Equation 5.10.

$$\omega_i = \sqrt{\frac{c_{ii}}{m_{ii} + a_{ii}}} \quad (5.8)$$

$$\zeta_i = \frac{b_{ii}}{b_{crit}} = \frac{b_{ii}}{2\sqrt{c_{ii}(m_{ii} + a_{ii})}} \quad (5.9)$$

$$\omega_d = \omega_n \sqrt{1 - \zeta^2} \quad (5.10)$$

The results of the validation are shown in Figure 5.6 and the natural period of the model can be read from the graph. The frequency dependent input parameters used in this validation are shown in Table 5.3.

Table 5.3: Pioneering Spirit parameters used as inputs in the vessel model during the natural frequency validation. Frequency dependent parameters added mass, hydrodynamic damping and damping ratios used in the natural frequency validation of the model.

| | Symbol | Heave | Pitch | Unit |
|-----------------------|------------|-------|-------|-----------------------|
| Hydrostatic stiffness | c_{ii} | | | $kg/s^2 \vee kgm/s^2$ |
| Natural frequency | ω_n | | | rad/s |
| Damping coefficient | ζ | | | - |
| Added mass | a_{ii} | | | kg |
| Hydrodynamic damping | b_{ii} | | | $kg/s \vee kgm/s$ |

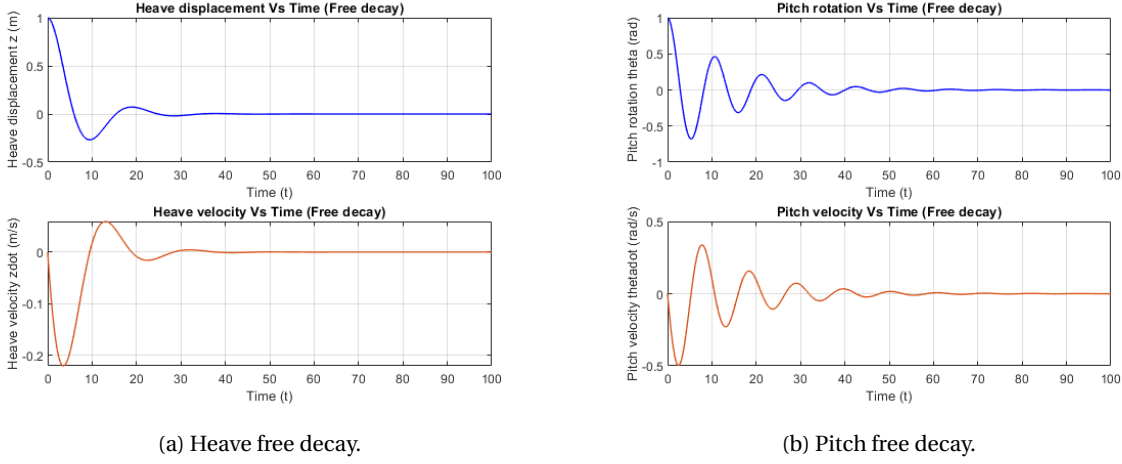


Figure 5.6: Validation of vessel model by natural frequency check in Heave and Pitch.

The undamped natural frequency, theoretical damped natural frequency that is the result of Equation 5.10 and the model damped natural frequency are shown in Table 5.4, The values of damped natural frequency are in agreement for both DOFs, showing a 0.12% derogation for heave and 0.20% for pitch.

Table 5.4: Theoretical and model damped and undamped radial natural frequencies.

| | Heave | Pitch |
|--|-------|-------|
| Undamped natural frequency (rad/s) | | |
| Theoretical damped natural frequency (rad/s) | | |
| Model damped natural frequency (rad/s) | | |

5.2.5. Calibration of forcing terms

Now that all the vessel parameters are known, the model can be calibrated by adjusting the amplitudes of the forcing terms, M_a and F_a . The forcing terms are scaled so that the motion of the CoG is exactly the same as Allseas' data prescribes. This is done at the hand of the previously introduced motion report, Figure 5.5.

The motion report is created for a water depth of 35 meters and a JONSWAP spectrum with a peak shape factor of 0.0. The response to beam waves is reduced as the resulting sway and roll response blow up due to the computational method. For more information about the JONSWAP spectrum, reference is made to Appendix E. Other sea states with peak shape factors of 1.0 (Pierson-Moskowitz spectrum, swell waves) and 3.3 (wind waves) are also considered.

The three hour maxima need to be converted to significant (single) amplitudes to be useful, as the three hour maxima only appear once every three hours, which is not very useful for this application from an operability point of view. This is done using Equation 5.11 which makes use of the common assumption that approximately one thousand waves pass in a 3-hour during period. For the application of this thesis, relatively large vessel motions are required to induce a harmonic force on the monopile. That is why a rough sea state, corresponding to the operational limit of the PS, is selected.

$$a_{max} = a_s \sqrt{\frac{1}{2} \ln(N)} = 1.86 a_s \quad (5.11)$$

Where: a_{max} = the maximum single amplitude
 a_s = the significant single amplitude, here, significant means the mean of the highest one third of motions
 N = the number of waves in a three hour time window

$$CoG_{motion} = x_h \sin(\omega t) = x_h \sin\left(\frac{v_h}{x_h} t\right) \quad (5.12)$$

Using Equation 5.12, a representative heave and pitch motion of the centre of gravity can be constructed in the form of a sine wave. This is shown in Figure 5.7.

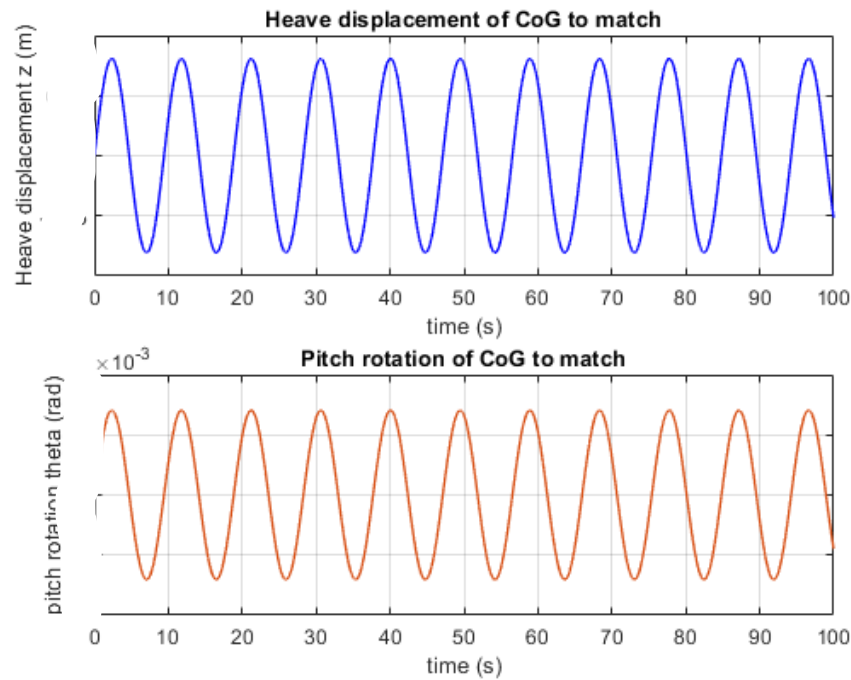


Figure 5.7: Heave and pitch motion simplification in CoG as obtained from a motion report.

Now the motion of the model needs to match the motion of the beam tip, which can be achieved by calibrating the forcing terms F_a and M_a , which is achieved by setting the forcing terms equal to those of Equation 5.13.

$$\begin{aligned} F &= F_a \sin(\omega t) = \sin(\quad t) \\ M &= M_a \sin(\omega t) = \sin(\quad t) \end{aligned} \quad (5.13)$$

5.3. Steel cable-wire modelling

Now that the vessel model is calibrated and the motions at the CoG are the same as Allseas' motion reports suggest, the remaining model parameters can be determined, being the spring-damper parameters for the steel wire crane cables and the cranemaster. The following section determines the model inputs of the spring-damper system that represents the steel-wire cables of the JLS.

5.3.1. Steel wire stiffness

According to Valk [93], steel wire ropes used for offshore lifting operations can be represented in a model as a simplified spring-damper connection. The force is assumed to be linear with elongation of the wire, leading to a constant spring coefficient, k_c [93].

$$k_c = \frac{EA_{eff}}{L_w} \quad (5.14)$$

Where: E = Young's' Modulus of steel wire (Pa)
 A_{eff} = Effective area of wire (m^2)
 L_w = Initial wire length (m)

Here A_{eff} represents the effective area of the wire rope, which is about two-thirds of the total area due to cavities in between the independent steel elements [94]. Notice that in this equation, the stiffness of the wire is dependent on its length and that during the lifting operation the length is decreased, increasing the stiffness. It is assumed that this change in length, and consequently stiffness, is marginal in the first seconds of lifting, hence it is not taken into account [93]. A constant length of 75 meters is assumed to calculate the wires stiffness.

The properties of the wire rope used in the JLS are shown in Table 5.5.

Table 5.5: JLS main hoist steel wire properties.

| Category | Value | Unit |
|--------------------------------|------------------------------|----------------------|
| Wire type | 8xK31WS + IWRCX (7x19 Seale) | - |
| Tensile grade | 1960 | (N/mm ²) |
| Axial stiffness | 310 | MN |
| Nominal length | 4.000 | m |
| Under Tension diameter 10% MBL | 77,80 | mm |
| Unit weight in air | 27,7 | kg/m |

The wire of the JLS main hoist is reeved multiple times to reduce the load on the winches that drive the steel wire. Per main hoist block this is done 40 times. The wires all run parallel to each other, resulting in a stiffness that is 40 times as large as that of a single wire. On top of that, three hoist blocks are used per beam, and 2 beams are utilised, resulting in a wire stiffness that is 240 times more stiff than a single wire. The main hoist is not the only component of the crane that can stretch and absorb some of the displacements of the vessel. The beams themselves can bend a little bit and the derrick hoist wires, the wires that hold the beams in position when lifted, also allow for some stretch. In discussion with experts at Allseas who are familiar with the system, it has been decided to model this by multiplying the main hoist wire stiffness by 0.5, so that the contribution of all other components is taken into account. The resulting spring stiffness used in the model is shown in Table 5.6 in the next section.

5.3.2. Steel Wire Damping

There are two physical phenomena that contribute to damping in steel wires, material and frictional damping, the latter being caused by relative motion between independent wires [93]. For spiral wires, frictional type of damping is dominant and its damping coefficient can be described by Equation 5.15 [93].

$$b = \zeta b_{crit} = \frac{1}{\sqrt{1 + \left(\frac{2\pi}{\delta}\right)^2}} 2\sqrt{k m_{wire}} \quad (5.15)$$

Where: ζ = dimensionless damping coefficient (-)
 b_{crit} = Critical damping (Ns/m)
 δ = logarithmic decrement (-)
 k_c = Stiffness of wire (N/m)
 m_{wire} = mass of the wire (kg)

The logarithmic decrement, δ , is determined by Equation 5.16 and follows from free decay tests with steel wires. It is determined by the natural logarithm of the ratio of two consecutive maximum amplitudes of the amplitude time history during the free decay test [95, 96].

$$\delta = \frac{1}{n} \ln\left(\frac{x_i}{x_{i+1}}\right) \quad (5.16)$$

Where: n = number of oscillations
 x_{i+1} = the upper peak following peak x_i
 x_i = the peak succeeding x_{i+1} in the time domain

Research by van der Veldt et al. [97] discovered that determining a single value for damping of steel wires is tough, as the value depends on a great many factors such as but not limited to the loading history, amplitude and frequency of the load and displacement, the type of lubricant (Nyrosten T55 in case of JLS) and the age of the wire. However, [93] found that a reasonable bound for the δ parameter is between 0.02 and 0.20 for multi-strand wire ropes and consequently, δ will be taken as 0.10. This then results in a damping ratio ζ of 0.016, or 1.6% [93].

Now that all the unknowns of Equation 5.15 are known, the damping of the main hoist cables can be calculated. A summary of all the parameter values as well as the damping is shown in Table 5.6.

Table 5.6: Parameters for steel wire stiffness and damping calculations and the damping entered in the model as b_c .

| parameter | value | unit |
|-----------|-------|-------|
| k_c | 496 | MN/m |
| δ | 0.10 | - |
| b_c | 0.501 | MNs/m |

5.4. Cranemaster

This section calculates the stiffness and damping variables that are used in the model to represent the behavior of the cranemaster. The selected cranemaster for this research is a passive heave compensator with a hydraulic nitrogen - oil cylinder and an accumulator. The use of Cranemasters is necessary to reduce the dynamic forces on the crane and to avoid slack in the wires as well as snap loads. A 1000 ton cranemaster is selected for this operation which has a stroke of 4 meters, and a lifting capacity of 1000 tons. This cranemaster is scaled-up to a 5000 ton cranemaster unit by multiplying the static force in air capacity by 5, while keeping the stroke length constant. This effectively scales the stiffness of the cranemaster with a factor of 5 as well. The same is done for the damping. This 5000 ton unit is used six times, one for every main hoist block of each of the JLS beams. The total capacity of the six cranemaster together comes to 30.000 tons, allowing for safety margins and snap loads. Following the tensioning procedure, it is assumed that the model starts with a cranemaster extension of two meters, and an initial velocity of zero. To make sure that the model starts at rest, and no initial vibrations are present, the static force in air is normalised with the value at 2.0 meter stroke length.

The damping force is taken as absolute so that multiplication with the velocity of the crane head, \dot{u} , results in the proper sign of the force. Both the stiffness, and the damping dataset are fitted in Matlab using the polyfit function, resulting in a total, non-linear, cranemaster force shown in Equation 5.17. The coefficients A to F are determined by Matlab. The modified stiffness and damping forces that are the result of the aforementioned adjustments are visualised in Figure 5.8.

$$F_{cm} = Au^2 + B u + C + D|\dot{u}|\dot{u} + E\dot{u} + F \quad (5.17)$$

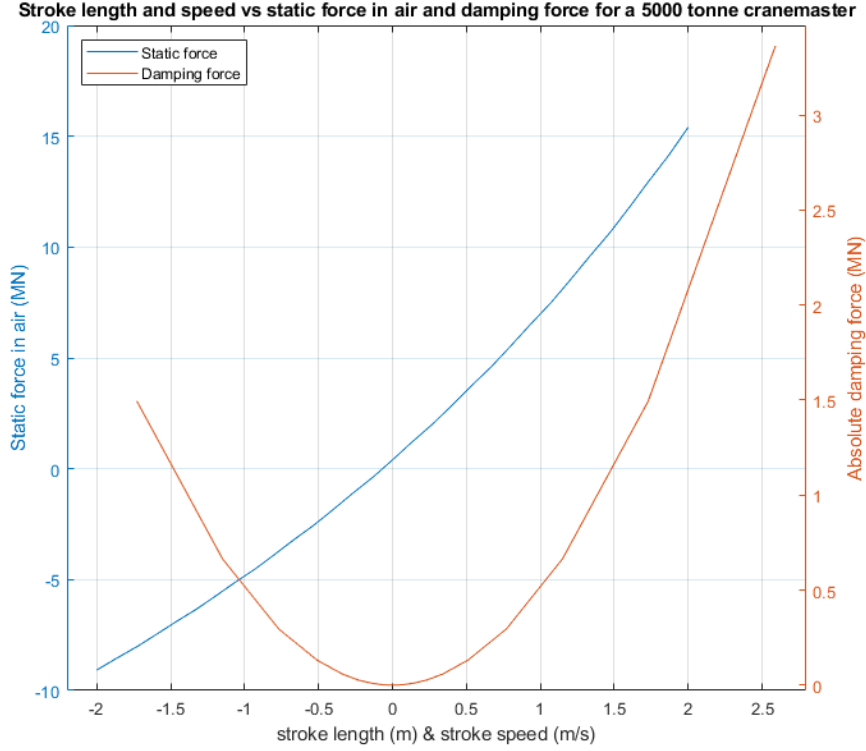


Figure 5.8: Damping and stiffness cranemaster versus stroke length and speed visualized.

Application of such a non-linear stiffness and damping in the equations of motion means that a matrix form of the equations is no longer an option. Instead, the three equations of motion are written separately like in Equation 5.18.

$$\begin{aligned}
 \ddot{z} &= \frac{F_a \sin(\omega_1 t) - (c_{33} + k_c)z + k_c l \theta + k_c u - (b_{33} + b_c) \dot{z} + b_c l \dot{\theta} + b_c \dot{u}}{m_{33} + a_{33}} \\
 \ddot{\theta} &= \frac{M_a \sin(\omega_2 t) - (c_{55} + k_c l^2)\theta + k_c l z - k_c l u - (b_{55} + b_c l^2)\dot{\theta} + b_c l \dot{z} - b_c l \dot{u}}{m_{55} + a_{55}} \\
 \ddot{u} &= \frac{k_c z - k_c l \theta - k_c u + b_c (\dot{z} - l \dot{\theta} - \dot{u}) - F_{cm}}{m_h}
 \end{aligned} \tag{5.18}$$

Where: F_{cm} = Cranemaster force, see Equation 5.17

$$\vec{x} = [z; \dot{z}; \theta; \dot{\theta}; u; \dot{u}]$$

5.5. Conclusion

This chapter has shown the set-up of a model describing motion of the Pioneering Spirit while it is connected to a monopile that is fixed in the ground. The model consists of simple, linear spring-damper combinations to represent the vessels response to wave excitation in heave and pitch. The steel wire cables are represented by linear spring-damper systems and a cranemaster, which is introduced to protect the crane from large snap loads, by a non-linear spring damper system. The equations of motion are determined following Lagrange's Theorem, and implemented in MATLAB which solves the differential equations using the ode45 solver.

Calibration of the vessel parameters added mass and damping is achieved by looking at the expected motion frequencies of the vessel and retrieving relevant parameters from Ansys AQWA data available at Allseas. The

forcing terms are then chosen so that motion of the beam tip is equal to calculated motions from motion reports from Allseas. The model is validated by comparing its natural frequency in heave and pitch to those found by Ansys AQWA, and they match well. Finally, the equations of motion are rewritten so that the non-linearity in the crane-master force is represented accurately.

6

Pile-soil interface modelling

The pile-soil interface is modelled in the Open System for Earthquake Engineering Simulation software, or OpenSees. It is an open source software Finite Element (FE) package. Being a seismic analysis tool, it excels at describing the difficult non-linear effects and visco-elastic-plastic behavior of soils [88]. It offers a wide variety of solvers and integrators to solve complicated pile-soil systems in both static and dynamic analyses [88]. This chapter discusses the model that was built in this thesis to answer the research questions.

6.1. Modelling pile-soil interaction

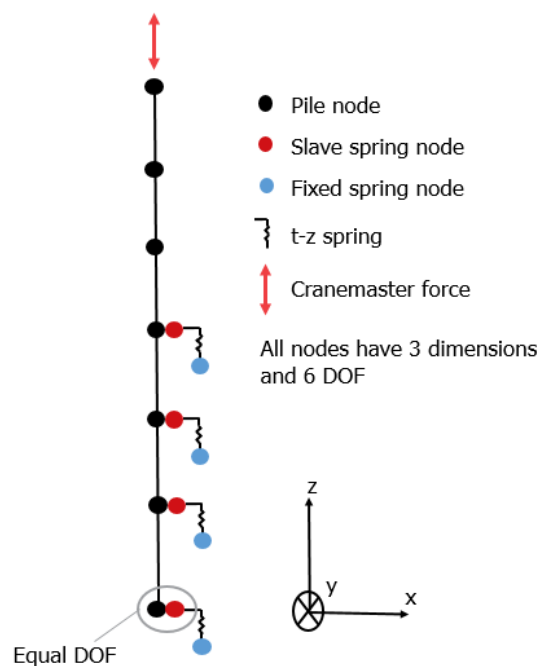


Figure 6.1: Schematic overview of the FEM model that is modelled in OpenSees.

The model used for this research is built on the basis of a Beam on Non-linear Winkler foundations and is a modified version of an example model available on the OpenSees website [98]. To accurately describe the behavior of the soil surrounding the pile, the pile is cut into sections and each section is connected to a non-linear t-z spring that represents the soils resistance to axial loading [98]. A schematic overview of the model is presented in Figure 6.1. The pile elements are created between the pile nodes, while the t-z springs are fit between the slave spring nodes and the fixed spring nodes [98]. At $t = 0$, these spring nodes are in the exact

same location and after loading is applied, the slave spring nodes move upward with their corresponding pile node using an equal DOF command [98]. The TzSimple1 element in OpenSees prescribes the resistance to vertical displacement that the slave node experiences. The TzSimple1 element is added to a ZeroLength element, describing its behavior; this element is located between the slave and fixed spring nodes [99].

6.1.1. T-z springs

Every pile node has a corresponding slave and fixed spring node. In between the latter two, a ZeroLength element is defined with the behavior of a t-z spring. A t-z spring in OpenSees needs two inputs at every depth, consisting of τ_{ult} , representing the ultimate capacity of the soil at which it fails, and z_{50} , representing the displacement at which 50% of the ultimate capacity of the soil is reached. In OpenSees, the input parameter τ_{ult} must be given in units of force (N), so the shear force τ_{ult} is multiplied by the area of the pile and the height soil column that the element at that depth describes. This force input parameter will from now on be denoted as t and t_{ult} . The ultimate capacity is calculated using the parameters and equations discussed in chapter 4, z_{50} is calculated using Equation 6.1.

$$z_{50} = \frac{\tau_{ult}}{E_s} \quad (6.1)$$

Where: z_{50} = the displacement at which 50% of the ultimate capacity of the spring is reached
 τ_{ult} = ultimate capacity of the spring
 E_s = initial tangent of the t-z curve, or stress-strain curve (N/m^3)

For sands, the initial tangent values are based on the hyperbolic relationship between skin friction and displacement as suggested by Mosher [10] which is solely dependent on the angle of internal friction ϕ . The values for initial tangent from Mosher have been interpolated and extrapolated for ϕ , so that they include more types of sand. The resulting values are listed in Table 6.1. For clays, the initial tangent is based on data from geotechnical software manufacturer, GEO5 [11].

Table 6.1: Initial tangent vs internal friction angle for sands with extrapolated values [10], and initial tangent with corresponding undrained shear strength for clays [11].

| E_f (psi/in) | Sands | | Clays | |
|----------------|---------------|------------|---------------|-------------|
| | E_s (MPa/m) | ϕ (°) | E_s (MPa/m) | c_u (kPa) |
| 15.5 | 4.2 | 24.8 | 8.5 | 15.0 |
| 30.6 | 8.3 | 26.6 | 15 | 30.0 |
| 45.6 | 12.4 | 28.0 | 32.5 | 57.5 |
| 60.7 | 16.5 | 30.3 | 75.0 | 112.5 |
| 75.8 | 20.6 | 32.1 | 137.5 | 225.0 |
| 90.9 | 24.7 | 33.9 | 200.0 | 300.0 |
| 105.9 | 28.8 | 35.7 | | |
| 121.0 | 32.9 | 37.6 | | |
| 136.1 | 36.9 | 39.4 | | |
| 151.2 | 41.0 | 41.2 | | |
| 166.3 | 45.1 | 43.1 | | |
| 181.3 | 49.2 | 44.9 | | |
| 196.4 | 53.3 | 46.7 | | |
| 211.5 | 57.4 | 48.5 | | |

The OpenSees TzSimple1 element that is used to construct the t-z spring behavior, is based on a paper by Boulanger et al. [29]. In the paper, equations are presented describing a p-y element, which is the horizontal equivalent of a t-z element. The element is divided into two parts, see Figure 6.2, consisting of a near-field plastic spring in series with a far field elastic spring [99]. A damper in parallel with the far-field elastic spring represents radiation damping [99].

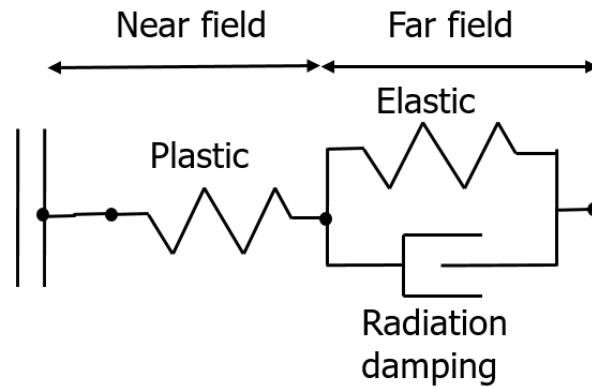


Figure 6.2: Construction of a t-z element as proposed by Boulanger et al. [29].

The plastic spring behavior is described by Equation 6.2, the elastic spring is described by Equation 6.3 [99]. Due to the addition of a plastic spring, the t-z element automatically accounts for hysteresis if a cyclic load is applied to the pile.

$$t^p = t_{ult} - (t_{ult} - t_0^p) \left[\frac{c z_{50}}{c z_{50} + |z^p - z_0^p|} \right]^n \quad (6.2)$$

Where: t^p = plastic part of force in element (N)
 t_{ult} = the ultimate static capacity of the soil (N)
 z_{50} = the displacement at which half the ultimate capacity of the soil is reached (m)
 t_0^p = t^p at the start of the current plastic loading cycle (N)
 z^p = plastic z-displacement (m)
 z_0^p = z at the start of the current plastic loading cycle (m)
 c = a constant controlling the tangent modulus at the start of plastic yielding
 n = an exponent controlling the sharpness of the $t - z^p$ curve

$$t^e = C_e \frac{t_{ult}}{z_{50}} z^e \quad (6.3)$$

Where: t^e = elastic part of force in the element (N)
 C_e = a constant defining the normalized elastic stiffness
 z^e = elastic z-displacement (m)

The ratios and constants that are used in the previous equations are pre-selected by OpenSees which provides two options, representing t-z curves in sands and shafts drilled into rock and clays. For sands, the following parameters are chosen so that the t-z curves follow the backbone of those provided in the paper of Mosher et al. [10]: $c = 0.6$, $n = 0.85$ and $C_e = 2.05$. For clays, the model proposed by Reese and O'Neill for drilled shaft capacities is used as a backbone for the t-z curve, corresponding to the following parameters: $c = 0.5$, $n = 1.5$, and $C_e = 0.708$ [100].

6.1.2. Pile elements

The pile nodes are connected by elastic elements using the elasticBeamColumn type of element. This elastically behaving element carries all the inertia and stiffness information of the pile that was listed in Table 3.1. Remaining input parameters are determined by Equation 6.4, Equation 6.5 and Equation 6.6 and listed in Table 6.2.

$$I_{xx} = I_{yy} = \frac{\pi}{64} (D_o^4 - D_i^4) \quad (6.4)$$

$$I_{zz} = \frac{\pi}{32} (D_o^4 - D_i^4) \quad (6.5)$$

$$A = \frac{\pi}{4} (D_o^2 - D_i^2) \quad (6.6)$$

Table 6.2: Elastic beam column command input parameters.

| Parameter | Value | Unit |
|----------------------|---------|-------|
| Area | 1.614 | m^2 |
| Young's modulus | 210 | GPa |
| Shear modulus | 80 | GPa |
| XX moment of inertia | 8.314 | m^4 |
| YY moment of inertia | 8.314 | m^4 |
| ZZ moment of inertia | 16.628 | m^4 |
| unit mass | 12585.3 | kg/m |

6.2. Integrator types

In OpenSees, different types of integrators are available for static and transient analyses to solve the governing differential equations of any problem. In a static analysis, the equations of motion are solved without damping or mass matrices which simplifies the system to the equation $KU = R$, where K is the stiffness matrix, U the displacement of a node and R the response of a node. In this thesis a static analysis is only used to apply gravity, which is an arbitrary procedure in OpenSees and will not be discussed, but is present in Appendix H to allow for reproduction of the experiments. For transient analyses, several choices for integrators exist. Various factors should be considered when selecting an integrator, such as high-frequency mode dissipation (often called numerical damping), stability and second-order accuracy. Numerical damping is often necessary in a numerical simulation due to FEM models inability to accurately represent high-frequency modes due to poor spatial discretization [101]. Some integrators can filter these high-frequency oscillations by numerical damping. Stability in numerical algorithms is concerned with spurious fluctuations in the initial data, or the growth of round-off errors, causing large deviations of the final answer from the exact solution [102]. If these errors are damped, the method is called stable, if not, the method is unstable. In non-linear problems, stability is uncertain and the stability of a method cannot be assured by definition. Second-order accuracy quantifies the error between the numerical approximation and the exact solution to the differential equation. In other words, it tells something about the magnitude of the numerical error. Its definition is given by Equation 6.7.

$$E(h) = \|u - u_h\| \leq Ch^n \quad (6.7)$$

Where: $E_n(h)$ = error size

h = some characterizing parameter, usually time-step

u = the exact solution to the differential equation

$u(h)$ = the numerical solution or approximation

C = a constant independent of h

n = the n -th power, determining the order of accuracy

Three of the most extensively used integrators will be discussed as well as their pros and cons. These are the Newmark method, Hilber-Hughes-Taylor (HHT) method and the Chung and Hulbert (CH) or generalized α method. The trade-off between integrator types is always between computational time and accuracy, and reaching a combination of the two is desired.

6.2.1. Newmark method

The Newmark method is -in OpenSees- an implicit integration method used for solving the differential equations that make up the EOM of the system. It is one of the quickest and simplest integration methods, hence

the reason for its widespread applicability [101]. A downside of the Newmark method is that it results in excessive numerical oscillations [101]. It is possible to add numerical dissipation into the Newmark method but then it is no longer second-order accurate. In OpenSees, the Newmark method comes in several forms, depending on the selection of the input parameters γ and β as shown in Table 6.3. As can be seen in the table, the Newmark method simplifies to other methods depending on the input parameters.

Table 6.3: Newmark method input parameters [12] and corresponding names of methods.

| Method | γ | β |
|-----------------------------|----------|--|
| Central Difference method | 0.5 | 0.0 |
| Average acceleration method | 0.5 | 0.25 |
| Linear acceleration method | 0.5 | 0.167 |
| Other, with dissipation | > 0.5 | $0 < \beta < 1$ & $\beta \neq 0.25$ |

In case of the central difference method, where β is 0, the Newmark method is an explicit method [12]. For all others the method is implicit. The average acceleration method, is unconditionally stable (for linear problems) and does not include numerical damping. The Newmark method is unconditionally stable if $2\beta \geq \gamma \geq \frac{1}{2}$, thus the linear acceleration method for example, is conditionally stable. Choosing $\gamma > 0.5$ introduces numerical damping into the solution. The method is second order accurate only if γ is chosen as 0.5. The Newmark method has problems with oscillations in OpenSees when the TzSimple1 element is implemented in the model. These oscillations have been observed even under a very simple loading applied to the model, and thus the method as a whole is not used.

6.2.2. Hilber-Hughes-Taylor

The Hilber-Hughes-Taylor (HHT) method is an implicit integration method allowing for energy dissipation while keeping the method second order accuracy [12]. The HHT method, in contrast to the Newmark method, filters unwanted high-frequency modes rather than amplifying them [101], and attempts to achieve this damping without harming the order of accuracy [103]. The method, for linear problems, can be unconditionally stable depending on input parameters [12]. The input parameters for HHT are shown in Table 6.4.

Table 6.4: HHT input parameters [12].

| | α | γ | β |
|--------------|------------|----------------|--------------------------|
| Newmark | 1.0 | - | - |
| standard HHT | 0.67 - 1.0 | $1.5 - \alpha$ | $\frac{(2-\alpha)^2}{4}$ |

The parameters γ & β are optional and the default values are shown in the table. These default values ensure the method is second order accurate and unconditionally stable if $\frac{2}{3} \leq \alpha \leq 1.0$. The closer α is to 0.67, the greater the numerical damping. The HHT method shows good convergence results for the particular model used in this research and does not show any unwanted numerical oscillations when α is set to 0.67.

6.2.3. Generalized- α

The generalized- α method, or CH method, which is often used in the field of structural dynamics generally shows good results in FEM models with geotechnical applications [101]. Just as the HHT method before, this implicit method allows for high energy dissipation and second order accuracy [12]. In general, this method is better at filtering high-frequency modes only while keeping medium to low frequencies unaffected [101]. Depending on the choices of input parameters the method can be unconditionally stable [12], these are listed in Table 6.5.

Table 6.5: Generalized- α method parameters.

| | α_M | α_F | γ | β |
|-------------------|--------------------|--------------------|-----------|-----------|
| Newmark | 1.0 | 1.0 | ambiguous | ambiguous |
| HHT | 1.0 | $\neq 1.0$ | ambiguous | ambiguous |
| Chung and Hulbert | $0 < \alpha_M < 1$ | $0 < \alpha_F < 1$ | ambiguous | ambiguous |

The method is second-order accurate if $\gamma = \frac{1}{2} + \alpha_M - \alpha_F$ and unconditionally stable provided that $\alpha_M \geq \alpha_F \geq \frac{1}{2}$ and $\beta = \frac{1}{4} + \frac{1}{2}(\gamma_M - \gamma_F)$ [12]. Again, γ & β are optional and the default values make sure that the method is unconditionally stable, second order accurate and high frequency dissipation is maximized. The default values are $\gamma = \frac{1}{2} + \gamma_M - \gamma_F$ & $\beta = \frac{1}{4}(1 + \gamma_M - \gamma_F)^2$.

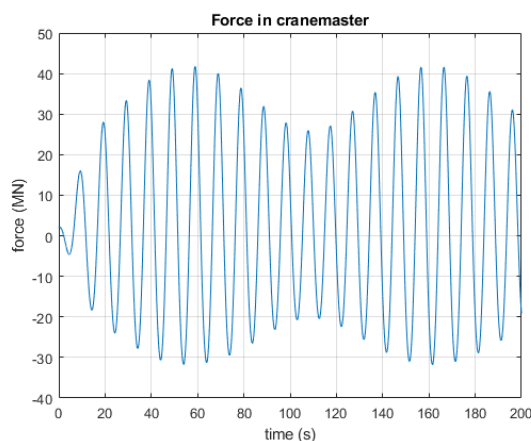
7

Results and Discussion

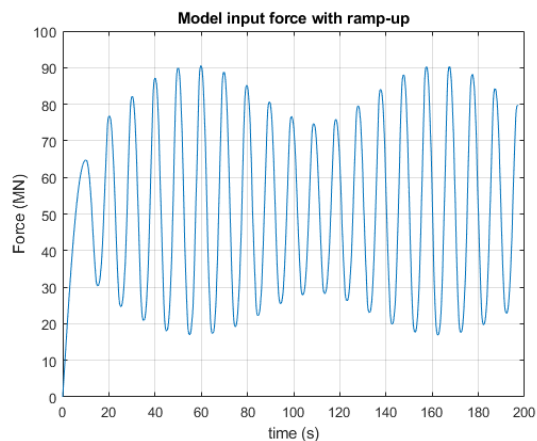
This chapter presents the outcomes of the two models and discusses the results by diving into the limitations and boundary conditions of both models. First, the results will be discussed, then in section 7.8 the discussion will be presented.

7.1. Vessel model results

First, the force graphs that are the result of the vessel model will be discussed. Figure 7.1a shows the force in the cranemaster for a simulation time of 200 seconds. Two frequencies can be distinguished from the graph, one with a relatively small period of approximately 10 seconds, and one with a larger one of approximately 100 seconds, indicating beating of the signal. Beating is a phenomenon where constructive and destructive interference of two waves with different frequencies create a new frequency in the resulting wave pattern, equal to the absolute value of the difference between the original two frequencies. Figure 7.1b shows the force that is used as an input in the OpenSees model. The first 10 seconds of the time-series consists of a ramp-up part, allowing the FEM model to respond gradually to the amplitudal force since it consists of a dynamic analysis. The addition of this ramp-up force also makes sure that OpenSees does not have to deal with the harmonic oscillations present in the first seconds of Figure 7.1a. These oscillations are the result of the fitting method MATLAB uses to approximate the cranemaster's stiffness and damping, and the fact that the tensioning procedure is not implemented in MATLAB.



(a) Cranemaster force.



(b) OpenSees model input force constructed from the cranemaster force of Figure 7.1a and a ramp-up part.

Figure 7.1: Output of the vessel model in terms of cranemaster force. Together with the ramp-up, the force represented in the right graph serves as the input of the pile-soil model.

7.2. Hysteresis

The response of the OpenSees model to the input force of Figure 7.1b is shown in Figure 7.2. These results are obtained from a 100 second simulation of a pile in sand with an ultimate capacity of 108.3 MN. The figure shows that the OpenSees model is sensitive to the maximum force in time that is applied. In the first 25 seconds, the force stays below 80 MN, which is far below the ultimate capacity and consequently, the corresponding displacements in Figure 7.2 are relatively low. When the input force comes above 80 and eventually 90 MN, the corresponding displacements become larger, and especially the plastic displacement increases. The latter can be observed from the relatively large horizontal spaces between the hysteresis cycles in the middle part of Figure 7.2.

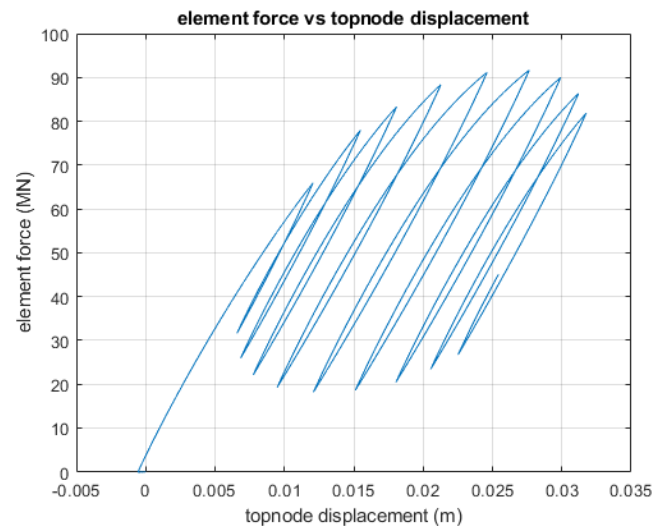


Figure 7.2: Response of OpenSees model to force input of Figure 7.1b, showing hysteresis behavior.

7.3. Varying amplitude

This section presents results of amplitude variation of the crane-master force and the effect this has on pile displacement. As was shown in the previous section, the maximum applied force in time has a large influence on the pile displacement. Because of this sensitivity, the tensional part of the input force is varied in coordination with variation of the amplitude, so that the maximum applied force in time stays constant. This can be observed by looking at the top-left, top-right and bottom-right graphs of Figure 7.3, where the red line indicates the maximum applied force in time, which is equal for all three graphs. Variation of the input force amplitude is achieved by multiplying the crane-master force in the EOM in the MATLAB model by 0.33 and 0.67 respectively. The maximum force in time comes relatively close to the ultimate capacity of the pile so that plastic strain accumulation can properly be observed. The simulation time has been increased to 500 seconds to make the results more apparent.

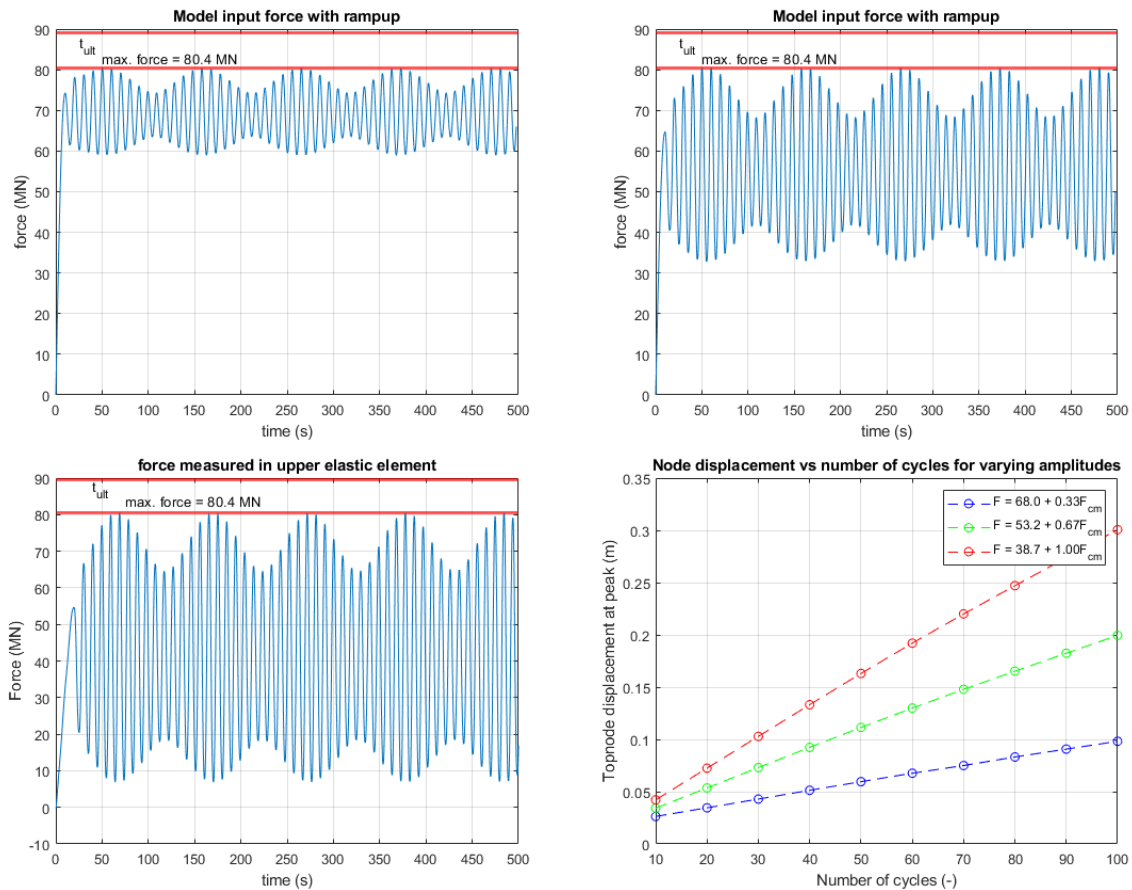


Figure 7.3: Results of pile-soil model to input force amplitude variation. Top and bottom left figures: applied force versus time, top red line represents the ultimate capacity of the pile equal to 89.1 MN, the bottom red line highlights the maximum applied force, equal to 80.4 MN in all cases. Bottom right: topnode displacement vs number of cycles for all three cases.

The effect of force amplitude variation becomes apparent when looking at the bottom right graph of Figure 7.3. As the simulation progresses and more force cycles are applied to the pile, plastic strain accumulates more when the full F_{cm} is applied. The total pile displacement after 100 cycles is three times as large when compared to the blue line, where 33% of the crane-master force is applied to the pile.

7.4. cyclic vs monotonic load

To see whether applying cyclic loads rather than monotonic loads to the monopile reduces soil resistance, it makes sense to look at the piles response to monotonic loads. Figure 7.4 shows the model response to a monotonic load of 80.4 MN, which is below the ultimate static capacity of the pile. This value of the monotonic load is selected so that the result can be compared to the results of the previous section, where the maximum force in time was equal to this 80.4 MN as well. The results will be compared to the bottom right graph of Figure 7.3 where the full crane-master force is taken into account rather than a fraction of it. To avoid a shock response in the transient analysis of the model, a ramp-up of 10 seconds to the monotonic force was used.

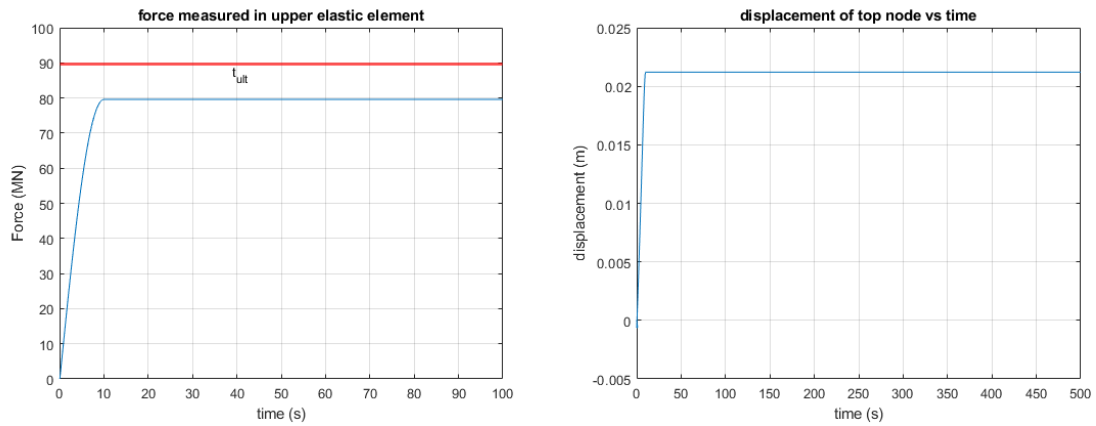


Figure 7.4: Response of model to monotonic load of 80.4 MN with a ramp-up. Left: force measured in top element of pile vs time, right: displacement vs time response.

The total displacement resulting from monotonic loading is 0.0221 meters, or 22.1 mm, and stays constant (Figure 7.4). When looking at the bottom right graph of Figure 7.3, the total displacement after 50 cycles (corresponding roughly to 500 seconds of simulation) is about 0.16 meters, or 160 mm. This results in a displacement increase of more than 600 % over a time period of 500 seconds. Increasing the number of cycles further has a positive impact on the total pile displacement as plastic strains continue to accumulate with each cycle.

7.5. Varying tension

Another result that can be obtained from the soil model is the response of the monopile to forces with varying tension. While keeping the amplitude of the forcing constant, the ramp-up or tensional part of the force is varied, resulting in variation of the red tension line in the left figure of Figure 7.5. The ultimate capacity of the pile is 89.7 MN and is never surpassed by the applied force. It is obvious that increasing the tension, has a positive effect on topnode displacement and this effect is largest when the maximum applied force in time comes close to the ultimate capacity of the pile. In the right graph this effect is visualized since the displacement of the red line increases more than the other two with every load cycle. The same applies to the green line with respect to the blue line.

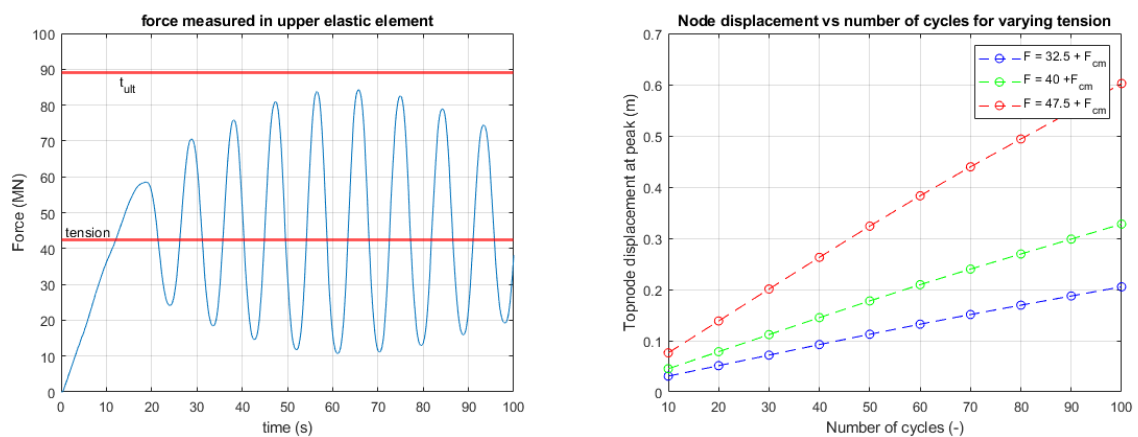
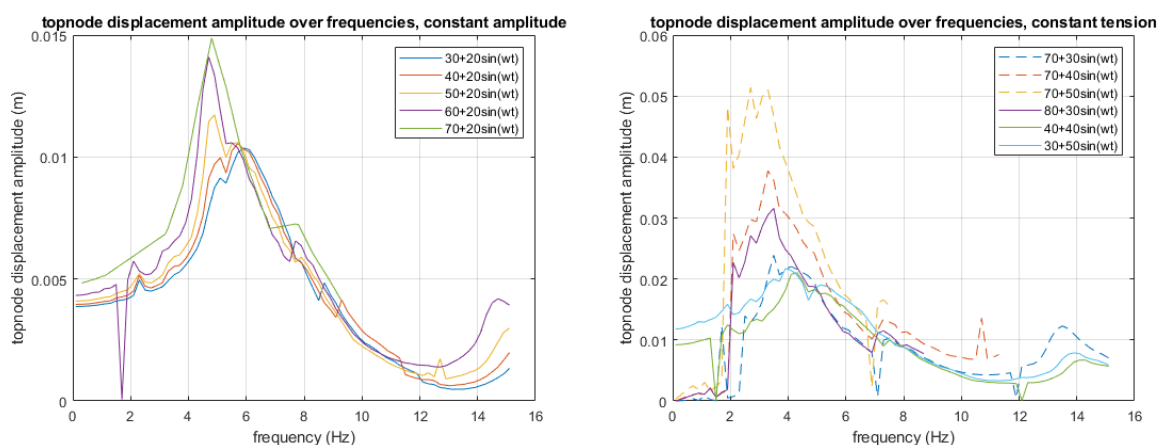


Figure 7.5: Results of varying tension and its effect on final displacement of the topnode. Left: example of the input force, with τ_{ult} and tensional part represented by red horizontal lines. Right: topnode displacement vs number of cycles for three different tension forces.

7.6. Resonance frequency

The resonance frequency of the pile-soil system is dependent not only on the system parameters, but also the force input parameters, such as amplitude and tension, because there are non-linear springs in the system. Understanding the response of the model to these different force input characteristics generates a lot of knowledge and insight into the model. An analysis is performed to find the resonance frequency of the model at different forcing amplitudes and tension. The parameter that is checked for resonance is the topnode displacement amplitude. However, since the applied force is harmonic, the topnode displacement is also harmonic and taking an arbitrary value in the time-series would result in errors. To omit this problem, the amplitude of the node displacement is used, while making sure that the steady-state response has already been achieved in every simulation. Figure 7.6a is obtained by varying the tension and keeping the amplitude constant. Doing the same for constant tension and varying amplitude results in Figure 7.6b. Note that in the production of these results the input force of the OpenSees was a perfect sine with a ramp-up, resulting in one-way cyclic loading, rather than the previously presented crane-master force.



(a) Topnode displacement amplitude at steady-state, for different forcing frequencies as input force. Graph shows the model response to input forcing with constant force amplitude and varying mean force.

(b) Topnode displacement amplitude at steady-state for different forcing frequencies as input force. Graph shows model response to input forcing with constant tension and varying amplitude, as well as some arbitrary forces.

Figure 7.6: Resonance frequency of the pile-soil model for different input forces, a) constant amplitude and b) arbitrary forces including constant tension of 70 MN. On the y-axis the amplitude of topnode displacement at steady-state is plotted.

Figure 7.6a shows a trend of increasing node displacement for increasing tension in the applied force. This is explained by the previously found result that larger applied forces in time result in larger displacements of the pile. Another interesting observation from Figure 7.6a, is that the resonance frequency increases when the tensional part of the input force becomes smaller, i.e., when the tensional share of the total force decreases.

Looking at Figure 7.6b, it can be seen that the frequency at which resonance occurs increases when the amplitude of the input force decreases. The smaller the input force frequency is, the larger the frequency at which resonance occurs will be.

The same trends can be observed in resonance graphs that show the soil response rather than pile displacement. The soil response is represented by the force in the t-z elements, and by looking at the force amplitude in these elements following the same procedure as for the displacement graphs, resonance frequency graphs like Figure 7.7 are obtained. To capture the entire soil response, the summation of all force amplitudes in every t-z element along the pile is taken.

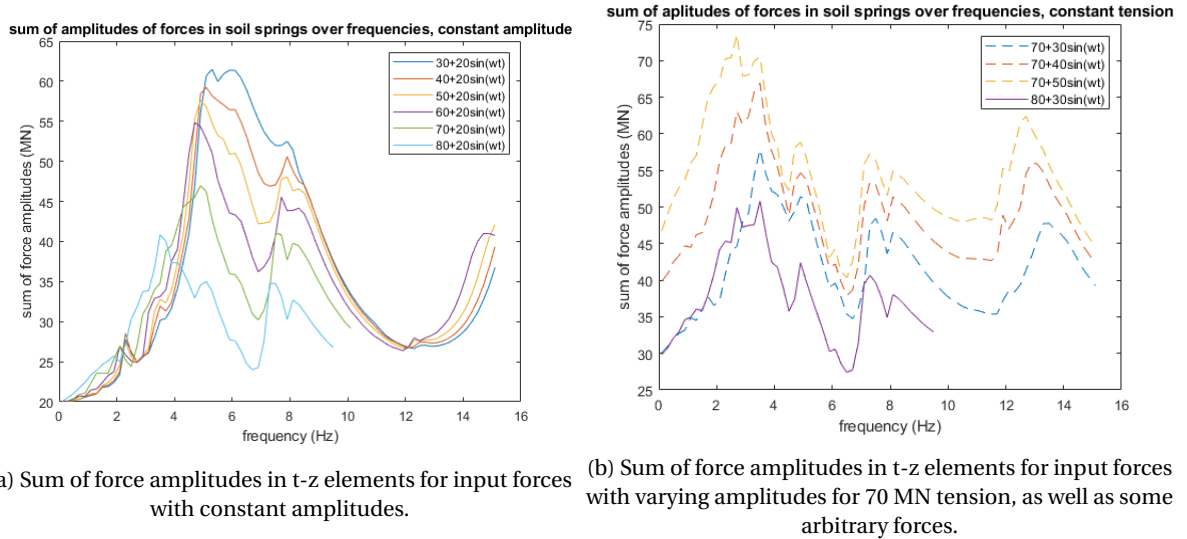


Figure 7.7: Resonance frequency analysis of the pile-soil model for different input forces, a) constant amplitude and b) arbitrary forces including constant tension of 70 MN. On the y-axis the sum of amplitude of force in all soil spring elements is plotted.

Figure 7.7a shows an increase in soil response when the tensional part of the input force decreases. This could possibly be explained by the non-linearity of the system, as a larger force is applied to the system, there is more damping and the response of the t-z elements is damped. However, closer examination and modelling should point out if this explanation is accurate. Figure 7.7a also shows the earlier observed trend where the resonance frequency increases when the tensional part of the input force decreases. Figure 7.7b also shows the earlier found relationship between resonance frequency and input force amplitude from Figure 7.6b. It clearly shows that the resonance frequency increases as the amplitudal part of the input force decreases.

7.7. Clay vs Sand

Another interesting find is the difference in response to cyclic loads between clays and sands. Looking at Figure 7.8, it can be observed that the response of clays to cyclic loading is different than that of sands. The two figures are obtained from applying the exact same cyclic force to the monopile. Figure 7.8a shows less plastic strain accumulation than Figure 7.8b.

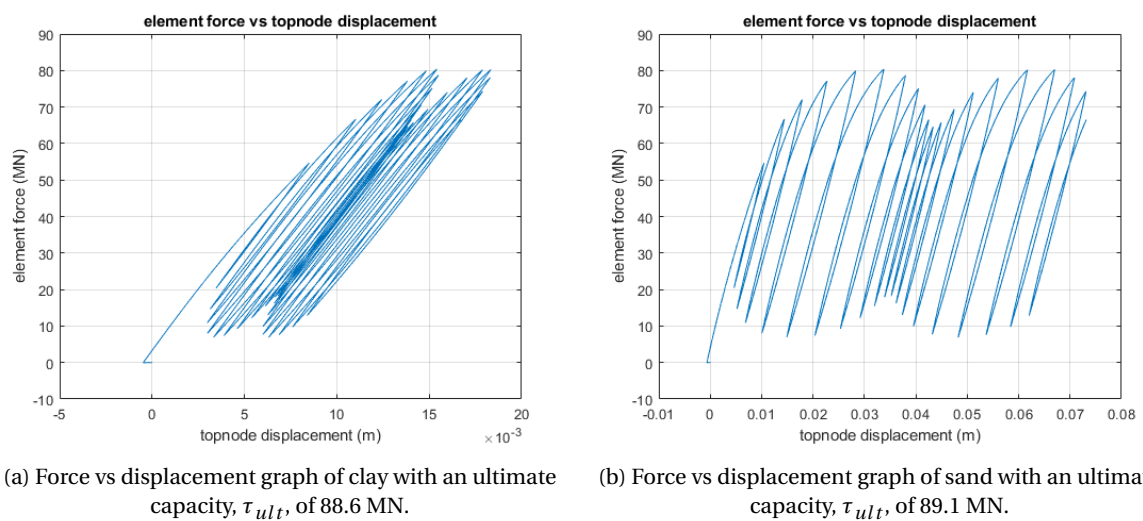


Figure 7.8: Force vs displacement curves showing the difference in response to cyclic loads of clays and sands. In both cases the exact same cyclic load was applied.

7.8. Discussion

All models are a simplified version of reality. By making assumptions and considering which phenomena are important enough to take into account and more importantly, which are not, predictions can be made about real world applications and problems. The reliability, accuracy, and truthfulness of the outcome of such models, lies in full with the assumptions that are made along the way to create it. This section discusses the results of the two models and looks critically at the assumptions that have been made along the way. The most important ones, those that have the largest influence on the results, will be discussed extensively, as well as the limitations and boundary conditions under which the model remains applicable.

7.8.1. Vessel model

The most influential assumption and simplification that has been made in the vessel model, is the assumption that the motion of the beam tip can be described by a perfect sine. In the model, the forcing terms, F_a , and M_a , are calibrated to match a perfect sinusoidal motion that is constructed using a motion report. In the real world, the vertical motion of the beam tip will not be a perfect sine with a constant amplitude and frequency, but a summation of multiple sines. The motion of the beam tip consists of the addition of numerous sines with different amplitudes and frequencies, creating an irregular displacement pattern. If this were to be implemented in the model, the crane-master force would be more irregular in terms of amplitude and frequency. This will have a significant effect on pile displacement, as it was shown that pile displacement is largely dependent on the combination of crane-master force amplitude and tension. Additionally, the beam tip motion is calibrated to a sea state of $H_s = 2.5m$ and $T_p = 7.74s$, because these represent the most rough conditions under which the JLS is able to operate. Assuming that this sea-state is constant is a very convenient assumption, making the hydrodynamic model non-conservative. A downside of aiming to operate at such rough sea-states is that the operationability window is small, as operations must be stopped if conditions get more severe.

A second limitation is the fact that the vessel model only considers one frequency of motion of the vessel in both heave and pitch motion, rather than considering the abundant amount of frequencies present in an actual sea state. The added mass and damping are only determined for these forcing frequencies, rather than determining them for every frequency at which the vessel moves as a result of a wave spectrum. The model also does not take roll of the vessel into account, where in reality, roll can result in vertical displacements of the beam tips. However, since the model assumes that there is only one beam, adding roll would not affect the results significantly.

Another simplification implemented in the model is the way that the stiffness of the two JLS beams and the derrick hoist are accounted for by the stiffness reduction factor, k_f . The value of $k_f = 0.5$ discussed in section 5.3, is based on interviews with Allseas experts [18], rather than being determined analytically. Since there is no fundamental basis for this value of 50%, a sensitivity analysis has been performed, to see what the influence of any deviation would be. A decrease of 50% to a k_f of 0.25, results in a minimal decrease in maximum crane-master force amplitude. A 50% increase, to a k_f value of 0.75, results in a small increase in maximum crane-master force amplitude. This makes sense, as the stiffness of the wire cables is extremely large with respect to the crane-master stiffness. Decreasing or increasing an already large stiffness has little to no effect on the displacement of the crane-master, since the stiffness of the crane-master dominates its displacement. In both cases, the model experiences the wire cables as rigid. Moreover, the two beams of the JLS are modelled as one, rigid beam, that is unable to bend, while in reality, these are two elastic beams, which will bend when loaded up to its maximum lifting capacity. Likewise, the representation of the six crane-masters by a single system of spring-dampers is an oversimplification.

The vessel model assumes that the monopile is stuck at the beginning of loading, and remains stuck during the simulation. In reality, the pile will start moving and deforming as soon as a certain threshold force is exerted on it. This will have an effect on the motion of the vessel. Since it is assumed that the top part of the pile is fixed during the vessel model simulation, elasticity of the pile is not taken into account in the vessel model. However, since the OpenSees model only simulates the first moments of extraction where displacements are small, the effect of pile displacements on vessel motion are assumed to be negligible. This effect should be accounted for if the soil model is extended to include large pile displacements.

The tensioning procedure as proposed in chapter 3 is not included in the model as it starts at a stroke length of 2 meters, corresponding to half the stroke of the crane-master. Additionally, the operationability aspects of the proposed system have not been thoroughly examined in this thesis. Using numerous crane-masters of these

dimensions has never been performed in an offshore environment, and more investigation and consideration is necessary before such an operation can be carried out.

Lastly, regarding the pitch motion of the vessel, it has been assumed that the vessel rotates around its Centre of Gravity whereas in reality, it will rotate around the constantly changing Centre of Flootation (CoF). This point, which represents the CoG of the water plane area of the vessel, moves around when the vessel rotates. The difference between the CoG and CoF is never large enough to have a significant effect on the outcome of the model, especially because the error is much smaller than the 217 meter arm between the CoG and the beam tip.

7.8.2. Soil model

A downside of using uncoupled t-z springs to model soil response, is that locality is not included in the model, and each segment of the soil is modelled as a separate segment. In reality, soil layers are not discrete and the behavior of one soil layer is dependent on the behavior of the surrounding layers as well. It is a continuous medium that interacts with itself and the pile over the complete depth of the pile-soil interface. However, modelling the pile-soil interaction with such uncoupled springs, has delivered satisfactory results in the past and thus this method is adopted. Additionally, this thesis only considers homogeneous soil layers, rather than heterogeneous soil compositions that one encounters in offshore conditions. This was done to ensure widespread applicability of the model, as it is relatively easy to change the inputs of the t-z springs at certain depths to represent various soil compositions. This way, the model can be applied to any soil structure and composition that might be encountered offshore, be it in the North Sea or anywhere else. Additionally, radiation damping is not included in the model, which makes the pile displacements non-conservative. In a real world application, radiation damping will have a negative effect on pile displacement. This effect however, becomes less when heterogeneous soil compositions are considered, according to Mylonakis et al. [104].

The description of soil behavior under cyclic loading is also limited. In the OpenSees model, the soil is represented by t-z springs, which are calibrated based on data by either Reese & O'Neill [100] or Mosher [10] if clays or sands are considered respectively. While these curves describe soil response accurately enough for monotonic loads, they do not update them when cyclic loads are applied. The backbone of the t-z curves remains constant during the simulation and the yield surface does not move. This effect, which is called isotropic hardening if the surface expands during the simulation, and kinematic hardening if the surface is transposed, is used in constitutive soil models. In such models, void ratio, pore pressure and other geotechnical parameters are included and updated, allowing for a more accurate description of soil behavior and stiffness. Absence of these stiffening effects does not necessarily mean that the results obtained from the current OpenSees model are untrue since the calibration of the t-z springs is still based on field tests.

The submerged unit weight of soil is kept constant at 10 kN/m^3 throughout this whole thesis. While this is a representative value, larger values have been encountered at offshore sites in the North Sea. For example in the geotechnical investigation report for Hollandse Kust Zuid carried out by Fugro [105], submerged unit weight of soil layers of 12 kN/m^3 have been observed. A larger submerged unit weight will have a significant effect on the ultimate capacity of the pile and the value taken in this research might result in an underestimation of the ultimate static capacity in the most heavy soils. On the other hand, it is unlikely that such a large submerged unit weight of soil is present along the entire embedded length of the pile. In reality, often several different soil layers are found at every location in a wind farm, both with high and low submerged unit weights, and often the first several meters have a lower submerged unit weight resulting in a lower ultimate static capacity. Taking a mean value of 10 kN/m^3 might thus be a conservative assumption, but this is site specific.

The current model is built with a focus on the first moments of a complete removal, where the pile transitions from a stuck condition to a condition where it starts moving and achieves a velocity. When plastic strain increases and displacements become increasingly large, the model is unable to accurately represent soil resistance. This is attributed to the inability of the t-z elements to be switched off at depths that the lower end of the pile has already passed. As a consequence, the bottom t-z element will always exert a force on the monopile equal to its ultimate capacity, even though in reality, the pile is no longer in contact with that soil layer. This limits the applicability of the current model to small pile displacements and the first moments of lifting.

Concluding, the hydrodynamical model overestimates the motions of the beam tip which results in an over-

estimation of the crane-master force. Additionally, the assumed sea-state of $H_s = 2.5\text{m}$ and $T_p = 7.74\text{s}$ is very specific, and it is uncertain how often this sea-state is encountered. Adding that the operationability window is small for this specific application, it can be concluded that the hydrodynamical aspect of this thesis is not in favour of completely removing the largest and heaviest monopiles this way. The soil model on the other hand, is considerably conservative because of the assumption that the entire inside of the pile is filled with soil, and the submerged unit weight of soil is considered constant at 10 kN/m^3 . As a result, the ultimate static capacity of the worst-case pile might have been overestimated, and complete removal might be more feasible than the results in this thesis indicate.

8

Conclusion

The objective of this thesis is to investigate the possibility of soil resistance reduction by utilizing vessel motion for the decommissioning of offshore wind turbine monopile foundations. To investigate this matter, the following main research objective has been established:

"Developing a dynamical interaction model between the Pioneering Spirit and a monopile describing the first moments of a complete removal, with an emphasis on soil-resistance reduction by utilizing vessel movement."

This chapter answers the sub-research questions and provides conclusions that can be drawn from the answers. The conclusions to the sub-questions in consecutive order will be followed by the conclusion that can be drawn regarding the main research objective.

From the performed market study, it can be concluded that monopiles to be decommissioned over the next decade typically are relatively small with respect to those that are installed in recent years, in terms of pile length, weight, diameter, installed capacity, and the water depth in which they stand. Interestingly, the embedded length of the pile has remained constant, at a range of 30 to 40 meters for most farms. Almost all of the first generation wind farms utilize a grouted connection between the monopile and the transition piece. The worst-case monopile that is selected as a representative maximum for the first generation piles has a length of 75 meters, embedded length of 40 meters, diameter of 6.5 meters and wall thickness of 80 mm. The first generation of monopiles is defined as piles installed before 2016, as these are all designed to last for 20 to 25 years and share approximately the same dimensions when compared to second generation piles. The design life of the second generation monopiles, which are installed after 2016, is often 40 and sometimes even 50 years. Consequently, these piles will not have to be decommissioned (on a large scale) for a long time.

Based on calculation methods for the ultimate static capacity of piles prescribed by DNV, API, and ISO, it can be concluded that the ultimate static capacity of the considered worst-case monopile lies, in the most stiff clays, north of 200 MN. This means that the lifting capacity of any crane aboard the existing fleet of heavy lift vessels worldwide, is insufficient to completely remove this pile by using blunt force. This remarkable conclusion indicates the lack of forward planning that has gone into decommissioning during the installation of offshore wind farms. It is expected however, that smaller piles than the considered worst-case pile, as well as piles that stand in less stiff clays, can be completely removed by using the JLS of the Pioneering Spirit, as their ultimate capacity lies below its 20.000 ton lifting capacity. The largest ultimate static capacities are the result of skin frictional forces on the outside and on the inside of the pile, since a plugged scenario results in a lower extraction force, as pile plug weight is far less than the inside skin friction. It is found that cohesive soils present the largest problem from a complete removal point of view, which is solely caused by the unit skin friction for the stiffest clays.

From the constructed hydrodynamical model in MATLAB, it can be concluded that its output is highly sensitive to the stiffness and damping properties of the cranemaster unit. The choice for a certain cranemaster should thus be carefully considered and thought needs to be put into the settings of the input pressure, which determines the stiffness and damping at a certain stroke and stroke speed. The constructed hydrodynamical

model makes favourable assumptions so that a large beam tip motion with a relatively constant amplitude and frequency is obtained. These assumptions make the model non-conservative and in reality, such motions are more irregular and it is expected that the mean of the crane-master force amplitude is lower in a real life application.

From the OpenSees pile-soil model, it can be concluded that increasing the amplitudal part of the input force results in larger monopile displacements, as the plastic regime of the t-z element is reached more often and for a longer duration of time. This way, larger plastic strains accumulate with each cycle than for smaller amplitude input forcing, and larger displacements are achieved. A second conclusion is drawn from the sensitivity of the model to large forces: the mean, tensional part of the input force also contributes significantly to pile displacement. The combination of high tension with a large amplitude will result in the largest plastic strain accumulation, since the non-linear behavior of the t-z elements at relatively high forces results in large plastic strains.

Thirdly, it can be concluded that the hypothesis that cyclic degradation can be achieved by loading the pile cyclically is proven to a certain extent. Under monotonic loads lower than the ultimate pile capacity, the displacement of the pile is constant and does not accumulate while under cyclic loads strain accumulation is observed. As time progresses and the number of cycles increases, it is expected that the accumulation of plastic strains will eventually lead to large monopile displacements. The effect of a large input force amplitude is twofold: a) the maximum force in time, consisting of the tension added to the force amplitude, comes closer to the ultimate capacity of the soil, resulting in larger plastic displacements; b) as the amplitude increases, the part of the cycle where plastic displacement occurs, occurs over a longer period of time.

Comparing the results for pile displacements under cyclic and monotonic loads, it can be concluded that in sands, the cyclic loads induce greater displacements after a small number of cycles, and displacements accumulate with an increasing number of cycles. In clays, plastic strain accumulation was observed to be lower when applying the same force. This can mainly be attributed by the fact that the t-z elements are calibrated differently for both soils. For clays, Reese & O'Neill provide backbone t-z curves, while for sands, Mosher provides backbone t-z curves. The z_{50} input parameters also plays a large role in the behavior of the element to cyclic forcing. It might be the case that in clays, the elastic spring in the t-z elements, relatively covers larger displacement with respect to the elastic spring in the t-z element in case of sands. This would mean that plastic strains are achieved at relatively larger displacements in clays.

Fourthly, from the resonance frequency analysis in sands, it is concluded that the largest reaction forces of the soil are observed at forcing frequencies between 4 and 7 Hz, depending on the input force characteristics. Therefore, it is in the interest of achieving maximum pile displacement to find a way to increase the frequency of vessel motion to these higher frequencies. This is attempted in the subsequent recommendations chapter, chapter 9.

In general, from the constructed models it can be concluded that, at small displacements, the proposed method is able to achieve plastic strain accumulation. The hydrodynamical model overestimates the motions of the beam tip, resulting in an overestimation of crane-master force amplitudes. A more realistic, smaller force amplitude will result in less plastic strain accumulation in the OpenSees model. On top of that, the assumed sea-state that is used in this thesis to create the crane-master force does not occur frequently, which lowers the operationability window of the proposed decommissioning method. The soil model is considerably conservative and in reality, more favourable geotechnical conditions are likely to be encountered. Combining these two facts, it is the authors expectation that the application of the proposed method might work better than the results of this thesis suggest, but only for very specific sea-states and application of the proposed method should be weighed on a case-by-case basis. Before that time comes, numerous improvements have to be made to both the model and the procedure, which will be elaborated on in the next chapter.

9

Recommendations for further research

As was discussed in section 7.8, the pile-soil model is relatively conservative, while the hydrodynamical model makes more favourable assumptions, making it relatively non-conservative. The next sections discuss several recommendations for further research, taking into account the consequences of these assumptions. These are divided into the following four categories:

1. General recommendations on where to go from here with the current research.
2. Improvements and recommendations to the hydrodynamical model.
3. Improvements and recommendations to the pile-soil model.
4. A specific recommendation for the design of a mechanical frequency multiplication device.

9.1. General recommendations

This section discusses the applicability of the proposed method and what specific aspects deserve more attention and consideration for follow-up research by either a Master student, Allseas Engineering or a PhD candidate. Two options are considered.

The first option is to further develop the procedure from an operationability point of view, by answering and addressing the following questions and problems. By looking at the amount time that is required to completely remove one monopile, what would the logistics of decommissioning an entire wind farm look like? How much deck space is required? What specific properties should the crane-master possess and can the description of the crane-master unit in the model be described more accurately? Maybe a new, specifically designed passive heave compensator better suits the proposed removal method. A more accurate representation of the stiffness reduction factor, k_f , can also be investigated, so that the flexibility of the beams, derrick hoist and other JLS components are accounted for as well. Such an extension should also deal with the design of a large-scale connection tool that is able to withstand large dynamic loads, since at the moment of writing, no internal lifting tool for such large pile dimensions exists. However, such detailed design considerations are more applicable in a later stage of technology development, so other recommendations deserve attention first. Especially since the current model is unable to predict soil response at large pile displacements, and consequently, no estimation on complete removal times can be made, continuing the current research with such a follow-up research is considered to be moving too fast.

The second option, which is more appropriate considering the current state of the project, is to switch to a co-simulation of the two proposed models rather than two separate simulations. The current two models run as separate simulations, meaning that one model is run after the other has finished. This way, exchange of information between the two models during the simulation is impossible. It is better to construct one single model that describes the crane-master force at every time-step and then feeds that force as an input to the OpenSees model for that specific time-step. The displacement that comes from the OpenSees model as a result, is then used as input in the MATLAB model again at the next time-step. A large benefit of such a co-simulation model, is that not only the effect of a fixed pile can be incorporated in vessel motion, but also that

of a moving pile. When the pile starts to move upwards, the motion of the vessel is affected which in turn has an effect on the crane force. Switching to a co-simulation will increase the computational time significantly, as information exchange between two separate software packages takes time. The proposed co-simulation is especially convenient when the current OpenSees model is expanded to include large pile displacements. Such a combined model can be modelled in MATLAB by controlling OpenSees as was done in this thesis, but it is also possible to look at other software packages to describe either the hydrodynamic or soil dynamic part of the problem more accurately. For more specifics on expansion of either of the two models, see the next sections.

9.2. Vessel model development

Another option is to improve the vessel model, which can be done for either a co-simulation or the current, separate simulation method. A large improvement of the model can be achieved by replacing the force inputs representing hydrodynamic wave forces by an input that represents an entire sea-state. In the current model, the heave and pitch forcing terms are each described by a single frequency and amplitude in sinusoidal form. Although this approach was sufficient to obtain a representative crane force in this research, using an entire sea-state as input will result in a more realistic description of vessel motion. In such a model, the frequency of vessel motion is likely to be near the resonance frequency. The 6x6 added mass and damping matrices can be taken from Allseas data and fed into the model as inputs; the model then selects the appropriate added mass and damping depending on the frequency of motion at the current time-step.

In the current model, the motion frequency of the vessel is almost equal to the forcing frequency because the model is linear. As a consequence, the frequency of motion of the PS is hardly affected by the fixity condition. By considering multiple frequencies as input signals, the effect of the fixity condition is modelled more accurately, since the model still experiences multiple frequency inputs as the connection between the pile and the crane is made, i.e., when the fixity condition is applied. When this fixity condition is applied, the resonance frequency of the system is expected to change and the motion of the vessel is more accurately represented if a spectrum of input frequencies is used, so that the model can determine at which frequency the vessel will start to move. Another option is to model the fixity condition in hydrodynamic software like OrcaFlex and see what its effect is on the motion frequencies of the vessel. This would be an improvement since it is known that the current model is sensitive to the added mass and damping inputs.

9.3. Soil dynamic model development

An immediate improvement of the soil model can be achieved by modifying the model so that large pile displacements are simulated accurately. This can be achieved by adding a condition to every the t-z element, prescribing that it will stop exerting a force on the monopile if a certain threshold displacement has been achieved. This condition must be applied separately at every t-z element, since the displacement at which it stops working is dependent on depth. This modification allows longer simulation times and can be performed together with the previously suggested co-simulation.

The determination of the initial tangents used in the `TzSimple1` command in OpenSees deserves more attention. The current determination by Mosher for sands and Reese & O'Neill for clays has been performed a long time ago, and the dimensions of monopiles have grown significantly in the meantime. This parameter affects the results a lot, as together with z_{50} it is the sole parameter describing the soils resistance to displacements in the model. A more accurate representation of soil response is captured in models like that of Kementzetzidis [106], for clays and of Wenjuan [88], for sands. In those approaches, constitutive models describe the soils behavior at every moment in time, taking into account locality, cyclic ratcheting (which has previously been called strain accumulation due to cyclic loading), and isotropic and kinematic hardening (which is at the basis of cyclic ratcheting). In such analyses, the yield stress surface of the material is updated during the simulation, meaning that backbone of the t-z curves changes over time. Such a model can also be built in OpenSees. Addition of p-y curves and horizontal motions of the pile can also benefit accurate description of pile extraction behavior. Lastly, finding a way to calibrate and implement radiation damping in the soil can yield more accurate results.

Thirdly, there is a possibility of the creation of a vacuum below the pile upon extraction according to Jardine et al. [79]. Such a vacuum force can be implemented in the model using the `QzSimple1` command, but further research and calibration is necessary for it to be accurately represented in the soil model. It is expected

that vacuum forces are most likely in clays under undrained conditions. Another interesting phenomenon mentioned by the same authors, is that of pile capacity reduction upon re-striking of a pile. This effect can be utilized to lower the ultimate capacity of the pile before it is extracted from the soil, but the current model is unable to simulate this effect. This effect can be simulated if the t-z elements are fit with a condition to represent failure of the soil.

Fourthly, more research should be conducted regarding set-up rates for large scale piles. This can be achieved by monitoring extraction forces during decommissioning campaigns over the following decade. Acquiring more information about this effect on monopiles is of importance since currently, all available data comes from smaller piles used in the O&G sector. Jardine et al. [79] have already conducted similar research for piles up to 507 mm in diameter and their paper can be used to set up similar research for monopiles with larger dimensions.

9.4. Frequency multiplication device

The resonance frequency analysis performed in this thesis, has pointed out that a higher frequency of the force that is applied to the monopile is desired, as this would lie closer to the resonance frequency of the pile-soil system. In a perfect scenario, the 0.1 Hz wave frequency is multiplied to a value lying somewhere between 4 and 7 Hz, depending on the input force characteristics like amplitude and mean tension. Possible ways to achieve such a modification of the input frequency will be discussed later in this section.

To achieve frequency multiplication of a mechanical motion, two types of systems will be considered, consisting of active and passive systems. An active system needs energy input from an external source and most of the time needs to be controlled by external software or operators in order to function as desired. An example of an active system is the Ampelmann bridge, a device that uses feedback loops and controls hydraulic actuators to steady a bridge with respect to wave excitation, so that offshore workers can safely walk from a vessel to an offshore platform or wind turbine. Passive systems do not need such external inputs or energy and generate an output while only using the input signal. An example of a passive system is the cranemaster used in this thesis, that is able to damp out some of the beam tip motion without any external control or addition of energy being necessary.

9.4.1. Passive systems

A passive system, by definition, does not require any additional energy to modify the incoming signal, besides the input. Consequently, due to the law of conservation of energy, the amplitude of any output signal with a frequency that is the multiple of the input signal, must be lower than the amplitude of the input signal. To find passive systems that are able to multiply an incoming frequency, analogies with other fields are explored. Frequency up-conversion is a common type of signal modification in the electromechanical industry, where a high frequency is often desired due to its ability of carrying large amounts of information. It is achieved by use of non-linear circuits where the input signal is distorted, creating a signal with numerous multiples of the input frequency. A bandpass filter then filters the desired frequency. Even though the analogy for frequency up-conversion is applicable, the practical difficulties of applying electrical concepts to mechanical designs are too large. Translating kinetic energy to electrical energy and then to kinetic energy with a higher frequency involves a large loss of energy.

A more promising field where frequency up-conversion is used is in the field of mechanical engineering with compliant mechanisms. A compliant mechanism is a flexible mechanism that transmits motion and forces through elastic body deformation. A compliant mechanism does not have joints, but is of monolithic design, e.g. a paperclip. Compliant mechanisms used for frequency up-conversion consist of Low Frequency Oscillators (LFOs) and High Frequency Oscillators (HFOs) [30]. The device is able to multiply an input frequency by utilizing one of three couplings being impact coupling, stick coupling or transmission coupling [107]. In the first, kinetic energy is exchanged between two mechanical elements upon contact in a short amount of time. In the second, a temporal connection between the two elements makes the strain energy buildup in an elastic element, until a force or displacement threshold is reached, and the connection is broken. In the third, a permanent connection between the mechanical elements exists, coupling their motions into a single DOF. An example of a frequency up-converter using impact coupling is shown in Figure 9.1.

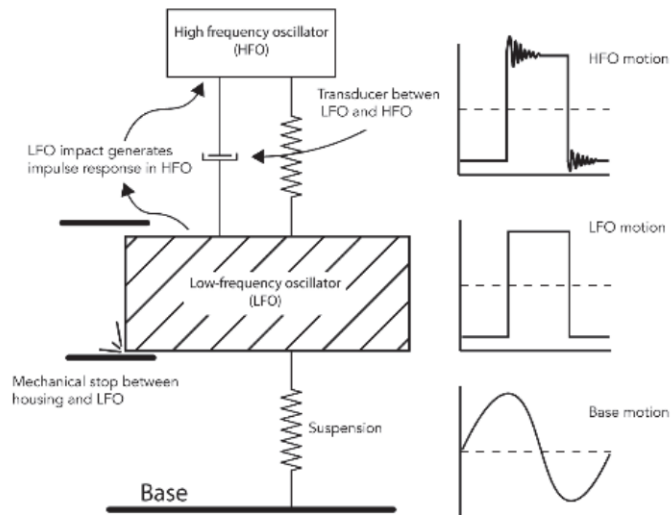


Figure 9.1: Example of a Frequency up-Converter using impact coupling to multiply the input frequency [30]. This type of up-converter is commonly used as a motion energy harvester in a wristwatch.

Although these concepts work well in small scale devices, application of these principles on a large scale is problematic because of the immense forces involved in the problem. Mechanical transmission systems like gears, clutches, belts, ropes, pulleys, and chains are all expected not to be rigid enough to withstand these forces. A promising alternative would be using hydraulic systems, as these are generally capable of transmitting greater forces than mechanical systems. The design of such a hydraulic system deserves a whole committed thesis of its own, but the boundary conditions of the proposed device will be listed here in short. The device should be able to at least withstand a force of 180 MN. These forces are of a dynamic nature which can be problematic if not accounted for in the design of the device. For instance, if a large snap load is experienced, the hydraulic system should be able to relieve the extra pressure build up. As was mentioned earlier, passive frequency multiplication is inherently tied to a decrease of amplitude, and this amplitude decrease should be kept as low as possible. This can be achieved by keeping damping at a minimum, so that little to no energy dissipates from the system. Since the device will be operating in an offshore environment, it should be corrosion resistant and include a minimum amount of moving parts to keep maintenance low. It should also be possible to exert a mean tensional force on the device without affecting the cyclic nature of the applied force.

It is interesting to look at the pile-soil response to forces that have a larger frequency but lower amplitude, to see what the effect of frequency multiplication would be (Figure 9.2).

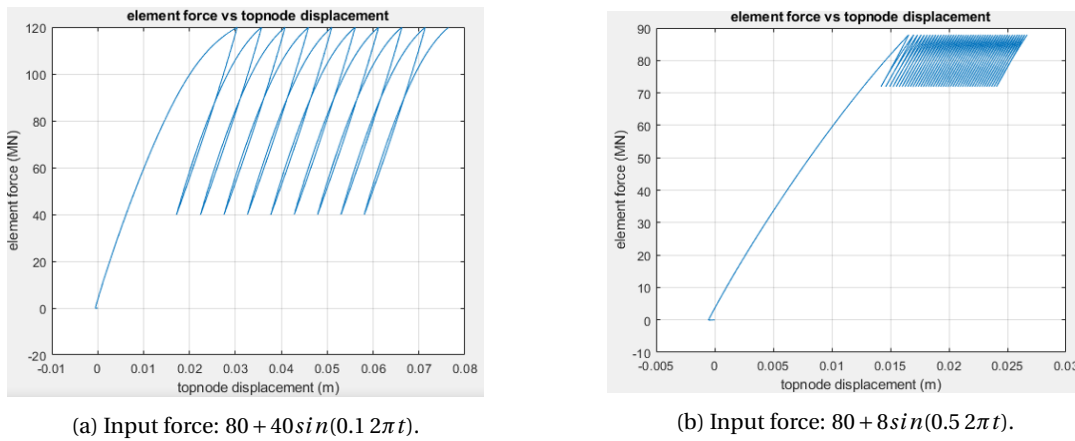


Figure 9.2: Force vs displacement graphs showing model response to frequency multiplication and amplitude reduction,

Figure 9.2 shows the response of the OpenSees model to such input forces, where the forcing frequency in Figure 9.2b is multiplied by a factor of 5 and the amplitude is divided by a factor of 5 with respect to Figure 9.2a. It is obvious from these graphs that the displacement resulting from the smaller amplitude input force is lower than the displacement resulting from the large amplitude force. This makes sense, as it was shown earlier that the OpenSees model is sensitive to the largest force in time that is applied to the model. In Figure 9.2b, the plastic spring in the t-z element does less work, and consequently a decrease in plastic strain accumulation is observed. However, because the amplitude has been decreased, the tensional part of the input force can be increased before the safe working limit of the crane is reached. A new scenario is considered, where the tensional part of the force is increased to 112 MN so that the maximum force in time is 120 MN (Figure 9.3).

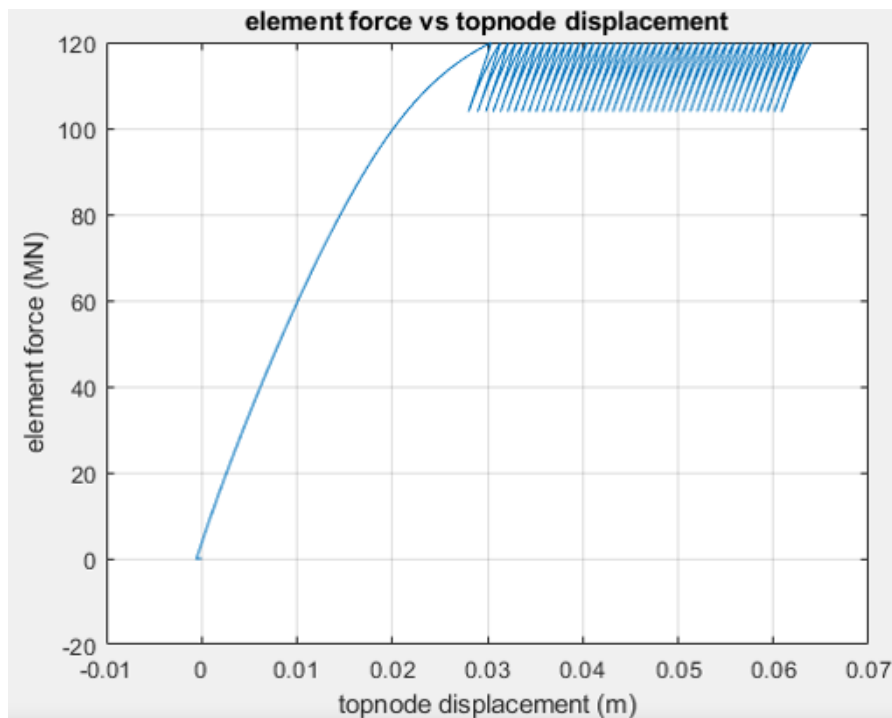


Figure 9.3: Force vs displacement graph as a result of a sinusoidal input force of the form: $112 + 8 \sin(0.5 2\pi t)$.

Figure 9.3 shows that the final node displacement is more or less equal to the final node displacement of Figure 9.2a, even though the frequency has been increased. An increase in frequency should, in theory, lead

to an increase node displacement, since the 0.5 Hz lies closer to the resonance frequency of the system. This behavior is not observed because it was also shown in Figure 7.6b that the resonance frequency increases, as the amplitude of the input frequency decreases. From this finding, the conclusion can be drawn that with every increase in frequency achieved with passive frequency multiplication and the accompanied reduction in amplitude, the resonance frequency of the system is increased and no increase in pile displacement can be achieved. Passive frequency multiplication is considered not to be feasible.

9.4.2. Active systems

To achieve frequency multiplication, the obvious solution is to look at active systems that are able to achieve high frequency oscillations on their own, using diesel, electric or hydraulic energy to do so. Vibratory hammers, such as the one used in decommissioning of the Lely wind farm monopiles by a Dieseko designed machine, excel at creating high frequency oscillations and are able to withstand a mean upward force during oscillations, in order to extract a monopile [90]. A schematical overview of such a vibratory hammer is shown in Figure 9.4.

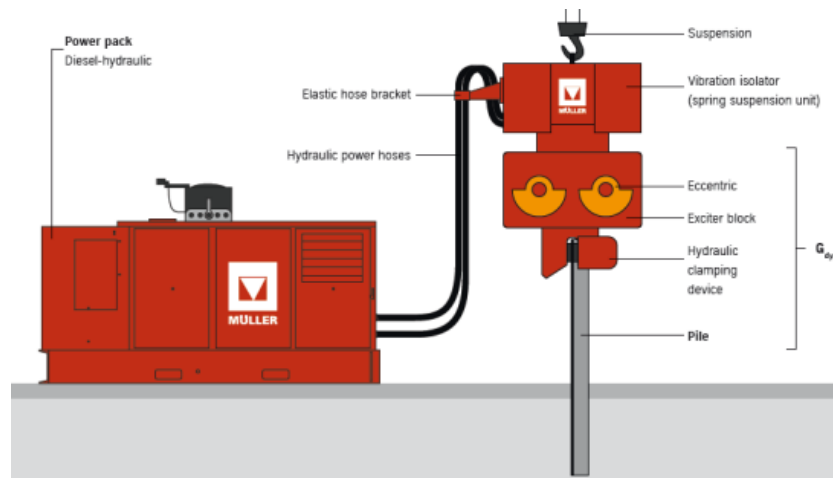


Figure 9.4: Overview of a vibratory hammer [31]. The eccentric masses create the harmonic force and are in this case driven by a hydraulic power unit.

A vibratory hammer relies on the idea of rotating eccentric masses, creating a vertical, harmonic force at every rotation Figure 9.5.

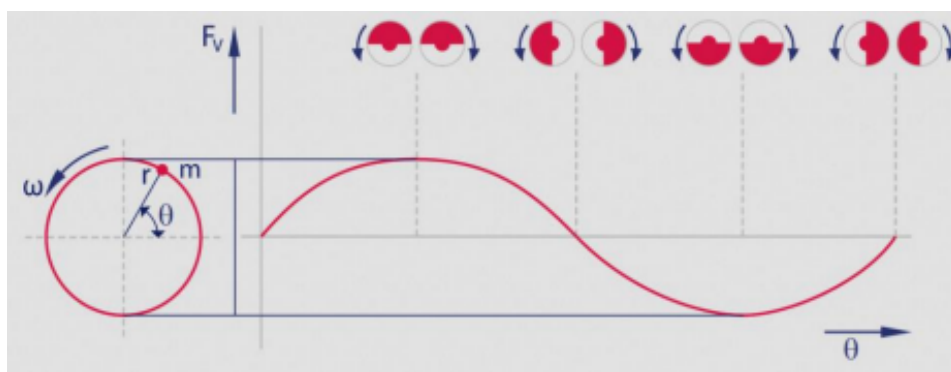


Figure 9.5: Representation of how rotation of an eccentric mass translates to a cyclic force [31].

The governing equations regarding force generation from eccentric mass rotation are shown in Equation 9.1 and Equation 9.2 [108].

$$m_r = g_r d_r \quad (9.1)$$

Where: m_r = eccentric moment (kgm)
 g_r = eccentric mass (kg)
 d_r = distance between point of gravity of eccentric mass and rotation point (m)

$$F_c = m_r(2\pi f)^2 \quad (9.2)$$

Where: F_c = centrifugal force (N)
 m_r = eccentric moment (kgm)
 f = rotational frequency (Hz)

Dieseko is currently developing a vibratory hammer with an eccentric moment of 2000 kgm that is able to operate at 1400 rpm [90]. Using the equations listed above, this results in a harmonic force with an amplitude of 43.0 MN, or using the industry standard measuring unit, 4.400 tons. As was shown in chapter 4, this force is not enough to pull out a monopile on its own, but it does not have to be. The frequency at which the vibrator oscillates is high enough to ensure that liquefaction of the soil occurs. The pile is vibrated at this frequency until it is observed to move downward. Then a separate crane lifts the pile and the vibratory hammer out of the soil while the hammer keeps vibrating. A reduction of soil resistance of 90% has been observed using this method [90]. As the frequency is increased during the start-up procedure, care should be taken when crossing the natural frequency of the crane system, as this can seriously harm the components involved [90].

Such an active way of achieving a high frequency is of course not the most desirable, as it completely disregards the idea of this thesis to use vessel motion to reduce soil resistance. A passive way to achieve frequency multiplication is more desired. On top of that, it has been observed during installation of monopiles of the Kaskasi wind farm, that not a single pile achieved its designed penetration depth by vibratory pile driving alone [41].

A

Offshore wind farm market analysis of MP and TP dimensions

The following table is the result of extensive market research into offshore wind farms in Europe. A decision was made to look into European wind farms only, since the Chinese offshore wind market was in the middle of its great expansion of 2021 and most data was not logged at the time. If multiple dimensions within a wind farm exist, the largest dimension is selected.

Table A.1: European offshore wind farm monopile dimensions and parameters for the five largest countries in the offshore wind sector in Europe. Farm capacity less than 50 MW is not considered. Blue = UK, Green = Germany, Orange = Netherlands, Red = Belgium, Yellow = Denmark. BF = Bolted Flange.

| Wind farm | Capacity (MW) | Year | Water depth (m) | Length (m) | Penetration depth (m) | Weight (Metric tons) | Bottom diameter (m) | Top diameter (m) | TP connection |
|------------------------|---------------------|------|-----------------|------------|-----------------------|----------------------|---------------------|------------------|---------------|
| Horns Rev I | 80 x 2.0 | 2002 | 20 | 60 | 27,5 | 138,5 | 4,2 | 4,2 | Grout |
| North Hoyle | 30 x 2.0 | 2003 | 12 | 53,3 | 41,3 | 275 | 4 | 4 | Grout |
| Scroby Sands | 30 x 2.0 | 2004 | 8 | 45,5 | 30 | 200 | 4,2 | 4,2 | Integrated |
| Kentish flats | 15 x 3.3 & 30 x 3.0 | 2005 | 5 | 38 | 33 | 247 | 4,5 | 4,3 | Grout |
| Princes Amalia | 36 x 3.0 | 2006 | 24 | 54 | 30 | 320 | 4 | 4 | Grout |
| Egmond aan Zee | 60 x 2.0 | 2006 | 18 | 60 | 30 | 250 | 4,6 | 4,6 | Grout |
| Barrow | 90 x 3.0 | 2006 | 23 | 61,2 | 38,2 | 452 | 4,8 | 4,8 | |
| Burbo bank | 25 x 3.6 | 2007 | 6 | 37 | 31 | 212 | 5 | 5 | Grout |
| Horns Rev II | 91 x 2.3 | 2009 | 17 | 40 | 23 | 210 | 3,9 | 3,9 | Grout |
| Lynn and Inner Dowsing | 54 x 3.6 | 2009 | 11 | 36 | 25 | 225 | 4,7 | 4,7 | Grout |
| Rhyl flats | 25 x 3.6 | 2009 | 12 | 40 | 28 | 235 | 4,7 | 4,7 | Grout |
| Belwind | 50 x 3.3 | 2010 | 36 | 65 | 29 | 550 | 5 | 4 | Grout |
| GF Sands 1 & 2 | 48 x 3.6 | 2010 | 15 | 50 | 37 | 423 | ? | 4,7 | Grout |
| Thanet | 100 x 3.0 | 2010 | 25 | 60 | 35 | 371 | 5,1 | 4,9 | |
| Baltic 1 | 21 x 2.3 | 2011 | 19 | 37 | 18 | 215 | 4,3 | 4,3 | Grout |
| Sheringham Shoal | 88 x 3.6 | 2012 | 24 | 50 | 26 | 500 | 5,7 | 4,7 | Grout |
| Greater Gabbard | 140 x 3.6 | 2012 | 32 | 67,7 | 30 | 676 | 6,3 | 5,1 | Grout |
| Lincs | 75 x 3.6 | 2013 | 15 | 49 | 30 | 340 | 5,2 | 4,7 | Grout |
| Teesside | 27 x 2.3 | 2013 | 15 | 51 | 36 | 352 | 4,6 | 3,9 | |
| Anholt | 111 x 3.6 | 2013 | 19 | 55 | 36 | 630 | 5,35 | 4,7 | Grout |
| London Array | 175 x 3.6 | 2013 | 25 | 68 | 43 | 650 | 5,7 | 4,7 | Grout |
| West of Duddon Sands | 108 x 3.6 | 2014 | 24 | 59 | 35 | 516 | 6 | 5,6 | Grout |
| Meerwind Sud/Ost | 80 x 3.6 | 2014 | 26 | 64 | 38 | 680 | 5,5 | 5,5 | Grout |

Table A.2: Table continued, thick line below Humber Gateway shows the boundary between the first and second generation of monopiles as it is assumed in this thesis.

| Wind farm | Capacity (MW) | Year | Water depth (m) | Length (m) | Penetration depth (m) | Weight (Metric tons) | Bottom diameter (m) | Top diameter (m) | TP connection |
|--------------------------|----------------------|------|-----------------|------------|-----------------------|----------------------|---------------------|------------------|---------------|
| Northwind | 72 x 3.0 | 2014 | 28 | 66 | 38 | 420 | 5,2 | 4,2 | Grout |
| Riffgat | 30 x 3.6 | 2014 | 24 | 70 | 40 | 720 | 6,3 | 4,7 | Grout |
| Luchterduinen (=hk zuid) | 150 x 4.0 | 2015 | 36 | 65 | 29 | 560 | 5 | 4,5 | Integrated |
| EnBW Baltic 2 | 80 x 3.6 | 2015 | 44 | 73,5 | 29,5 | 832 | 6,5 | 5 | |
| Borkum Riffgrund I | 78 x 4.0 | 2015 | 29 | 66 | 30 | 700 | 5,9 | 5,9 | |
| DanTysk | 80 x 3.6 | 2015 | 31 | 63 | 32 | 575 | 6 | 6 | Grout SK |
| Gwynt y mor | 160 x 3.6 | 2015 | 33 | 70 | 37 | 687,5 | 6,5 | 4,6 | Grout |
| Amrumbank West | 80 x 3.6 | 2015 | 25 | 60 | 30 | 700 | 6 | 6 | BF |
| Humber Gateway | 73 x 3.0 | 2015 | 15 | 60 | 45 | 650 | 4,9 | 4,5 | BF |
| Gemini | 43 x 3.0 | 2015 | 24 | 73 | 49 | 800 | 7 | 5,5 | Grout |
| Gode Wind 1&2 | 97 x 6.0 | 2016 | 33 | 67 | 34 | 939 | 7,5 | 5,7 | Grout |
| Galloper | 58 x 6.0 | 2016 | 36 | 85 | 49 | 1237 | 7,5 | 6,3 | |
| Dudgeon | 67 x 6.0 | 2017 | 25 | 44,5 | 19,5 | 840 | 7 | 6,3 | Grout |
| Sandbank | 72 x 4.0 | 2017 | 33 | 70 | 37 | 1083 | 6,8 | 5,5 | |
| Nordsee One | 54 x 6.2 | 2017 | 29 | 70 | 41 | 900 | ? | 5,5 | BF |
| Veja Mate | 67 x 6.0 | 2017 | 41 | 84,4 | 43,4 | 1300 | 8,7 | 6,5 | BF |
| Nobelwind | 50 x 3.3 | 2017 | 30 | 77 | 47 | 800 | 6,8 | 4,5 | BF |
| Walney extension | 47 x 7.0 & 40 x 8.25 | 2018 | 37 | 72,5 | 35,5 | 970 | 8,4 | 6,2 | |
| Arkona | 60 x 6.0 | 2018 | 37 | 81 | 40 | 1200 | 7,75 | 7 | BF |
| Rampion | 116 x 3.45 | 2018 | 41 | 60 - 85 | 44 | 647 | 6,5 | 5,75 | BF |
| Rentel | 44 x 7.0 | 2018 | 36 | 83 | 47 | 1250 | 8 | 5,6 | Grout |
| Horns Rev III | 49 x 8.3 | 2019 | 20 | 50 | 30 | 610 | 6,5 | 6,5 | |
| Albatros | 16 x 7.0 | 2019 | 40 | 71 | 31 | 1081 | 8 | 6 | |
| Hohe See | 71 x 7.0 | 2019 | 40 | 71,4 | 31,4 | 1070 | 8 | 6 | |
| Mercur | 66 x 6.0 | 2019 | 33 | 72,6 | 35,4 | 970 | 7,8 | 6 | BF |
| Deutsche Bucht | 33 x 8.2 | 2019 | 40 | 78 | 38 | 1100 | 8 | 6,5 | |
| Borkum Riffgrund 2 | 56 x 8.0 | 2019 | 30 | ? | ? | 900 | 8 | 6,5 | BF |
| Hornsea One | 174 x 7.0 | 2020 | 30 | 65 | 35 | 800 | 8,1 | 6 | BF |
| Borssele 1&2 | 94 x 8.0 | 2020 | 36 | 76 | 40 | 1188 | 8,3 | 6,5 | |
| Northwester 2 | 23 x 9.5 | 2020 | 40 | 82 | 42 | 1000 | 8 | 6,5 | |
| Seamade | 58 x 8.4 | 2020 | 38 | 80,4 | 42,4 | 1040 | 8 | 6,3 | BF |
| Triton Knoll | 90 x 9.5 | 2021 | 18 | 50,3 | 32,3 | 537 | 6,9 | 6,5 | BF |
| Kriegers Flak | 72 x 8.4 | 2021 | 30 | 65 | 35 | 810 | 6 | 6 | BF |
| Borssele 3&4 | 77 x 9.5 | 2021 | 38 | 85 | 47 | 1280 | 7,4 | 6,5 | Integrated |
| Hornsea Two | 165 x 8.4 | 2022 | 40 | 77,2 | 37,2 | 1285 | 9,5 | 6,5 | |
| Dogger bank A & B | 190 x 13 | 2023 | 35 | 50 | 15 | 1200 | 8,6 | 8,3 | BF |

In this table, water depth was taken as Lowest Astronomical Tide (LAT). Finding data on embedded length proved to be difficult as press releases almost never present this type of technical information and owners are not keen on sharing it. When data was unavailable the assumption was made that the embedded length is equal to the pile length minus water depth and 5% pile length for clearance. This complies with findings by Liu [42], who found that because of increasing diameters, embedded length has stabilised to a value between 30 and 40 meters. In his research, Liu found that the old rule of thumb prescribing embedded pile lengths of 5 times the diameter is obsolete and the trend moves toward 3 to 4 times the diameter [5].

B

Monopile to transition piece connections

This appendix discusses the different types of connections between the transition pieces and monopiles that are commonly used in industry today. It will list pros and cons of these connections and explain why industry has shifted from one to the other. Figure B.1 shows combinations of three of the most used concepts, being a grouted, bolted and slip joint connection. Recently, transition pieces integrated in the monopile itself are increasing in popularity as they reduce the number of offshore lifts during installation, reducing time spent offshore and overall costs while increasing HSEQ conditions.

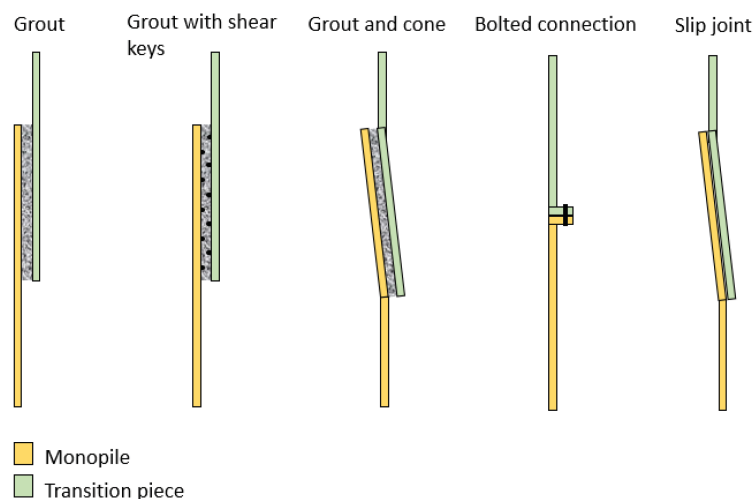


Figure B.1: Different types of transition piece to monopile connection [32].

B.1. Grout connections

Figure B.2 shows a typical grouted monopile to transition piece connection where the TP is placed over the MP in order for it to facilitate necessary operational requirements such as a boat landing, and the external and internal platforms [33, 41]. Grouted connections have been used in the O&G sector extensively with success which is one of the reasons that the grouted connection was initially used in the offshore wind industry.

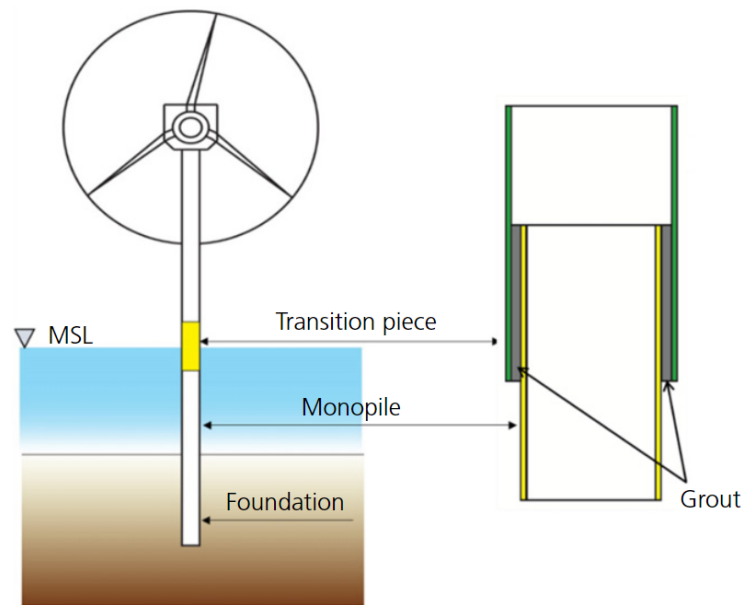


Figure B.2: Typical grouted MP-TP connection [33].

Grout is a composite material made up of water, cement and sand. It can be compared to concrete as it is made of the same materials, but the quantities are different, which results in grout being less viscous than concrete, increasing workability [39]. Grout is used in the offshore industry because it is flexible, can be mixed on site and it develops great strength properties over a short period of time. As a rule of thumb, after 7 days of grouting the grout has achieved 75% of its compressive strength. Regulations demand that after 28 days the compressive strength is measured axially as it is believed that the grout has achieved most of its strength after that time [39]. When these checks are complete and sufficient, the installation of the tower, RNA and secondary steel on the TP can begin.

However, over the last decade grouted connections in WTGs have failed several times across numerous wind farms. For example in Kentish Flats and Horns Rev I, settlement of the TP and abrasive wear due to sliding of the contact surfaces was observed [33]. Another example is that of the Dutch Offshore Wind Egmond aan Zee (OWEZ) wind farm. This, to the authors knowledge, is the only wind farm where the transition piece had a smaller diameter than the monopile and thus when vertical settlement of the transition piece occurred, the whole inside of the monopile had to be filled with concrete. As one can imagine, especially this last example will result in complications during the inevitable decommissioning process [41, 109]. The problem with grout connections up to some point got so severe that up to 2011, 600 of the 948 installed turbines with a grout connection have seen grout failure [110]. There has been a lot of research into why the grout connection does not behave the way it is supposed to, or the way it does in the O&G sector and Tsiavos et al. [33] sum them up nicely. They conducted a thorough review on how the environmental loads on an offshore structure are determined and afterwards, what numerical methods are used to model the structural behavior of grout. The main conclusion of their research is that the highly brittle grout behaves non-linearly which makes it very hard to model it properly in FE analyses [33]. On top of that the modelling of the grout-steel interface between the grout and the MP or TP is also hard to adequately represent in models and faulty assumptions and linearizations in this process is where most models wrongly predict grout behavior, resulting in failure. Another noteworthy conclusion from their research is that there is little grout data available from the offshore wind industry, indicating that most data and modelling indeed comes from the O&G sector.

After these flaws became apparent, design standards became more stringent on grout use as it was found out that design standards indeed overestimated the bearing capacity of grout connections between two smooth cylindrical walls by a significant margin [111]. Codes like DNV changed in 2014 to mandatory use of conical monopile and transition piece sections in the part where grout is used, as seen in the middle of Figure B.1.

This way, it was thought that the vertical settlement of the TP would be halted by the increasing diameter of the monopile. If still a tubular connection is used, use of shear keys is mandatory, but the choice between conical and tubular sections was left up to designers [34]. The three discussed connections in this section are illustrated by the first three illustrations from the left in Figure B.1.

Shear keys

Shear keys were introduced in design standards as they had been used in the O&G sector successfully for a long time. Usage of shear keys as mandated by the DNV [34] is shown in Figure B.3.

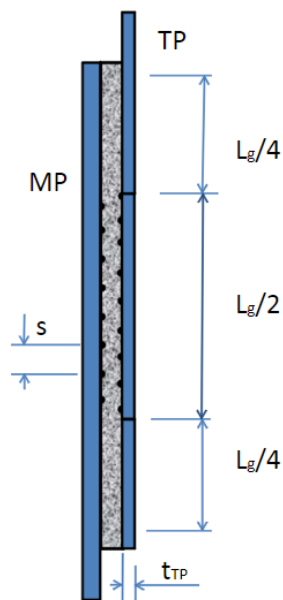


Figure B.3: Shear keys in a grouted TP-MP connection [34].

Shear keys are circumferential weld beads, welded onto the surface of the MP and TP with the goal of increasing the surface area and sliding resistance between the two wall sections. This way, when the transition piece starts to sag, the shear keys prevent the downward motion, or using the words of the DNV: "using shear keys, axial capacity of the connection can be counted on in design, in contrast to what holds for tubular grouted connections without shear keys" [34]. Designers remained sceptical to keep using grouted connections because of the large differences in dimensions between the O&G and offshore wind sector [110].

Forces on grouted TP when pulling on it

As was demonstrated earlier in this report, grouted connections were used in early to recent stages of offshore wind industry development. When only grout is used as a connection between the transition piece and the monopile, it is highly unlikely that both can be decommissioned in a single lift by exerting a tensile force on the transition piece [41]. Grout has great performance properties in compression, with a maximum compressive strength of 90 N/mm^2 but lacks strength in tension, with a maximum tensile stress of 10.4 N/mm^2 [112]. Simple calculations already show that the normal stress in a grouted connection without shear keys can quickly rise over 80 MPa Equation B.1 which greatly exceeds the maximum tensile stress.

$$\sigma = \frac{F}{A} = \frac{200e6}{0.25\pi(D_o^2 - D_i^2)} = \frac{200e6}{0.25\pi(6.5^2 - 6.34^2)} = 124.0 \text{ MPa} \quad (\text{B.1})$$

Another note must be made that in practice, hardly any adhesion between the grout and monopile surface is observed [113]. Rather than through adhesion, the main method of load transfer between the pile and grout is "through shear friction mobilised by the normal stress induced through interlocking of surface imperfections and compression of the grout" [113]. Considering adhesion between the pile and grout is poor, it is highly unlikely that grout will be able to transmit the immense forces involved in complete removal, and will most likely fail upon trying.

It is obvious from the previous sections that grouted connections, be it with or without conical sections and shear keys, are no longer the best design practice for monopile to transition piece connections and other methods, like the bolted connection, are more desirable.

B.2. Bolted connection

After millions were spent on preventing transition pieces from sagging, designers looked onward to more promising connections like the bolted flange connection [110]. In a bolted flange connection, on the top part of the monopile a flange is present which is rigidly connected to the flange on the bottom of the transition piece, usually using M72 bolts. This is illustrated in Figure B.1 in the fourth illustration from the left. The bolts in a bolted flange connection often are covered with grout to ensure water tightness [41], making maintenance of the bolts difficult. The maintenance time and costs are also higher than for the traditional grout connection as well as other, more inventive connections [72]. Installation can be done more quickly than in grouted connections but is complicated by the fact that impact hammering might damage the flange on top of the monopile [111] and designers have to account for this in their FLS calculations. On top of that, turbine collapse due to bolt failure has also been observed in Lemnhult, Sweden [72]. Bolt failure due to fatigue is often encountered from a loss of pre-tension, as well as hydrogen embrittlement, which is encountered more often offshore due to the very high forces and presence of salt water [41]. Another downside of a bolted connection is that placing of the transition piece can no longer correct any misalignment of the monopile that has occurred during piling, which could be done by grouting the transition piece at a slight angle, allowing for 0.5° corrections [111]. Using M72 bolts is also a limiting factor for scaling up this connection method. As turbine sizes get bigger and bigger and environmental loads more severe, the bolts connecting TP to MP, and TP to turbine tower increased as well, up to the very large size of M72 bolts. Especially from a HSEQ perspective this causes problems, as M72 bolts are already at their maximum permitted weight to be lifted by personnel as they weigh 18 kg, and the equipment necessary to tension the bolts already exceeds HSEQ lifting limits necessitating the use of extra lifting equipment inside the tower of the turbine during installation [36]. In addition to HSEQ lifting limits, the larger M80 bolts are not yet included in design standards like DNV 2016, [86]. Dogger bank A, B & C are the only wind farms that will experiment and implement these M80 bolts [41], turbine installation is expected to commence in 2023 at Dogger bank A.

Despite the obvious flaws, the bolted flange connection is certainly an upgrade from the grouted connection, resulting in the fact that almost all newly designed offshore wind turbines use it. There are more, innovative connection methods that are used occasionally or are still in the design phase, but the main connection type nowadays remains a bolted flange connection.

B.3. Slip-joint

A slip joint connection is a connection where, normally, no grout or bolts are used, but the connection is based on the friction created by placing two conical sections on top of each other, depicted in the final illustration of Figure B.1. Think of the connection as placing two upside down glasses on top of each other. The method was firstly installed at full scale in 2020 by Van Oord at the Borssele V wind farm site, after the GROW consortium completed their Slip Joint Offshore Research (SJOR) program [114]. The weight of the transition piece ensures the stability and firmness of the connection. Without the use of grout or bolts, the transition piece is easily slid over the monopile, reducing installation time and time spent offshore significantly. A great benefit of the slip joint, unlike traditional methods, is that it allows for a submerged connection, which makes it possible to balance the weight distribution between the MP and TP [114]. The balancing of this ratio enables manufacturers and designers to increase foundation and transition piece sizes so that monopiles can be used in ever deeper waters. Another benefit of the slip-joint is that it can easily be implemented in a TP-less design for a monopile [72], which will be discussed in the next section about integrated TPs.

A cutting-edge design is that of the double slip joint by the DSJ-consortium of KCI engineers, Van Oord and SIF Group [35]. Their design, shown in Figure B.4, consists of two cylindrical rings that, in an ideal case, make full contact along the 360 degrees of the MP-TP combination. This reduces the contact area from the entire conical section to just these two rings. It must be noted that this reduction in contact area makes the design susceptible to very high peak loads and stresses which might exceed maximum design levels.



Figure B.4: Double slip joint [35].

The consortium claims the following benefits regarding the concept [35]:

- Simple, robust and stable connection.
- 30% lower cost of installation.
- Lower manufacturing costs, especially for future, larger turbines.
- Installation is faster and safer.
- Increases flexibility in the installation fleet for future XXL turbines.

The company is looking to implement the technology at full scale at the moment. But whether the double slip-joint is a success remains to be seen.

B.4. Integrated TP

Over the years, some designers opted for an integrated design of the monopile and the transition piece. The top part of the monopile in such a design is painted yellow and, after installation, all secondary steel, such as boat landings and platforms, are installed since they are not able to withstand the large accelerations and stresses from piling. Downside of such a concept is that once again hammering on a flange is applied and care must be taken not to exceed the FLS of the monopile and the Ultimate Limit State (ULS) of the flange. The benefit of an integrated TP is that it saves not only installation time but also reduces O&M costs as it reduces the number of bolt/grout connections from two to one. Examples of wind farms that implemented an integrated TP are Scroby Sands, which implemented the method as early as 2004 and showed no signs of negative effects since, Luchterduinen, and the recently installed Hollandse Kust Zuid (HKZ) which was recently covered in the news because of a collision with a freely drifting vessel.

In case of Luchterduinen, installation time of monopiles was considerably low with just 12 to 14 hours installation time at the end of the project; at Scroby Sands it was 18 hours per pile, showing a steep learning curve as well [115]. This reduction in installation time includes arriving at location, jacking up the vessel, hammering, measuring, jack-down and sailing to the next location. A downside and time-consuming part of the integrated TP is that secondary steel has to be installed after installation of the pile is finished. Integrated TP design also comes with other downsides, such as the aforementioned inability to fix vertical alignment errors of the monopile by placement of the TP resulting in a very low margin for error during installation. On top of that, if something goes wrong after installation, like a vessel collision with a monopile such as the event at HKZ, matters become more complicated, seeing as replacing only the TP is not an option.

Integrated TPs carry another inextricably linked downside with them, being that the size and weight of the foundation rises significantly. Especially when looking at the trend toward XXL monopiles, foundations will become enormous and the vessels and cranes used during installation consequently, will have to become enormous as well. This puts a lot of stress on contractors to update their fleet accordingly and could be a reason to only use integrated TPs in WTGs of smaller dimensions.

B.5. C1 wedge connection

Another innovative design showing promising results is that of the C1 wedge connection. The inventors were motivated to find a new way of connection between the MP and TP by the limiting factors of the bolted L-flange connection, called simply the bolted connection earlier in this report. In the C1 wedge connection, the monopile and transition piece are connected using C1 Wedges, shown in Figure B.5. For this design to work, the bottom part of the transition piece must have a fork-like profile, while the monopile its top part can retain its original cylindrical shape, both of these criteria can be met by manufacturers existing production facilities [36]. The design has already been approved by DNV-GL.

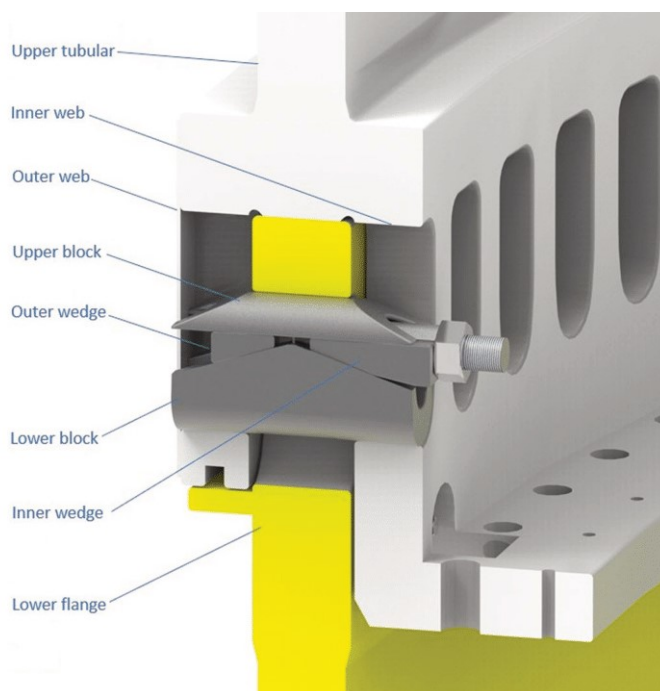


Figure B.5: C1 Wedge connection between MP and TP [36].

The method allows for a more safe installation, requiring less personnel and less use of heavy equipment during installation. The quality control of the bearing capacity can be done by visual inspection and it is claimed to be maintenance free. This last claim is based mainly on the fact that the usual failure method of traditional bolts, being preload loss due to settlement in the thread, is not a problem for the C1 Wedge because, firstly, the bolt is tightened up to 70% of the yield stress whereas traditional L-bolted flanges are pretensioned up to 90%. Secondly, the C1 wedge needs four complete rotations to obtain preload in contrast to the one tenth of a rotation for traditional L-bolted flanges, which makes any errors in tightening of much smaller significance and thirdly, a significant loss of preload in the bolt of the C1 does not result in an equal loss of preload of the overall mechanism [36]. Full scale tests have been conducted at the TU Delft on 4.5 meter diameter piles and tests confirmed the claims made by C1 Connections, the manufacturing company [36].

A downside of the method is that, at the moment, the C1 wedge can not be used when piles are installed using impact hammering. In that case the necessary shape of the monopile is unlikely to support the impact of the hammer during piling [36].

C

Monopile condition at EOL

C.1. What does the structural integrity of a monopile look like after design life is reached?

To accurately describe the processes involved in monopile corrosion, additional terminology is introduced. While different designs exist because of different MP-TP connections, in all foundation types the following structures and components are present.

- Internal air-tight and work platforms
- External platform
- Boat landing
- Ladders
- Anodes
- Scour protection
- Grout skirts
- Internal or J-tube cable entry

Four different zones are distinguished regarding corrosion, Figure C.1. The area most affected by corrosion is the splash zone, where water and air are both in regular contact with the surface. In this region, unprotected external steel surfaces experience a minimum wall thickness reduction of 0.30 mm/year, which reduces to 0.10 mm/yr for internal surfaces [37]. Because of these large reductions in wall thickness, protective coatings like Interzone 954 [116] on external surfaces are mandatory in the splash zone. Combined with coating, Cathodic Protection (CP) can be used, where sacrificial anodes corrode away, rather than the primary steel. Cathodic protection is mandatory for all external surfaces 1 meter below the Mean Water Line (MWL). According to DNV it can safely be assumed that no wall thickness reduction occurs if coating is undamaged and sufficient CP is applied, which means that external surfaces of monopiles will remain unaffected after their design life. The inside surfaces of a MP and TP are usually not coated, but CP is mandatory by DNV standards [37]. A problem here is that CP does not work for surfaces that are not completely submerged, and if tidal variation is present inside the MP, this can induce corrosion.

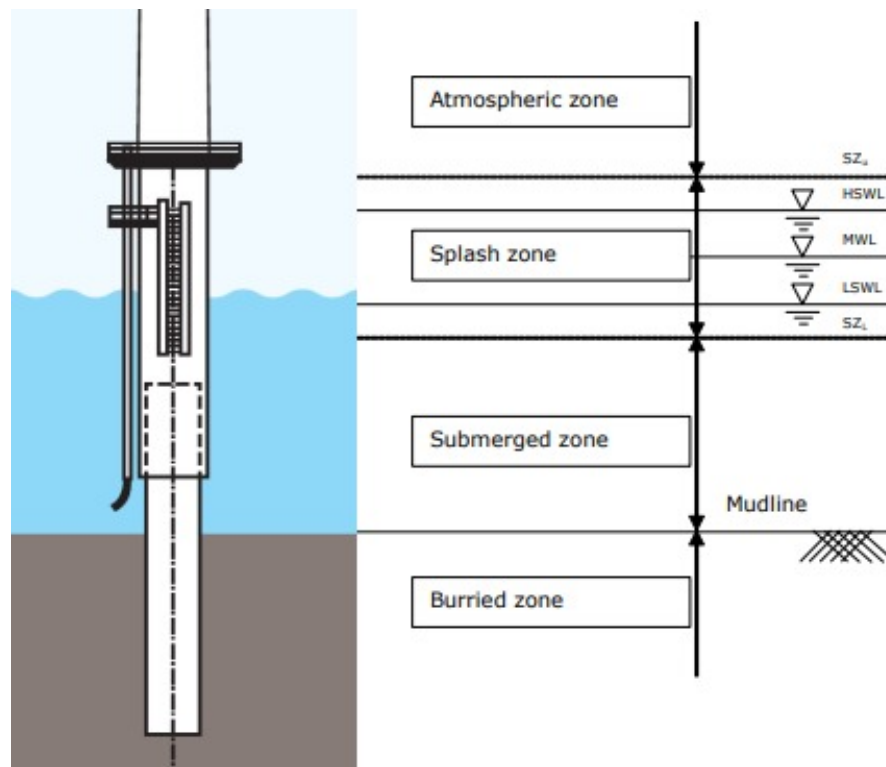


Figure C.1: Important zones of MP and TP regarding corrosion [37].

In the atmospheric zone, both external and internal surfaces must be protected by coating [37]. However, in transition pieces, an air tight platform is installed, making sure that no salt water and oxygen is able to enter the inside of the tower, reducing corrosion effects and the need for internal coating. Literature suggests that corrosion rates on internal surfaces can be higher than expected. Hilbert et al. [117] found uniform corrosion rates of 0.1-0.15 mm/yr, and 0.4 mm/yr locally. This growth rate is reduced in time as the corrosion layer thickness increases. In an ideal case, the inside of the monopile is sealed off and air only enters during maintenance, stopping the aerobic corrosion process quickly as air corrodes away (anaerobic corrosion still occurs but this is less harmful [116]). Reality however, shows that there are often leakages near the J-tube entry or power cable entry subsea, causing fresh seawater to enter the pile. During inspection of a five to ten years old wind farm consisting of 36 turbines only 3 foundations were completely free of oxygen and 25 showed oxygen levels above 15% [117]. On top of aerobic corrosion there is also microbial activity in the water, producing H_2S , sulphur and iron, affecting corrosion. If the foundation is water tight and no fresh water enters through the bottom, this microbial activity should die out quickly as the result of absence of nutrients [117]. Below the waterline, corrosion will mostly be in the form of differential aeration between the upper and lower water layers [117], which means that an anode and a cathode form on the MP due to varying oxygen concentrations along its surface.

Inlet of fresh seawater through a J-tube has a significant effect on corrosion rates: increasing uniform corrosion (throughout entire MP) by 0.1-0.15 mm/yr and 0.2-0.3 mm/yr locally, differential aeration close to the seabed by 0.2 mm/yr, and microbiologically influenced corrosion (MIC) in the upper parts of the mud zone by 0.1-0.25 mm/yr depending on oxygen potential. Khodabux et al. even found local corrosion rates at the seabed-water interface of 0.83 mm/yr, which is much higher than design standards prescribe [116]. Their value however, is almost four times as high as was the case in the 43 reference field experiments and also four times as high as the DNV standard prescribes and it might be explained by a larger than normal concentration of nitrogen at the seabed [116].

Expert interviews conducted at Allseas revealed that in practice, if the coating is intact and CP proved sufficient at EOL, no wall thickness reduction is assumed. If damages are observed, inspection and measurements are carried out to quantify reduction. In case of the Ninian Jacket a reduction of 3 millimeters was sufficient. Because of the variability of the problem and the case-by-case approach, no assumption regarding outside

wall thickness reduction will be made but it shall be implemented in a model as a variable, allowing for variation between load cases. For inside wall thickness reduction the same conclusion is applicable but a different parameter

D

AQWA data

AQWA data used for hydrostatic stiffness, Figure D.1.

| | X | Y | Z |
|-------------------|---|---|---|
| CENTRE OF GRAVITY | | | |
| INERTIA MATRIX | | | |

Figure D.1: Inertia matrix of PS at a draft of 17 meters.

AQWA data used for determining natural frequency in heave and pitch, Figure D.2.

| FREQUENCY NUMBER | FREQUENCY (RAD/S) | UNDAMPED SURGE(X) | NATURAL SWAY(Y) | FREQUENCIES(RADIANS/SECOND) HEAVE(Z) | ROLL(RX) | PITCH(RY) | YAW(RZ) |
|------------------|-------------------|-------------------|-----------------|--------------------------------------|----------|-----------|---------|
|------------------|-------------------|-------------------|-----------------|--------------------------------------|----------|-----------|---------|

Figure D.2: Frequencies as input in AQWA in iterative process, resulting outputs are response frequencies. Coinciding frequencies marked red and taken as natural frequency in that DOF.

AQWA data used for determining critical damping in heave and pitch, Figure D.3. Ansys data used to determine the added mass and damping at the forcing frequencies is shown in Figure D.4 and Figure D.5.

| FREQUENCY NUMBER | FREQUENCY (RAD/S) | APPROXIMATE SURGE(X) | PERCENTAGE SWAY(Y) | CRITICAL DAMPING HEAVE(Z) | ROLL(RX) | PITCH(RY) | YAW(RZ) |
|------------------|-------------------|----------------------|--------------------|---------------------------|----------|-----------|---------|
|------------------|-------------------|----------------------|--------------------|---------------------------|----------|-----------|---------|

Figure D.3: Frequencies as input in AQWA in iterative process with corresponding critical damping values in percentages. At the natural frequency, critical damping is selected.

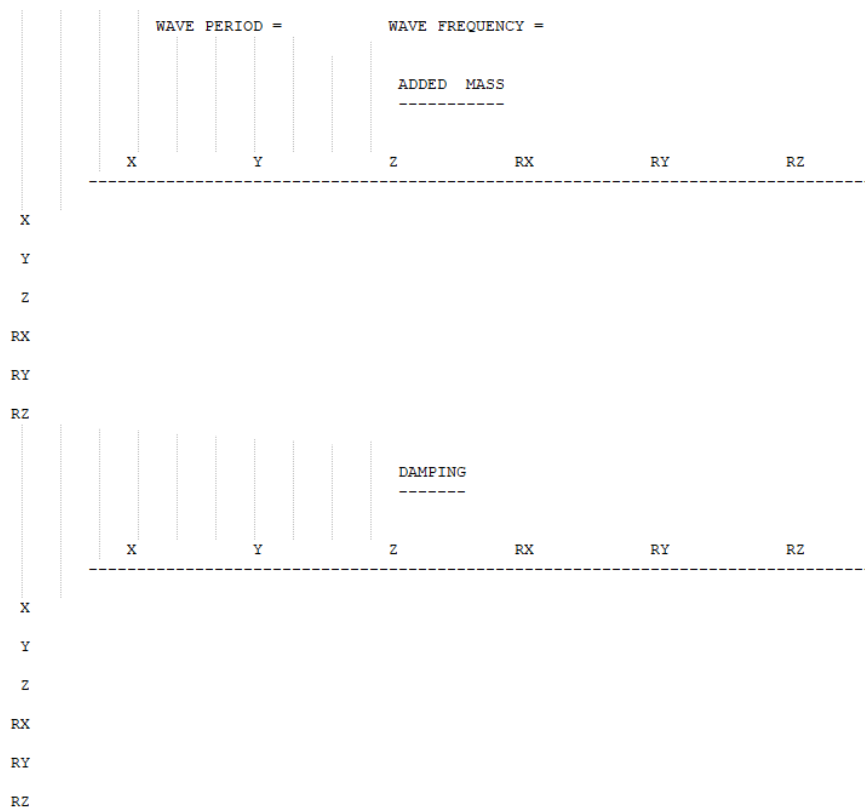


Figure D.4: ANSYS data used to determine the added mass and damping in heave.

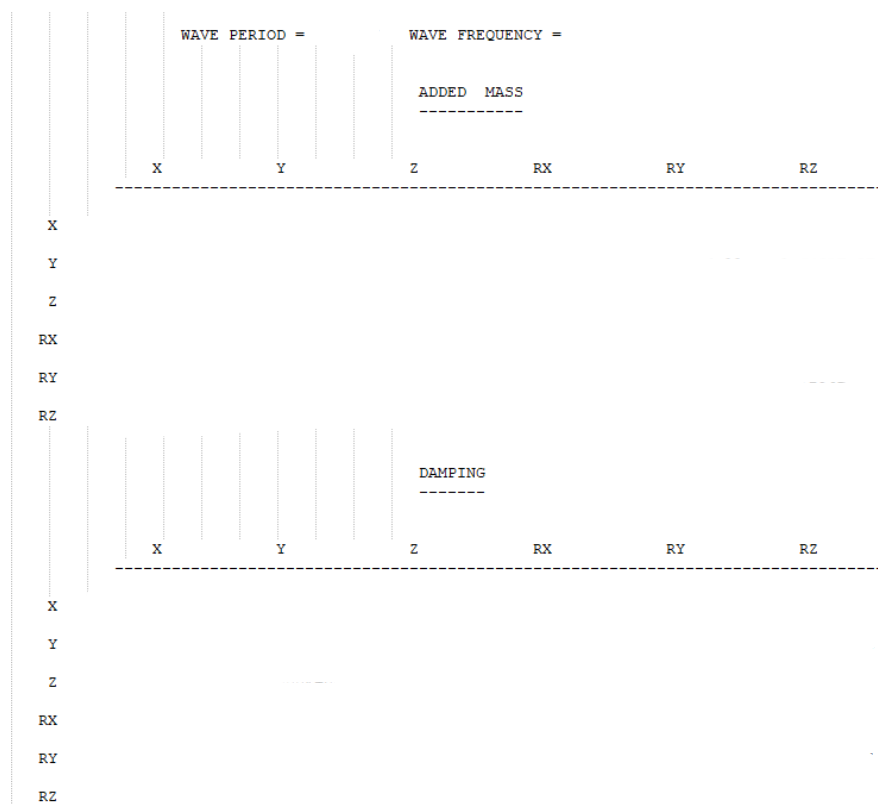


Figure D.5: ANSYS data used to determine the added mass and damping in pitch.

E

Vessel model validation and sensitivity analysis

E.1. RAOs

In order to get a better feel for the response of the PS to waves of different frequencies, coming from different directions, it is useful to look at its Response Amplitude Operators (RAOs). These graphs show the energy spectrum of the vessel response at different wave frequencies.

The RAOs in the CoG are known and provided by Allseas, these need to be translated to the beam tip. Combining the three individual translational matrices to form 1 complete translation matrix in Equation E.1, the RAOs can be translated to the beam tip, which is the point of interest.

$$\begin{bmatrix} 1 & 0 & 0 \\ 0 & \cos(\phi) & -\sin(\phi) \\ 0 & \sin(\phi) & \cos(\phi) \end{bmatrix} * \begin{bmatrix} \cos(\theta) & 0 & \sin(\theta) \\ 0 & 1 & 0 \\ -\sin(\theta) & 0 & \cos(\theta) \end{bmatrix} * \begin{bmatrix} \cos(\psi) & -\sin(\psi) & 0 \\ \sin(\psi) & \cos(\psi) & 0 \\ 0 & 0 & 1 \end{bmatrix} =$$

$$\begin{bmatrix} \cos(\theta)\cos(\psi) & -\cos(\phi)\sin(\psi) + \sin(\phi)\sin(\theta)\cos(\psi) & \sin(\phi)\sin(\psi) + \cos(\phi)\sin(\theta)\cos(\psi) \\ \cos(\theta)\sin(\psi) & \cos(\phi)\cos(\psi) + \sin(\phi)\sin(\theta)\sin(\psi) & -\sin(\phi)\cos(\psi) + \cos(\phi)\sin(\theta)\sin(\psi) \\ -\sin(\theta) & \sin(\phi)\cos(\theta) & \cos(\phi)\cos(\theta) \end{bmatrix} \quad (\text{E.1})$$

Using the translation matrix, the RAOs of the centre of gravity are translated to the (starboard) beam tip in Figure E.1.

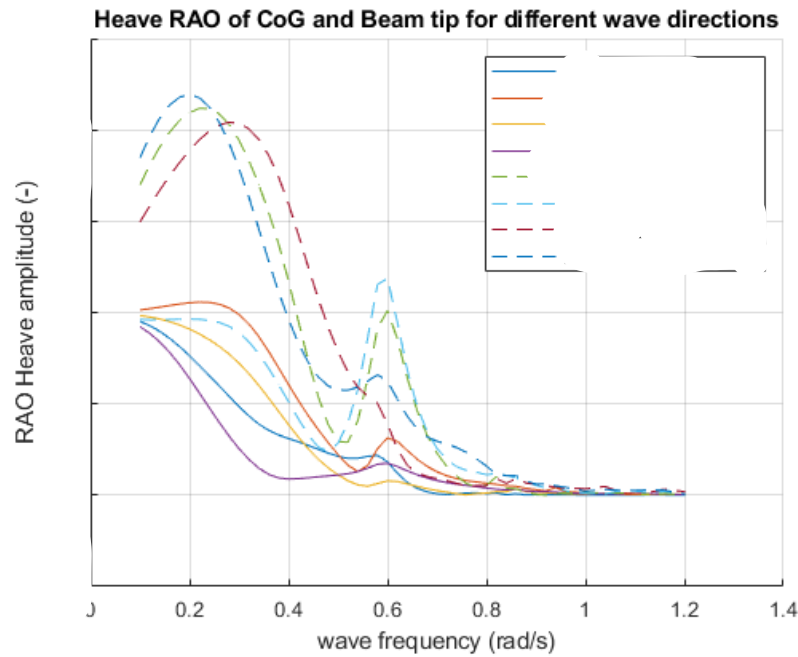


Figure E.1: RAOs of heave amplitude for wave directions 45, 90, 120 and 150 degrees for both the Centre Of Gravity and the starboard beam tip.

It can be seen from the figure that the vessel reacts most intense to beam waves i.e. waves coming from the side, at a 90 degree angle. This also shows in the response spectrum. The response spectrum of a vessel can be computed by multiplying the wave spectrum with the RAO amplitude squared. The wave spectrum that will be used for this calculation is the JONSWAP spectrum.

$$S_v(\omega) = RAO^2 * S_\zeta(\omega) \quad (E.2)$$

Translating the RAOs this way, disregards the effect of that the phases of the RAO have on points that do not lie in the CoG. Because of this limitation, the RAO in the beam tip represents the worst case scenario where heave excitation is in phase with pitch excitation, resulting in a conservatively large heave displacement. This does not mean that the results are wrong, but it must be realized that the RAO and the subsequent response spectrum is (over)conservative. It is possible to implement phase differences in the translation as well, but seeing as the generation of the response spectrum in the beam tip is only done to get a feel for the order of magnitude of the motions, this is seen as an unnecessary time consuming task, yielding minimal additional results.

E.1.1. The JONSWAP spectrum

The wave climate of the North Sea is usually depicted using a Pierson-Moskowitz or Joint North Sea Wave Observation Project (JONSWAP) spectrum, where the JONSWAP spectrum is the more evolved version of the former. Evolved here means, that the wind has been blowing over a large distance, increasing the sea states fetch. A spectrum shows the distribution of energy over the frequencies present in the spectrum. In other words, it tells the reader how many times a certain wave frequency occurs in a given sea state while accounting for the amount of energy that a wave with that frequency carries. The JONSWAP spectrum is defined by Equation E.3.

$$S_J(\omega) = A_\gamma \frac{5}{16} H_s^2 \omega_p^4 \omega^{-5} \exp\left(-\frac{5}{4} \left(\frac{\omega}{\omega_p}\right)^{-4}\right) \gamma^b \quad (E.3)$$

Where: $A_\gamma = 1 - 0.287 \ln(\gamma)$, a normalising factor
 H_s = significant wave height (m) = 2.5m
 ω_p = spectral peak radial frequency (rad/s)
 ω = radial frequency (rad/s)
 γ = non-dimensional peak shape factor = 3.3
 $b = \exp\left[-\frac{1}{2}\left(\frac{\omega - \omega_p}{\sigma\omega_p}\right)^2\right]$
 $\sigma = 0.07$ for $\omega \leq \omega_p$ and 0.09 for $\omega > \omega_p$

The spectrum is dependent on a few input parameters, namely the significant wave height, H_s , and the peak period, T_p . The JLS of Pioneering Spirit operates safely in sea states with significant wave heights up to 2.5 meters and zero-crossing periods of up to 6 seconds. For any wave-spectrum, following the DNV code for the design of offshore wind turbine structures, the relationship between the peak frequency and zero-crossing frequency is the following [34]:

$$T_z = T_p \sqrt{\frac{5 + \gamma}{11 + \gamma}} \quad (\text{E.4})$$

Two sea states will be considered, one for wind waves and one for swell. In swell, the Pierson-Moskowitz spectrum will be used, with a γ of 1. For wind waves, the JONSWAP spectrum is used with a γ of 3.3 [34]. The peak-enhancement factor, γ , is a measure for the development of the wave spectrum over distance (fetch). The higher γ , the more narrow the resulting peak around its peak period [34].

Under the assumption that the wave spectrum is narrow banded, i.e. not too many frequencies present in the spectrum, and the wave elevation can be assumed to be Gaussian distributed, the spectrum follows a Rayleigh distribution. This is useful since it allows for all sorts of statistical analyses to be carried out on not only the wave spectrum but also the response spectrum which will be done in section E.2.

E.2. Response spectrum

This multiplication is graphically represented in Figure E.2. When examining Figure E.2a for frequencies lower than 0.5 radians per second, it is clear that Figure E.2b is the result of Equation E.2 since the spectrum contains little to no energy below this frequency. This is because the JONSWAP spectrum contains almost no energy at these low frequencies and consequently the lower frequencies that are present in the RAOs, are multiplied by 0. The higher frequencies around 0.7 rad/s, are magnified and make up the bulk of the spectrum. This makes sense as high frequency waves carry little energy and are relatively small. Such a small wave will have little to no impact on the motions of a heave vessel such as the PS.

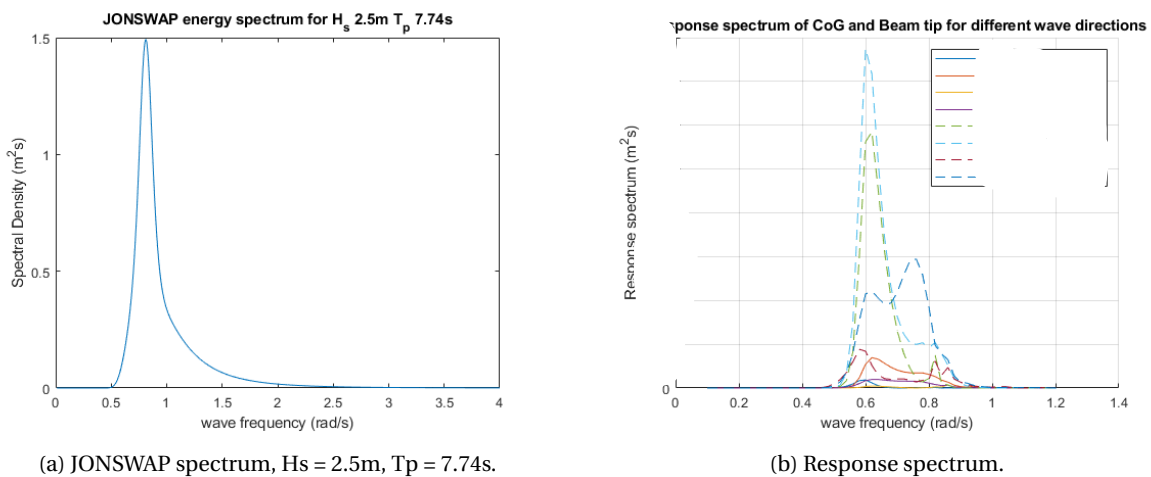


Figure E.2: Response spectrum at CoG and starboard beam tip for wave directions 45, 90, 120 and 150 degrees.

Performing statistical analyses on the response spectrum produces useful information about the spectrum. The response amplitudes are assumed to be Rayleigh distributed if the incoming waves are assumed to be Gaussian and the spectrum is narrow banded. The Rayleigh short term probability density function of the response is then given as [28]:

$$f_{ST}(R_a) = \frac{R_a}{m_{0R}} \exp\left\{-\frac{R_a^2}{2m_{0R}}\right\} \quad (\text{E.5})$$

Where m_{0R} is first spectral moment, representing the area under the curve of the response spectrum and R_a is the response amplitude, in this case heave. The spectral moments are defined by Equation E.6 and Equation E.7 gives the double amplitude of the significant response of the spectrum. This corresponds to the same property as the significant wave height in wave spectra which stands for the mean of the largest one third of waves. Finally, Equation E.8 gives the zero-crossing period of the waves, T_z , which can be translated to a peak period using Equation E.4.

$$m_{nz} = \int_0^\infty S_v(\omega) \omega^n d\omega \quad (\text{E.6})$$

$$2 * R_{s,a} = 4\sqrt{m_{0R}} \quad (\text{E.7})$$

$$T_2 = T_z = 2\pi\sqrt{\frac{m_{0R}}{m_{2R}}} \quad (\text{E.8})$$

Figure E.3 shows how this double significant amplitude is spread over waves coming in from different directions. It is obvious that the PS operates well in head waves and most turbulent in beam waves. This will help later when determining a representative beam tip motion to construct the force on the pile head for the FEM model.

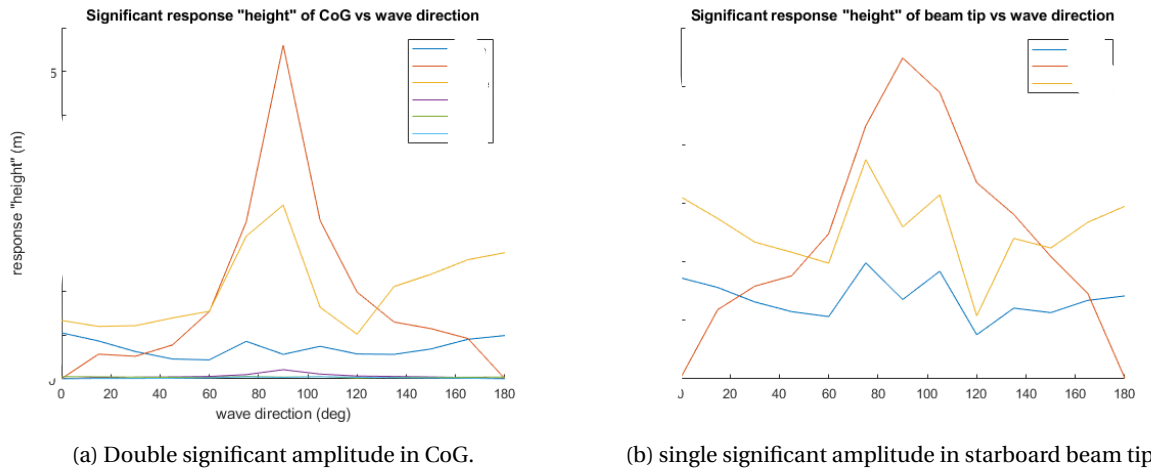
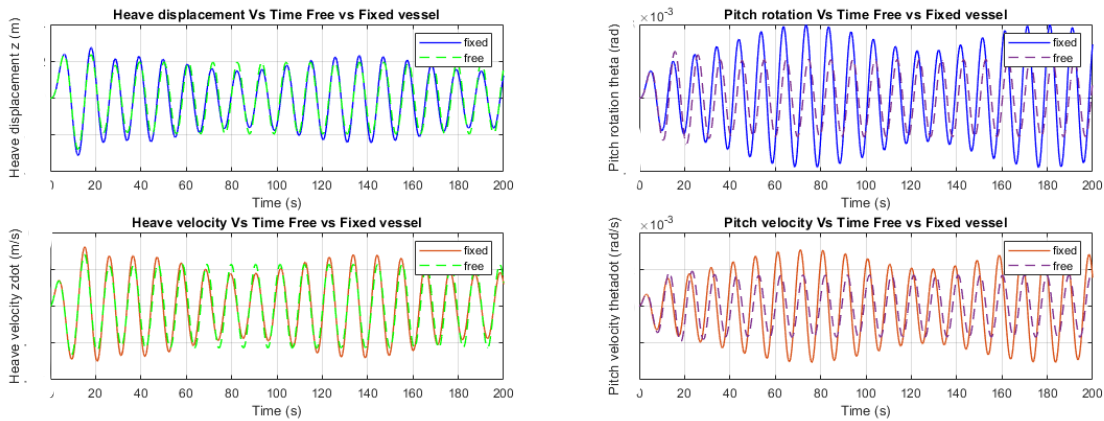


Figure E.3: Single significant amplitudes in centre of gravity and beam tip for different wave directions.

E.3. Fixity effect on added mass and damping

This section checks whether the added mass and damping that are chosen in a free floating condition, do not change too much when the fixity condition is applied. Firstly, it is important to mention that added mass and damping are solely dependent on the frequency of motion of the vessel, meaning that if the frequency of heave and pitch motion does not change, the added mass stays the same as well. Figure E.4 shows the change in vessel response when the fixity condition is applied, showing that the frequency of the heave motion is not affected, only the amplitude is, and the frequency of the pitch motion is adjusted slightly, accompanied by a phase shift. The free and fixed frequencies of motion are shown in Table E.1.



(a) Heave motion and velocity vessel. Free moving period: 10.868s, fixed moving period: 10.884s. (b) Pitch motion and velocity vessel. Free moving period: 9.852s, fixed moving period: 9.652s.

Figure E.4: Heave and pitch displacements and velocities of vessel for fixed and free conditions.

The change in frequency of the heave motion is less than the accuracy of the model, so no change in added mass or damping has to be accounted for. In case of pitch, the change in frequency is ... and the new added mass (which is determined by linear interpolation of the tables in Appendix D) is listed in Table E.1. The changes in added mass and damping in pitch direction in fixed conditions are 0.36% and -0.42% respectively.

Table E.1: Adjusted added mass and damping values for pitch in fixed and free condition.

| | | frequency (rad/s) | added mass (kg) | damping (kg/s v kgm/s) |
|-------|-------|-------------------|-----------------|------------------------|
| Free | Heave | | | |
| | Pitch | | | |
| Fixed | Heave | | | |
| | Pitch | | | |

It is obvious that a 0.36% difference in added mass and a 0.42% difference in damping does not have a significant effect on the response of the vessel.

E.3.1. Pitch and heave data real time lift

The model used in this research only takes one frequency as the forcing frequency and the model is likely to start moving at the forcing frequency as well. Therefore, real time data of PS heave and pitch motion during a jacket lift is analysed as well, to see whether the fixity connection changes PS motions. During the Tyra lift, the following pitch and heave motions at the CoG have been recorded, Figure E.5.

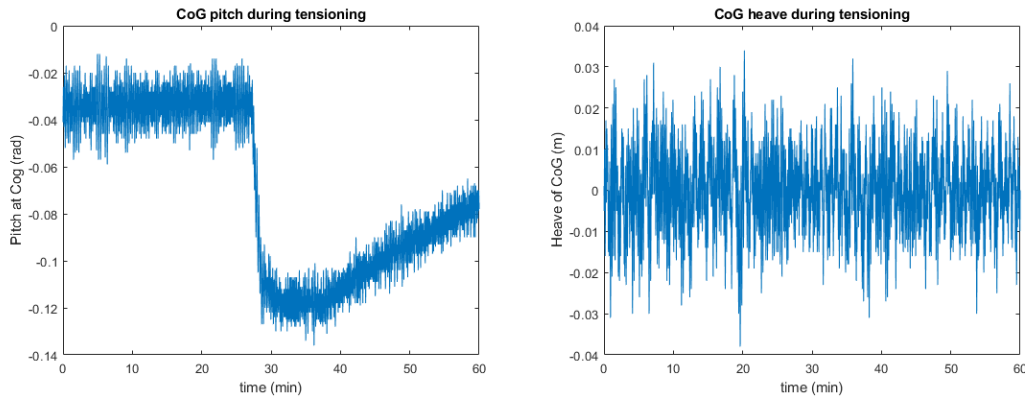


Figure E.5: PS Heave and pitch motion during tensioning procedure of Tyra jacket lift. At around 27 minutes the tensioning starts, after 32 minutes it is complete and the remainder of the plot is ballasting.

A Fast-Fourier-Transform (FFT) of both graphs, yields the frequencies of the oscillations for each of the three stages of the procedure. The answers are listed in Table E.2. The FFT of the heave data is very unclear with a lot of noise. The difference in added mass and damping corresponding to these changes in frequency are also shown. It must be noted that the time window of especially the tensioning part is very small, consisting of only a few minutes. With the large period of motion, only 10 to 20 waves are present during this time and as a result, the FFT might be inaccurate. On top of that, during the lifting of a jacket, the goal is to keep the moment of largest tension as low as possible. Complete tension might only exist for several seconds before the jacket is lifted from its foundation. This makes the results of the FFT more uncertain.

| | Heave period (s) | Pitch period (s) |
|--------------------------|------------------|------------------|
| Pre-tensioning | | |
| During tensioning | | |
| Change in added mass (%) | | |
| Change in damping (%) | | |

Table E.2: Fast-Fourier-Transform results of Tyra data in Figure E.5.

E.4. Sensitivity analysis

The previous section concluded that a change in vessel frequency due to the fixity condition may result in a 10% difference in added mass in heave motion and a 8% difference in damping in pitch motion. This section investigates the effect of varying those parameters by 10 and 20%. Table E.3 shows the input parameters as well as the results, in the form of amplitude of the resulting crane-master force from the vessel model. The amplitude is taken as the largest difference between a peak and a subsequent trough in a 100 second simulation, corresponding to the force amplitude at a quarter of the beating frequency.

| | -20% | -10% | normal | +10% | +20% |
|----------------------------------|------|------|--------|------|------|
| a_{33} (kg) | | | | | |
| a_{55} (kg) | | | | | |
| b_{33} (kg/s) | | | | | |
| b_{55} (kgm/s) | | | | | |
| Cranemaster force amplitude (MN) | 82.1 | 79.1 | 72.0 | 66.2 | 58.8 |

Table E.3: Added mass and damping sensitivity analysis input parameters varying both with $\pm 20\%$. Results are given as the largest amplitude in the resulting crane-master force.

If the added mass and damping are reduced, the crane-master force amplitude increases, if they are increased, the force amplitude decreases. This makes sense, seeing as more inertia is added to the system, the response

is less intense. A 10% decrease from the original values results in a 9.9 MN increase in force amplitude, which is quite significant. It is thus concluded that the model is sensitive to both parameters and more calculation of both in a fixed condition is required in a future model.

F

Resonance frequency

Since the OpenSees model consists of non-linear springs, determining the resonance frequency is not as straightforward as it is for linear systems. Knowing where the resonance frequency lies, gives a better understanding of the model and its response to vessel forcing. This chapter proposes a method to determine the resonance frequency and immediately presents the results.

The method is as follows:

1. Build the model and apply a harmonic force.
2. While keeping the forcing amplitude and mean constant, change the frequency.
3. Record the displacement of the topmost node at a given moment in time, for each simulation with a different harmonic excitation frequency.
4. Plot the result in a displacement vs forcing frequency plot.

The result is plotted in Figure E.1. It can be seen that the system responds most extensively to excitations with frequencies around 10 to 20 Hz, which clearly lies far away from the forcing frequency due to vessel motion and wave excitation, which is in the range of 0.05 to 0.2 Hz.

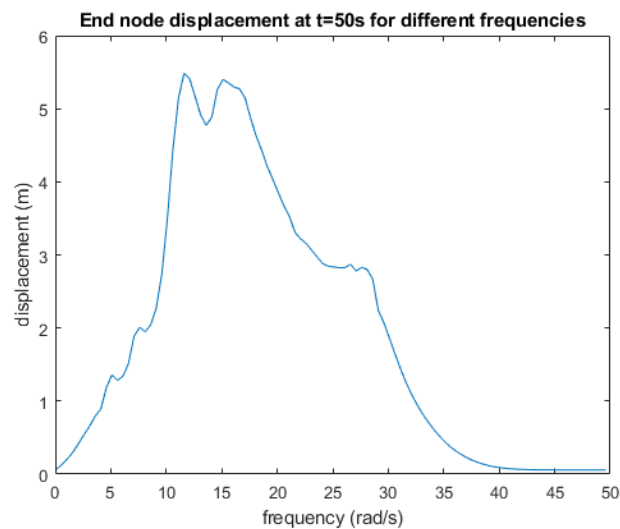


Figure E.1: Nodal displacement vs forcing frequency for the topmost node after 50 seconds of simulation.

G

Mesh convergence study

A number of elements convergence study is carried out to see if the results of the OpenSees FEM model are accurate while keeping computational time at a minimum. This can be compared to a mesh convergence study but the model is not in 3D, so only the number of nodes (and consequently elements) influence the accuracy of the model. The more Degrees Of Freedom present in the model, the better the model will capture the behavior of the pile-soil interaction, but adding more DOFs also makes the simulation more complex and hence, solve time is increased. A balance between the two -number of DOFs and solve time- is desired. The result of the model should be independent of mesh size in order to be accurate. To check if this is the case, the model is run with an increasing number of elements and the nodal displacement as well as the force-displacement graphs are checked for convergence. This process is shown in Figure G.1.

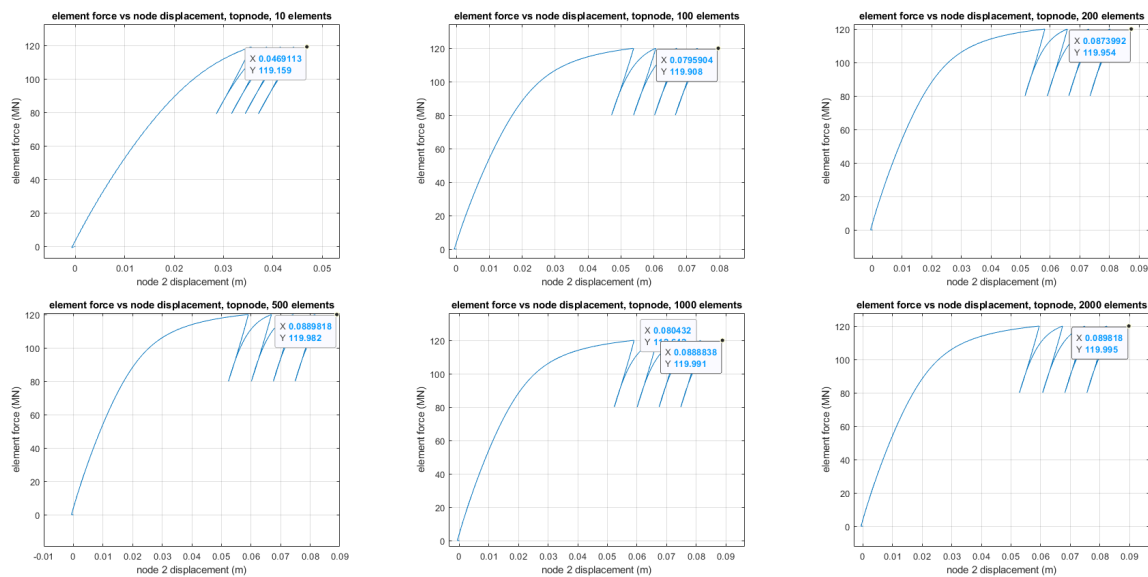


Figure G.1: Force-displacement graphs with varying number of elements used to construct the monopile. Number of elements from top left to bottom right: 10, 100, 200, 500, 1000, 2000.

The computational time of each simulation is recorded as well and combining this with the previously obtained data for maximum nodal displacement and force measured in the topmost element at this displacement, Figure G.2 is obtained. The maximum values are also reported in Table G.1. Based on this graph and the data from the table, 2000 elements is considered as an appropriate number of elements to ensure accurate results while keeping computational time as low as possible. To obtain intermediate results quickly, a pile consisting of 500 elements is used to produce ballpark figure numbers.

| Number of elements | Topnode displacement (m) | Computational time (s) | Difference (%) |
|--------------------|--------------------------|------------------------|----------------|
| 10 | 0.046911 | 26 | - |
| 100 | 0.0795904 | 27 | 69.66 |
| 200 | 0.0873992 | 28 | 9.81 |
| 500 | 0.0889818 | 50 | 1.81 |
| 1000 | 0.0888838 | 108 | -0.11 |
| 2000 | 0.089818 | 236 | 1.05 |
| 5000 | 0.0899881 | 654 | 0.19 |

Table G.1: Data obtained in mesh convergence study.

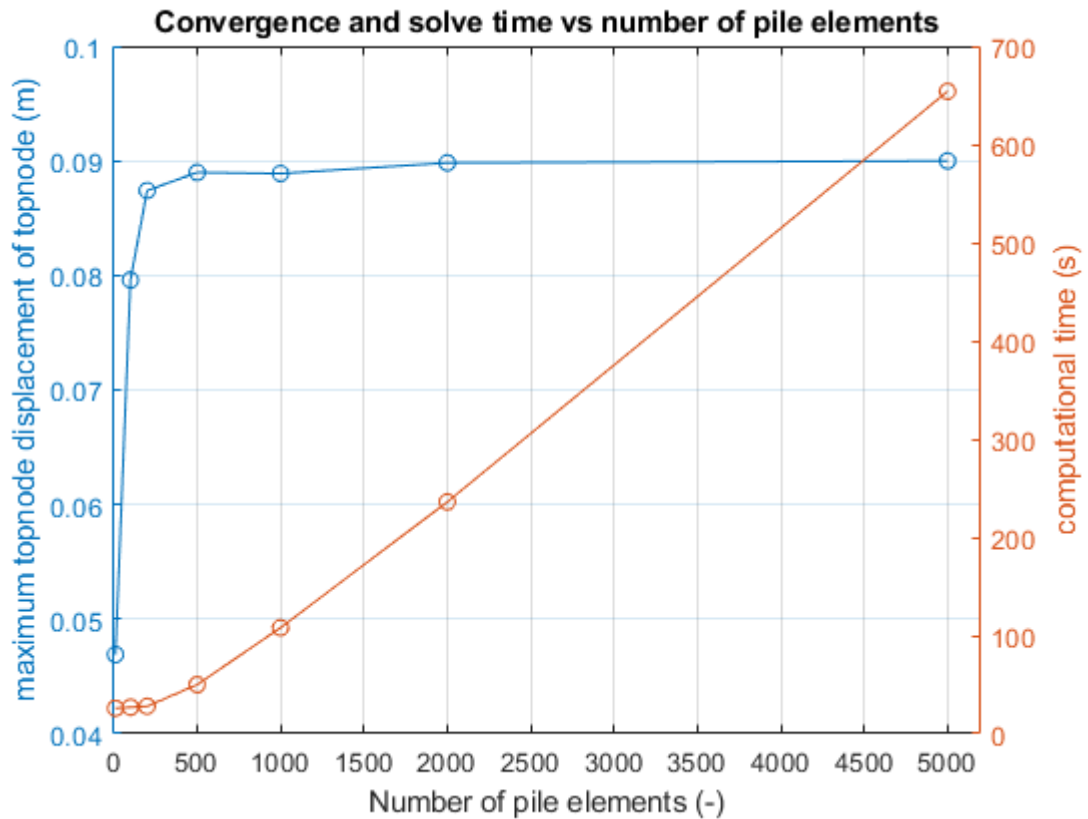
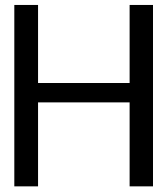


Figure G.2: Convergence of topnode displacement and computational time versus number of pile elements.

Using 500 elements to represent homogeneous soil accurately seems like a lot but when considering the discretization of soils based on τ_{ult} in the t-z elements, it makes more sense. The ultimate capacity of every soil layer is calculated by multiplication with the depth of that element. If the mesh becomes more coarse meaning that the depth of every element is determined more accurately, the result will change. Consequently, the z_{50} values are also dependent on this depth, adding to the sensitivity.



OpenSees code

This appendix first shows the MATLAB code used in the hydrodynamical vessel model and the presents the OpenSees model representing the pile-soil interaction (which is also written in MATLAB).

H.1. Vessel model

```
1 tspan = [0 1000];
2 x0 = [0.0; 0; 0.0; 0; 0.0; 0.0]; % initial disp. and vel. is 0. for all 3 DOF.
3 % x = [z; zdot; theta; thetadot; u; udot]
4 [t,x] = ode45(@Three_DOF,tspan,x0);
5
6 F_output = zeros(length(t),2);
7
8 for i = 1:length(t) % moet x(i,:) niet x0 zijn?
9     F_output(i,:) = Three_DOF(t(i),x(i,:),2);
10 end
11 F_cranemaster = F_output(:,1);
12 F_cables = F_output(:,2);
13
14 % Make a ramp up part to the forcing.
15 % global tension_array
16 % tensioning = tension_array;
17 tensioning = 138e6; % 27.6 for 4*F_cm, 42.5 for 2*F_cm. 75.0 for 6*F_cm
18 w = 2*pi/40; % 10s rampup time
19 [peak_value_cm, peak_index_cm] = findpeaks(F_cranemaster);
20
21 for i = 1:length(peak_index_cm)
22     if peak_index_cm(i+1)-peak_index_cm(i) < 280
23         amp(i) = 0;
24     else
25         amp(i) = peak_value_cm(i+1);
26         index_jump = peak_index_cm(i+1);
27         break
28     end
29 end
30 zero_indeces = find(amp==0); % Selects zeros
31 amp(zero_indeces) = []; % deletes zeros
32
33 rampup2 = (tensioning+amp)*sin(w*t);
34 [peak_value_rampup, peak_index_rampup] = findpeaks(rampup2);
35
36 arbitrary = 50;
37 subtract = (peak_index_rampup(1))-index_jump+arbitrary; % Makes the y_resulting ...
38     vector as long as time.
39 y_resulting = [rampup2(1:peak_index_rampup(1)-1); ...
40     tensioning+F_cranemaster(index_jump:(end-subtract))]; % Jermain smartness, geen ...
41     loop nodig
```

```

40 figure
41 plot(t(1:min(length(t),length(y_resulting))),y_resulting(1:min(length(t),length(y_resulting)),1)/1e6)
42 grid on
43 % hold on
44 % yline(80.4,'-or','LineWidth',2)
45 % txt2 = 'max. force = 80.4 MN';
46 % text(50,83,txt2)
47 % yline(89.1,'or','LineWidth',2)
48 % txt = 't_{ult}'
49 % text(25,86,txt)
50 % yline(54.8,'-or','LineWidth',2)
51 % txt2 = 'max. force = 54.8 MN';
52 % text(50,58,txt2)
53 % yline(89.1,'or','LineWidth',2)
54 % txt = 't_{ult}'
55 % text(50,85,txt)
56 % title('Model input force with rampup'); xlabel('time (s)'); ylabel('force (MN)'); ...
    grid on
57
58 figure()
59 plot(t,F_output(:,1)/1e6); xlabel('time (s)'); ylabel('force (MN)'); title('Force in ...
    cranemaster'); grid on
60
61 [peak_check_value, peak_check_index] = findpeaks(x(:,1));
62 [peak_check_value_pitch, peak_check_index_pitch] = findpeaks(x(:,3));
63
64 for i = 1:length(peak_check_index)-1
65     period(i) = (t(peak_check_index(i+1))-t(peak_check_index(i)));
66     pitch_period(i) = (t(peak_check_index_pitch(i+1))-t(peak_check_index_pitch(i)));
67 end
68 period_output_heave_fixed = mean(period);
69 period_output_pitch_fixed = mean(pitch_period);
70
71 freq_heave_fixed = 2*pi/period_output_heave_fixed;
72 freq_pitch_fixed = 2*pi/period_output_pitch_fixed;
73 %%%%%%%%%%%%%%%%%%%%%%%%%%%%%%%%%%%%%%%%%%%%%%%%%%%%%%%%%%%%%%%%%%%%%%%%%
74 % Plots
75 %%%%%%%%%%%%%%%%%%%%%%%%%%%%%%%%%%%%%%%%%%%%%%%%%%%%%%%%%%%%%%%%%%%%%%%%%
76
77 figure()
78 subplot(2,1,1)
79 plot(t,x(:,1), 'color','b','LineWidth',1)
80 grid on
81 xlabel('Time (s)')
82 ylabel('Heave displacement z (m)')
83 title('Heave displacement Vs Time (Free decay)')
84
85 subplot(2,1,2)
86 plot(t,x(:,2), 'color','#D95319','LineWidth',1)
87 grid on
88 xlabel('Time (s)')
89 ylabel('Heave velocity zdot (m/s)')
90 title('Heave velocity Vs Time (Free decay)')
91 pos1 = get(gcf,'Position');
92 set(gcf,'Position', pos1 - [pos1(3)/2,0,0,0])
93
94 figure()
95 subplot(2,1,1)
96 plot(t,x(:,3), 'color','b','LineWidth',1)
97 grid on
98 xlabel('Time (s)')
99 ylabel('Pitch rotation theta (rad)')
100 title('Pitch rotation Vs Time (Free decay)')
101
102 subplot(2,1,2)
103 plot(t,x(:,4), 'color','#D95319','LineWidth',1)
104 grid on
105 xlabel('Time (s)')
106 ylabel('Pitch velocity thetadot (rad/s)')
107 title('Pitch velocity Vs Time (Free decay)')
108 pos2 = get(gcf,'Position');

```

```

109 set(gcf, 'Position', pos2 + [pos2(3)/2,0,0,0])
110
111 figure()
112 subplot(2,1,1)
113 plot(t,x(:,5), 'color', 'b', 'LineWidth', 1)
114 grid on
115 xlabel('Time (t)')
116 ylabel('Cable displacement u (m)')
117 title('Cable displacement Vs Time (Forced Vibration)')
118
119 subplot(2,1,2)
120 plot(t,x(:,6), 'color', '#D95319', 'LineWidth', 1)
121 grid on
122 xlabel('Time (t)')
123 ylabel('Cable velocity udot (m/s)')
124 title('Cable velocity Vs Time (Forced Vibration)')
125 pos3 = get(gcf, 'Position');
126 set(gcf, 'Position', pos3 - [pos3(3)/2, 0.91*pos3(2), 0, 0])
127
128 function [dxdt] = Three_DOF(t,x,optie)
129 if nargin == 2
130     optie = 1;
131 end
132
133 m = % vessel mass
134 m55 = % pitch inertia
135 mh = % hoist block mass
136 l = % arm between beam tip and CoG (m)
137
138 % Hydrostatic stiffnes
139 c33 =
140 c55 =
141
142 % New and last method. Added mass and damping are taken from .lis files at the ...
143 % forcing frequency, that is the frequency from the motion report!
144 % Frequencies are:
145 % JONSWAP. gamma 3.3
146 % x33 = ; v33 = ; a33 =
147 % x55 = ; v55 = a55 =
148 % PM. gamma 1.0
149 % x33 = ; v33 = ; a33 =
150 % PM. gamma 0.0
151 x33 = v33 =
152 x55 = ; v55 =
153
154 wnh = v33/x33; % wnh = is 1 sec. wnh =
155 wnp = v55/x55; % free wnp = 0 rad/s. fixed wnp = /s
156
157 % 80%
158 % a33 = % (c33-wnh^2*m)/wnh^2; %
159 % a55 = % (c55-wnp^2*m55)/wnp^2; %
160 % zeta33 = % zeta33 = 100
161 % zeta55 = % zeta55 = 100
162
163 % 90%
164 % a33 = %zeta33*2*sqrt(c33*(m+a33)); %
165 % a55 = %zeta55*2*sqrt(c55*(m55+a55)); % i
166 % b33 =
167 % b55 =
168
169 % 100%
170 a33 =
171 a55 =
172 b33 =
173 b55 =
174
175 % 110%
176 % a33 =

```

```

177 % a55 =
178 % b33 =
179 % b55 =
180
181 % 120%
182 % a33 =
183 % a55 =
184 % b33 =
185 % b55 =
186
187 % Forces to match CoG movement from motion report for 3 different gamma values. ...
      AQWA natural periods Th = , Tp =
188 % gamma = 0.0
189 Fa = ; % at omega100% Fa = at omega50% Fa = at ...
      omega200% Fa =
190 Ma = ; % at omega100% Ma = at omega50% Ma = at ...
      omega200% Ma =
191
192 % % gamma = 1.0 TO DO if necessary
193 % Fa =
194 % Ma =
195 % w1 =
196 % w2 =
197 %
198 % % gamma = 3.3 TO DO if necessary
199 % Fa =
200 % Ma =
201 % w1 =
202 % w2 =
203
204 %%% Cable and sling constants
205 length_cable = 75;
206 k_r = 0.5; % reduction factor of k_c due to beam stiffness and derrick hoist stiffness
207 k_c = k_r*(310e6/length_cable)*40*3*2; % cable stiffness, 40 is 20*2 voor ...
      vertraging, 3 is 3 main hoist blokken, 2 is 2 beams
208
209 Δ = 0.1;
210 zeta = 1/(sqrt(1+(2*pi/Δ)^2));
211 m_c = 27.7*75*40*3*2;
212 b_c = zeta*2*sqrt(k_c*m_c);
213
214 F_cables = x(5)*k_c + x(6)*b_c;
215
216 %%% CRANEMASTER parameters
217 % F_data = 5*9.81*1000*[595.9; 606.4; 617.2; 628.4; 639.8; 651.5; 663.6; 676.0; ...
      688.7; 701.9; 715.4; 729.3; 743.6; 758.3; 773.5; 789.1; 805.3; 821.9; 839.0; ...
      856.7; 875.0; 893.9; 913.3; 933.4; 954.2; 975.7; 998.0; 1021.0; 1044.8; 1069.5; ...
      1095.0];
218 F_data = -780.928 + [595.9; 606.4; 617.2; 628.4; 639.8; 651.5; 663.6; 676.0; 688.7; ...
      701.9; 715.4; 729.3; 743.6; 758.3; 773.5; 789.1; 805.3; 821.9; 839.0; 856.7; ...
      875.0; 893.9; 913.3; 933.4; 954.2; 975.7; 998.0; 1021.0; 1044.8; 1069.5; 1095.0];
219 F_data = 5*9.81*1000*F_data; % -780 is subtracting the mean, and makes it start at ...
      x=2.0, middle of the stroke. This makes sure there is no oscillations in the ...
      beginning.
220 x_data = [0; 0.13; 0.27; 0.4; 0.53; 0.67; 0.8; 0.93; 1.07; 1.2; 1.33; 1.47; 1.6; ...
      1.73; 1.87; 2.0; 2.13; 2.27; 2.4; 2.53; 2.67; 2.8; 2.93; 3.07; 3.20; 3.33; 3.47; ...
      3.60; 3.73; 3.87; 4.0];
221 x_data = x_data-2;
222 k_coefficients = polyfit(x_data,F_data,2);
223
224 v_data = [-1.73; -1.15; -0.77; -0.51; -0.34; -0.23; -0.15; -0.10; -0.07; -0.05; ...
      -0.03; -0.02; 0.00; 0.02; 0.03; 0.05; 0.07; 0.10; 0.15; 0.23; 0.34; 0.51; 0.77; ...
      1.15; 1.73; 2.59];
225 b_force_mirror = 5*1000*[299.01; 132.89; 59.06; 26.25; 11.67; 5.19; 2.30; 1.02; 0.46; ...
      0.20; 0.09; 0.04; 0.00; 0.04; 0.09; 0.20; 0.46; 1.02; 2.30; 5.19; 11.67; 26.25; ...
      59.06; 132.89; 299.01; 672.78];
226 b_coefficients = polyfit(v_data,b_force_mirror,2);
227
228 % F_cranemaster = 6*((k_coefficients(1)*(x(5)+2)^2 + k_coefficients(2)*(x(5)+2) + ...
      k_coefficients(3) + b_coefficients(1)*x(6)*abs(x(6)) + b_coefficients(2)*x(6) + ...
      b_coefficients(3)));

```

```

229 F_cranemaster = 6*((k_coefficients(1)*(x(5))^2 + k_coefficients(2)*(x(5)) + ...
      k_coefficients(3) + b_coefficients(1)*x(6)*abs(x(6)) + b_coefficients(2)*x(6) + ...
      b_coefficients(3)));
230
231 % F_cranemaster = 0;
232 % k_c = 0; b_c = 0;
233 % F_cables = 0;
234
235 % Matrices
236 EOM1 = (Fa*sin(wnh*t)-(c33+k_c)*x(1) + k_c*1*x(3) + k_c*x(5) - (b33+b_c)*x(2) + ...
      b_c*1*x(4) + b_c*x(6))/(m+a33);
237 EOM2 = (Ma*sin(wnp*t)-(c55+k_c*1^2)*x(3) + k_c*1*x(1) - k_c*1*x(5) - ...
      (b55+b_c*1^2)*x(4) + b_c*1*x(2) - b_c*1*x(6))/(m55+a55);
238 EOM3 = (k_c*x(1) - k_c*1*x(3) - k_c*x(5) + b_c*(x(2) - 1*x(4) - x(6)) - ...
      F_cranemaster)/mh;
239
240 dxdt = [x(2); EOM1; x(4); EOM2; x(6); EOM3];
241
242 % Extract F_cranemaster & F_cables
243 if optie == 2
244     dxdt = [F_cranemaster F_cables];
245 end
246 end

```

H.2. OpenSees model main code

```

1 clear variables
2 clc
3
4 % Main file model
5 %delete checkMain.out
6
7 % Import files to write in
8 [fIDmain, fID1, fID2, fID3, fID4] = load_files();
9
10 fprintf(fIDmain, '#hello this is the start of the main tcl file \n');
11 fprintf(fIDmain, 'wipe \n');
12
13 [nNodeEmbed] = Create_Nodes(fID1); % This function has input and output.
14 fprintf(fIDmain, 'source Create_Nodes.tcl \n');
15
16 parameters
17
18 [tau_ult_force, tau_ult_calibration, z50,ultimate_capacity] = tz_spring(fID2,nNodeEmbed);
19 fprintf(fIDmain, 'source tz_spring.tcl \n');
20
21 Create_Elements(fID3);
22 fprintf(fIDmain, 'source Create_Elements.tcl \n');
23
24 fprintf(fIDmain, 'recorder Element -file allforce.out -time -eleRange 1 %i force \n', ...
      nNodePile);
25 fprintf(fIDmain, 'recorder Node -file allnodedisp.out -time -nodeRange 20001 %i -dof ...
      3 disp \n', 20000 + nNodePile);
26
27 fprintf(fIDmain, 'recorder Element -file zeroforce.out -time -eleRange 10000 %i force ...
      \n', 10000+nNodeEmbed);
28
29 % Normal run
30 % global tension_array
31 % tension_array = 20e6;
32 Loading(fID4);
33 fprintf(fIDmain, 'source Loading.tcl \n');
34
35 !OpenSees.exe main.tcl
36 read_output
37
38
39 % varying tension

```

```

40 % global tension_array
41 % for i = 1:40
42 %     tension_array = i*1e6+31e6;
43 %     Loading(fID4);
44 %     fprintf(fIDmain, 'source Loading.tcl \n');
45 %     fprintf(fIDmain, 'print -file checkMain.out \n');
46 %     !OpenSees.exe main.tcl
47 %     read_output
48 %     final_disp(i) = node_disp(end-1,end);
49 %     final_force(i) = element_force(end-1,end);
50 % end
51
52 % varying beta
53 % outcome = fopen("results\beta_variation\beta5.tcl",'w');
54 % for i = 1:length(element_force)
55 %     fprintf(outcome, '%.10f %.10f \n', node_disp(i,end), element_force(i,end));
56 % end
57
58 % Clays
59 for i = 1:length(c_u)
60     fprintf('the ultimate capacity for c_u(z) = %.2f (kPa) is %.3f MN \n', ...
        c_u(i)/1e3, ultimate_capacity(i)/1e6)
61 end
62
63 % Sands
64 % for i = 1:length(beta1)
65 %     fprintf('the ultimate capacity for beta = %.2f is %.3f MN \n', beta1(i), ...
        ultimate_capacity(i)/1e6)
66 % end
67
68
69 %%
70 % tension = linspace(32,72,40);
71 % figure
72 % plot(final_disp(1,1:end),tension);title('final node displacement vs teansioning ...
        force');xlabel('final node displacement (m)');ylabel('tension force (MN)'); grid on

```

H.3. MATLAB functions in order of usage of main file for OpenSees model

```

1 function [nNodeEmbed] = Create_Nodes (blitz)
2 parameters
3
4 fprintf(blitz, '# Model setup \n \n');
5 fprintf(blitz, 'model BasicBuilder -ndm 3 -ndf 6 \n \n');
6
7 %%%%%%%%%%%%%%%%%%%%%%%%%%%%%%%%%%%%%%%%%%%%%%%%%%%%%%%%%%% Spring nodes
8 nNodeEmbed = ceil((L2/(L1+L2))*totalelements);
9 fixednode = zeros(nNodeEmbed,3);
10 slavenode = zeros(nNodeEmbed,3);
11 zCoord = zeros(nNodeEmbed,1);
12 fprintf(blitz, '#fixed spring nodes and slave nodes and their fixities \n \n');
13
14 for i = 1:(nNodeEmbed)
15     zCoord(i) = eleSize*(i-1); % i-1 because ...
16     first node should be at 0,0,0
17     fprintf(blitz,'node %i 0 0 %.8f \n', i, zCoord(i)); % Create ...
18     fixed spring node coordinates
19     fprintf(blitz,'fix %i %i %i %i %i %i \n', i, 1, 1, 1, 1, 1);
20     fprintf(blitz,'node %i 0 0 %.8f \n', i+10000, zCoord(i)); % Create ...
21     slave spring node coordinates
22     fprintf(blitz,'fix %i %i %i %i %i %i \n', i+10000, 1, 1, 0, 1, 1);
23 end
24
25 %%%%%%%%%%%%%%%%%%%%%%%%%%%%%%%%%%%%%%%%%%%%%%%%%%%%%%%%%%% Pile nodes
26 fprintf(blitz, '# Create pile nodes \n \n');
27 fprintf(blitz, 'model BasicBuilder -ndm 3 -ndf 6 \n');
28 fprintf(blitz, 'geomTransf Linear 1 0.0 -1.0 0.0 \n \n');
29

```

```

27 fprintf(blitz,'node 20001 0 0 0.0 \n'); ...
    % Create bottom node
28 fprintf(blitz,'fix 20001 1 1 0 1 1 \n'); ...
    % Fix bottom node to check pile extension
29
30 for i = 2:(nNodePile-1) % -1 because the top node should not be fixed
31     zCoord(i) = eleSize*(i-1);
32     fprintf(blitz,'node %i 0 0 %.8f \n', i+20000, zCoord(i)); ...
        % Create pile nodes except topnode
33     fprintf(blitz,'fix %i %i %i %i %i \n', i+20000, 1, 1, 0, 1, 1, 1); ...
        % Constrain pile nodes in 5 DOF, z-direction excluded
34 end
35
36 fprintf(blitz,'node %i 0 0 %.8f \n', 20000+nNodePile, zCoord(end)+eleSize); ...
        % Create topmost pile node
37 fprintf(blitz,'fix %i %i %i %i %i %i \n', 20000+nNodePile, 1, 1, 0, 1, 1, 1); ...
        % Fix topmost pile node
38
39 end
40
41
42 % Soil parameters FILE
43 g = 9.81; % m/s^2
44 phi = [30.0, 32.5, 37.5, 42.5, 45.0]; % made up myself
45 beta1 = [0.21, 0.29, 0.37, 0.46, 0.56]; % From report table, API and DNV use ...
    last 4 values.
46
47 gamma1 = 10.0E3; %
48 kf = [2228.6, 4400.0, 6571.4, 8742.8, 10914.2, 13085.6, 15257.0, 17428.4, 19599.8, ...
    21771.2, 23942.6, 26114, 28285.4, 30456.8];
49 fric = [24.8, 26.6, 28.0, 30.3, 32.1, 33.9, 35.7, 37.6, 39.4, 41.2, 43.1, 44.9, 46.7, ...
    48.5];
50
51 kf_clay = 1e6*[8.5, 15, 32.5, 75, 137.5, 200]; %Source ...
    https://www.finesoftware.eu/help/geo5/en/secant-modulus-of-soil-es-02/
52 c_u = 1e3*[15, 30, 57.5, 112.5, 225, 300];
53
54 % Pile properties and mesh elements
55 L1 = 35.0; % Length above seabed level (m)
56 L2 = 38.0; % Length of embedded pile (m)
57 Dout = 6.5; % Outside diameter (m)
58 t = 0.080; % Wall thickness (mm)
59 Din = Dout-2*t; % Inside diameter (m)
60 totalelements = 200; % Total pile elements
61 eleSize = (L1+L2)/totalelements; % Element size (m)
62 nNodePile = 1 + totalelements; % Number of pile nodes, 1 more ...
    than pile elements (-)
63
64 % Steel properties
65 E = 210E9; % Pa
66 A = 0.25*pi*(Dout^2-Din^2); % m^2
67 Ix = ((pi*Dout^4)-(pi*Din^4))/64; % m^4
68 Iy = Ix;
69 Iz = ((pi*Dout^4)-(pi*Din^4))/32; % m^2 is J in element command.
70 G = 80E9; % Pa
71 rhos = 7800; % kg/m^3
72
73 % Loading
74 timestep = 0.01;
75
76 function [tau_ult_force, tau_ult_calibration, z50, ultimate_capacity] = ...
    tz_spring(fID2,nNodeEmbed)
77
78 [tau_ult_force, tau_ult_calibration, z50, ultimate_capacity] = get_tz_test(nNodeEmbed);
79 parameters
80
81 % clc; clear all; close all;
82 % [fIDmain, fID1, fID2, fID3, fID4] = load_files();
83 % [nNodeEmbed] = Create_Nodes(fID1,L1,L2,Dout,totalelements,eleSize,nNodePile,A,rhos);
84 % [tau_ult_force, tau_ult_calibration, z50] = ...
    get_tz(eleSize,gamma1,beta1,Dout,phi,fric,kf,nNodeEmbed,Din,L2);

```

```

85
86 fprintf(fID2,'# Define the spring material using a t-z curve and hysteresis in ...
    TzSimple1 command \n\n');
87
88
89 for i=1:nNodeEmbed
90     %          uniaxialMaterial TzSimple1 $matTag $tzType $tult    $z50 <$c>
91     fprintf(fID2,'uniaxialMaterial TzSimple1    %i    %i    %.8f    %.15f    %.1f ...
        \n', i, 1, tau_ult_force(i,6), z50(i,6), 0.0);
92 end
    determines which beta you use, third column is beta 0.37                                %the 3 ...
93
94 % Create zero-length elements
95 fprintf(fID2,'# Create zero-length elements \n');
96
97 for i=1:nNodeEmbed
98     %          zeroLength eleTag, node i, node j, -mat tags associated ...
        with previously defined uniaxialMaterial, -dir specify in what direction the ...
        zeroLength element works
99     fprintf(fID2,'element zeroLength    %i    %i    %i    -mat %i -dir %i \n', ...
        i+10000, i, 10000+i, i, 3); % might need to switch i and j node.
100 end
101
102 % Define equal DOF between pile nodes and slave nodes
103
104 for i=1:nNodeEmbed
105     %          equalDOF $rNodeTag $cNodeTag $dof1 $dof2 ...
106     fprintf(fID2,'equalDOF    %i    %i    %i \n', i+10000, i+20000, 3); % Maybe ...
        add more DOF than only the 3rd.
107 end
108 end
109
110 function [tau_ult_force, tau_ult_calibration, z50, ultimate_capacity] = ...
    get_tz_test(nNodeEmbed)
111
112 % clc
113 % clear
114
115 parameters
116 % [fIDmain, fID1, fID2, fID3, fID4] = load_files();
117 % [nNodeEmbed] = Create_Nodes(fID1);%L1,L2,Dout,totalelements,eleSize,nNodePile,A,rhos);
118
119
120 % get_tz_test takes f_lim into account
121 f_lim = 1e3*[48, 67, 81, 96, 115];
122 % Calculation of tau_ult for calibration and TzSimple1 command
123 tau_ult_force = zeros(nNodeEmbed,length(beta1));
124 tau_ult_calibration = zeros(nNodeEmbed,length(beta1));
125 z = linspace(0.1,L2,nNodeEmbed);
126 fz = zeros(length(z),length(beta1));
127
128 % % Sands
129 % Including tau_lim
130 %
131 % for i = 1:nNodeEmbed
132 %     for j = 1:length(beta1)
133 %         if beta1(j)*gammal*z(i) <= f_lim(j)
134 %             fz(i,j) = beta1(j)*gammal*z(i);
135 %         else
136 %             fz(i,j) = f_lim(j);
137 %         end
138 %         tau_ult_force(i,j) = fz(i,j)*pi*(Dout+Din)*eleSize; % Use this in the command ...
        TzSimple1 for tult. Units: N.
139 %         tau_ult_calibration(i,j) = fz(i,j); % Use this in the calibration of z50 = ...
        tult/kSI. Units: N/m^2
140 %     end
141 % end
142 % tau_ult_force = flip(tau_ult_force);
143 % tau_ult_calibration = flip(tau_ult_calibration);
144 % ultimate_capacity = sum(tau_ult_force);
145 %

```

```

146 % % Excluding tau_lim
147 % % for i = 1:nNodeEmbed
148 % %     for j = 1:length(beta1)
149 % %         fz(i,j) = beta1(j)*gammal*z(i);
150 % %         tau_ult_force(i,j) = fz(i,j)*pi*(Dout+Din)*eleSize;
151 % %         tau_ult_calibration(i,j) = fz(i,j);
152 % %     end
153 % % end
154 % % tau_ult_force = flip(tau_ult_force);
155 % % tau_ult_calibration = flip(tau_ult_calibration);
156 % % ultimate_capacity = sum(tau_ult_force);
157 %
158 % % Interpolation of Ef
159 % k_sand = zeros(length(kf),1);
160 % kSI = zeros(1,length(beta1));
161 % for i = 1:length(phi)
162 %     if phi(i) < fric(1)
163 %         k_sand(i) = kf(1);
164 %     elseif phi(i) > fric(end)
165 %         k_sand(i) = kf(end);
166 %     else
167 %         k_sand(i) = interp1(fric,kf,phi(i));
168 %     end
169 %     kSI(i) = k_sand(i)*(47.88/0.0254);
170 % end
171 %
172 % z50 = zeros(nNodeEmbed,length(beta1));
173 % for i = 1:length(beta1)
174 %     z50(:,i) = tau_ult_calibration(:,i)/kSI(i);
175 % end
176
177 % % Clays, NEED TO CHANGE Z50 determination, now that for sands is used.
178 Psi = zeros(nNodeEmbed,length(c_u));
179 alph = zeros(nNodeEmbed,length(c_u));
180 firsthalf = zeros(nNodeEmbed,length(c_u));
181 secondhalf = zeros(nNodeEmbed,length(c_u));
182
183 for i = 1:nNodeEmbed
184     for j = 1:length(c_u)
185         Psi(i,j) = c_u(j)/(z(i)*gammal);
186         if Psi(i,j) ≤ 1.0
187             alph(i,j) = 0.5*Psi(i,j)^-0.5;
188             firsthalf(i,j) = 0.5*Psi(i,j)^-0.5;
189         else
190             alph(i,j) = 0.5*Psi(i,j)^-0.25;
191             secondhalf(i,j) = 0.5*Psi(i,j)^-0.5;
192         end
193         fz(i,j) = alph(i,j)*c_u(j);
194         tau_ult_force(i,j) = fz(i,j)*pi*(Dout+Din)*eleSize;
195         tau_ult_calibration(i,j) = fz(i,j);
196     end
197 end
198 tau_ult_force = flip(tau_ult_force);
199 tau_ult_calibration = flip(tau_ult_calibration);
200 ultimate_capacity = sum(tau_ult_force);
201
202 z50 = zeros(nNodeEmbed,length(c_u));
203 for i = 1:length(c_u)
204     z50(:,i) = tau_ult_calibration(:,i)/kf_clay(i);
205 end
206
207 % k_clay = 1e6*[20; 37.5; 50; 75; 90; 100]; % Need to determine proper values for k_clay
208 % for i = 1:length(c_u)
209 %     z50(:,i) = tau_ult_calibration(:,i)/k_clay(i);
210 % end
211 % Literature to determine k_clay, also check mosher
212
213 % From the following paper: E_u50 = 1e6*[ ,6.0 ,7.4]
214 % cu = [30.7, 56.0, 107.1, 185.6, 218.7, 329.8, 531.3];
215 % Eu50 = [4.0, 5.7, 6.0, 6.3, 6.6, 7.4, 16.7];
216 % Eu50new = interp1(cu,Eu50,150e3);

```

```

217 % ...
      https://www.semanticscholar.org/paper/The-elastic-undrained-modulus-Eu50-for-stiff-clays-Str%C3%B3
218 % ...
      https://www.researchgate.net/publication/331304290_Shear_Modulus_of_Compacted_Sandy_Clay_from_Vari
219 % https://www.fhwa.dot.gov/publications/research/infrastructure/structures/04043/07.cfm
220 end
221
222 function Create_Elements(fID4)
223
224 parameters
225 mass = rhos*A*eleSize;
226
227 %element elasticBeamColumn $eleTag $iNode $jNode $A $E $G $J $Iy $Iz $transfTag ...
      <-mass $massDens> <-cMass>
228 for i = 1:(nNodePile-1)
229     fprintf(fID4,'element elasticBeamColumn %i %i %i %.4f %.2f %.2f %.5f %.5f %.5f %i ...
      -mass %.4f -cmass \n', i, 20000+i, 20001+i, A, E, G, Iz, Ix, Iy, l, mass);
230 end
231
232 end
233
234 function Loading(fID4)
235
236 parameters
237
238 %% Apply a gravity load
239
240 nodal_gravity = 9.81*(A*rhos*(L1+L2))/nNodePile;
241
242 tag = 1;
243 fprintf(fID4,'pattern Plain %i Linear { \n', tag);
244 for i = 1:nNodePile
245     fprintf(fID4,'load %i 0.0 0.0 %.6f 0.0 0.0 0.0 \n', 20000+i, -nodal_gravity);
246 end
247 fprintf(fID4, ' } \n');
248
249 % Perform static gravity analysis
250 fprintf(fID4, 'constraints Plain \n');
251 fprintf(fID4, 'numberer Plain \n');
252 fprintf(fID4, 'system BandGeneral \n');
253 fprintf(fID4, 'test NormDispIncr 1.0e-8 6 0 \n');
254 fprintf(fID4, 'algorithm Newton \n');
255 fprintf(fID4, 'integrator LoadControl 0.001 \n');
256 fprintf(fID4, 'analysis Static \n');
257 fprintf(fID4, 'analyze 1000 \n \n');
258
259 % Reset time and keep load constant
260 fprintf(fID4, 'loadConst -time 0.0 \n');
261 fprintf(fID4, 'wipeAnalysis \n');
262 fprintf(fID4, 'puts "gravity analysis complete" \n \n \n');
263
264 %% Apply the sinusoidal extraction load
265 steps = 100000; % How many steps the Transient analysis will ...
      make
266 stepsize = 0.01; % Stepsize of those steps
267 analysis_time = steps*stepsize; % Resulting analysis time in OpenSees
268 tag2 = 2;
269 tag3 = 3;
270
271 addpath('../Vessel_Mass_DOF_system/')
272 Hydrodynamical_model_3DOF
273 cranemaster_force = fopen('cranemasternew.tcl','w');
274 for i = 1:length(y_resulting)
275     fprintf(cranemaster_force,'%3f \n', y_resulting(i));
276 end
277
278 %%% Cranemaster force
279 % timeSeries Path $tag -dt $dt -filePath $filePath <-factor $cFactor>
280 fprintf(fID4, 'timeSeries Path %i -dt %.5f -filePath cranemasternew.tcl -factor 1.0 ...
      \n', tag2, (1+analysis_time)/length(y_resulting)); % timestep must allow ...
      cranemasternew.tcl to go to 100 seconds.

```

```

281
282 %%% Standard sine loading
283 % Sine_Loading
284 % fprintf(fID4, 'timeSeries Path 2 -dt %.5f -filePath Sine_Loading.tcl -factor 1.0 ...
    \n', timestep);
285 %
    pattern Plain $patternTag $tsTag <-fact $cFactor>
286
287 %%% Constant load
288 % timestep = 0.01; time = 0:timestep:1000; cos_mean = 180E6; w_sin = 2*pi/40; rampup ...
    = (cos_mean)*sin(w_sin*time);
289 % [peak_value_rampup, peak_index_rampup] = findpeaks(rampup);
290 % constant_force = ones(1,length(time)-peak_index_rampup(1))*180e6;
291 % y_resulting = [rampup(1:peak_index_rampup(1)) constant_force];
292 %
293 % % Make last 40% of force go to 0
294 % % rest_zero = zeros(1,floor(0.4*length(y_resulting)+1));
295 % % y_resulting = [y_resulting(1:floor(0.6*length(y_resulting))) rest_zero];
296 %
297 % constant_force = fopen('constantforce.tcl','w');
298 % for i = 1:length(y_resulting)
299 %     fprintf(constant_force,'%0.3f \n', y_resulting(i));
300 % end
301 % fprintf(fID4, 'timeSeries Path %i -dt %.5f -filePath constantforce.tcl -factor 1.0 ...
    \n', tag2, (1+analysis_time)/length(y_resulting));
302
303 %%% Apply the load, arbitrary if you choose constant, standard sinusoidal or cranemaster
304 fprintf(fID4, 'pattern Plain %i %i -fact 1.0 { \n', tag3, tag2);
305 fprintf(fID4, 'load %i 0.0 0.0 1.0 0.0 0.0 0.0 \n } \n \n', 20000+nNodePile);
306
307 % Analyze Transient analysis
308 fprintf(fID4, 'constraints Transformation \n');
309 fprintf(fID4, 'numberer RCM \n');
310 fprintf(fID4, 'system SparseGeneral \n');
311 fprintf(fID4, 'test NormDispIncr 1.0e-5 200 0 \n');
312 fprintf(fID4, 'algorithm Newton \n');
313 fprintf(fID4, 'integrator HHT 0.67 \n');
314
315 fprintf(fID4, 'analysis Transient \n');
316 fprintf(fID4, 'set startT [clock seconds] \n');
317 fprintf(fID4, 'analyze %i %.5f \n \n', steps, stepsize);
318 fprintf(fID4, 'set endT [clock seconds] \n');
319 fprintf(fID4, 'puts "Transient analysis execution time: [expr $endT-$startT] ...
    seconds." \n');
320
321 % VariableTransient
322 % fprintf(fID4, 'analysis VariableTransient \n');
323 % fprintf(fID4, 'set startT [clock seconds] \n');
324 % fprintf(fID4, ['analyze %i %.5f 0.001 0.01 5 \n \n'], steps, stepsize);
325 % fprintf(fID4, 'set endT [clock seconds] \n');
326 % fprintf(fID4, 'puts "VariableTransient analysis execution time: [expr ...
    $endT-$startT] seconds." \n');
327
328 % Analyze Static analysis
329 % fprintf(fID4, 'integrator LoadControl 0.05 \n');
330 % fprintf(fID4, 'constraints Transformation \n');
331 % fprintf(fID4, 'test NormDispIncr 1e-5 50 1 \n');
332 % fprintf(fID4, 'algorithm Newton \n');
333 % fprintf(fID4, 'numberer RCM \n');
334 % fprintf(fID4, 'system SparseGeneral \n');
335 % fprintf(fID4, 'analysis Static \n');
336 % fprintf(fID4, 'analyze 800');
337
338 fprintf(fID4, 'wipeAnalysis \n');
339
340 end
341
342
343 % load data
344 element_force = importdata("allforce.out"); % Imports force in elements
345 colsWithZeros = any(element_force==0); % Selects columns with zeros
346 element_force = element_force(:, ~colsWithZeros); % deletes the columns with zeros

```

```

347
348 node_disp = importdata("allnodedisp.out");           % Imports node displacement data
349
350 zerolength_force = importdata("zeroforce.out");
351 colsWithZeros = any(zerolength_force==0);           % Selects columns with zeros
352 zerolength_force = zerolength_force(:, ~colsWithZeros); % deletes the columns ...
    with zeros
353
354 % element force vs time
355 figure()
356 plot(element_force(:,1),element_force(:,end)/1000000)
357 hold on
358 title('force measured in upper elastic element');
359 xlabel('time (s)')
360 ylabel('Force (MN)')
361 grid on
362 hold on
363 yline(198.4,'-or','LineWidth',2)
364 txt = 't_{ult}';
365 text(39,192,txt)
366 % axis([0 100 0 100])
367 % yline(42.5,'-or','LineWidth',2)
368 % txt2 = 'tension';
369 % text(1,45,txt2)
370
371
372 % Select smallest dataset
373 [r_disp, c_disp] = size(node_disp); [r_force, c_force] = size(element_force);
374 n = min(r_disp,r_force); c = min(c_disp,c_force);
375
376 % node displacement vs time
377 figure
378 plot(node_disp(1:n,1),node_disp(1:n,end))
379 title('displacement of top node vs time')
380 xlabel('time (s)')
381 ylabel('displacement (m)')
382 grid on
383
384 % force vs displacement
385 figure
386 plot(node_disp(1:n,end),element_force(1:n,end)/1e6)
387 title('element force vs topnode displacement')
388 xlabel('topnode displacement (m)')
389 ylabel('element force (MN)')
390 grid on
391
392 % ZeroLength element force
393 % figure
394 % plot(zerolength_force(:,1),zerolength_force(:,end))
395 % title('force in topmost zerolength element')
396 % hold on
397 % plot(zerolength_force(:,1),zerolength_force(:,3))
398 % legend('top element','bottom element')
399
400 total_spring_force = zerolength_force(end,2:end);
401 total_spring_force = sum(total_spring_force(total_spring_force>0))/1e6

```

Bibliography

- [1] EDF-renouvelables, “Saint-Nazaire offshore wind farm : France’s first offshore wind turbine has been erected,” 4 2022. [Online]. Available: <https://www.edf-renouvelables.com/en/saint-nazaire-offshore-wind-farm-frances-first-offshore-wind-turbine-has-been-erected/>
- [2] L. Ziegler, E. Gonzalez, T. Rubert, U. Smolka, and J. J. Melero, “Lifetime extension of onshore wind turbines: A review covering Germany, Spain, Denmark, and the UK,” pp. 1261–1271, 2 2018.
- [3] Offshore wind farm database, “4C Offshore,” 12 2021.
- [4] ISO, “Geotechnical investigation and testing, identification and classification of soil,” International Standardization Organization, Tech. Rep., 2017. [Online]. Available: [www.sis.se.Buytheentirestandardviahttps://www.sis.se/std-80000191](http://www.sis.se/Buytheentirestandardviahttps://www.sis.se/std-80000191)
- [5] J. Liu, Y. Liang, and L. Cao, “Statistical Correlations between SPT N-Values and Soil Parameters,” Technical University Delft, Tech. Rep., 2015. [Online]. Available: <https://www.researchgate.net/publication/281109498>
- [6] J. Vugts, Handbook of bottom founded offshore structures part 2, 1st ed. Delft: Eburon, 2016.
- [7] API, “Recommended Practice for Planning, Designing and Constructing Fixed Offshore Platforms API RECOMMENDED PRACTICE 2A-WSD (RP 2A-WSD),” American Petroleum Institute, Tech. Rep., 2007.
- [8] ISO, “International Standardization Organisation 19902,” International Standardization Organization, Tech. Rep., 2007.
- [9] DNV GL, “DNVGL-ST-0378 Standard for offshore and platform lifting appliances,” Det Norske Veritas, Tech. Rep., 2016. [Online]. Available: <http://www.dnvgl.com>,
- [10] L. R. Mosher, “Load-transfer criteria for numerical analysis of axially loaded piles in sand,” U.S. Army, Tech. Rep., 1984.
- [11] GEO5, “Secant Modulus of Soil Es,” 2022. [Online]. Available: <https://www.finesoftware.eu/help/geo5/en/secant-modulus-of-soil-es-02/>
- [12] “OpenSees,” 5 2022. [Online]. Available: <https://opensees.berkeley.edu/>
- [13] “WindEurope,” 2 2022.
- [14] E. Topham, E. Gonzalez, D. McMillan, and E. João, “Challenges of decommissioning offshore wind farms: Overview of the European experience,” in Journal of Physics: Conference Series, vol. 1222, no. 1. Institute of Physics Publishing, 5 2019.
- [15] L. Arany, S. Bhattacharya, J. Macdonald, and S. J. Hogan, “Design of monopiles for offshore wind turbines in 10 steps,” Soil Dynamics and Earthquake Engineering, vol. 92, pp. 126–152, 1 2017.
- [16] G. Smith, C. G. Det, and N. Veritas, “Logistics and Cost Reduction of Decommissioning Offshore Wind Farms Offshore wind decommissioning View project Wind farm wakes View project,” DNV-GL, Tech. Rep., 2018. [Online]. Available: <https://www.researchgate.net/publication/274896458>
- [17] E. Topham and D. McMillan, “Sustainable decommissioning of an offshore wind farm,” Renewable Energy, vol. 102, pp. 470–480, 3 2017.
- [18] J. Breukels, J. Gruijters, B. Yenigul, N. Mallon, A. Skinner, and M. Dijk, “Allseas Engineering,” 2022.
- [19] Wout Stapel, “Graduation_Thesis_Entire_Monopile_Removal_Wout_Stapel_Repository,” Ph.D. dissertation, Delft university of technology, Delft, 2019.

- [20] N. Hinzmann, P. Lehn, and J. Gattermann, "Large-scale model investigation for monopile decommissioning of offshore wind turbines - Overpressure and vibratory pile," Technische Universität Braunschweig, Tech. Rep., 2020.
- [21] "Balltec LiftLOK," 8 2022. [Online]. Available: <https://www.balltec.com/solutions/balltec-lifting-solutions-tools/4-liftlok/>
- [22] "Righini Lifting Tools," 8 2022. [Online]. Available: <https://www.righiniravenna.it/soluzioni/internal-lifting-tools/>
- [23] Mente Baak, "Cranemaster ," 2022. [Online]. Available: <https://www.cranemaster.com/units/?load-range=4-1200>
- [24] F. Elekes and E. J. Parteli, "An expression for the angle of repose of dry cohesive granular materials on Earth and in planetary environments," Proceedings of the National Academy of Sciences of the United States of America, vol. 118, no. 38, 9 2021.
- [25] W. David and C. Mark, Offshore Geotechnical Engineering. CRC Press, 7 2017.
- [26] C. H. Tsuha, P. Y. Foray, R. J. Jardine, Z. X. Yang, M. Silva, and S. Rimoy, "Behaviour of displacement piles in sand under cyclic axial loading," Soils and Foundations, vol. 52, no. 3, pp. 393–410, 2012.
- [27] "Settlement of single pile foundations," 9 2022. [Online]. Available: https://ebrary.net/203324/engineering/settlement_single_pile_foundations
- [28] J. M. J. Journée and W. W. Massie, Offshore Hydromechanics First Edition. TU Delft, 2016.
- [29] R. W. Boulanger, C. J. Curras, B. L. Kutter, D. W. Wilson, and A. Abghari, "Seismic Soil-Pile-Structure Interaction Experiments and Analyses," Journal of Geotechnical and Geoenvironmental Engineering, vol. 125, no. 9, pp. 750–759, 9 1999.
- [30] T. W. Blad, D. Farhadi Machekposhti, J. L. Herder, and N. Tolou, "Design of a Motion Energy Harvester based on Compliant Mechanisms: a Bi-stable Frequency Up-converter Generator," in Mechanisms and Machine Science, vol. 73. Springer Science and Business Media B.V., 2019, pp. 1619–1626.
- [31] a.u., "Comparison of impact versus vibratory drive piles: With a focus on soil-structure interaction," Deep foundations institute, Tech. Rep., 2022.
- [32] R. Redondo and A. Mehmanparast, "Numerical analysis of stress distribution in offshore wind turbine m72 bolted connections," Metals, vol. 10, no. 5, 5 2020.
- [33] N. I. Tziavos, H. Hemida, N. Metje, and C. Baniotopoulos, "Grouted connections on offshore wind turbines: A review," Proceedings of the Institution of Civil Engineers: Engineering and Computational Mechanics, vol. 169, no. 4, pp. 183–195, 12 2016.
- [34] D. Norske Veritas, "DET NORSKE VERITAS AS Design of Offshore Wind Turbine Structures," Det Norske Veritas, Tech. Rep., 2014. [Online]. Available: www.dnvgl.com.
- [35] KCI, "Double Slip Joint Innovative Pile Connection," KCI consortium, Tech. Rep., 2018. [Online]. Available: www.kci.nl
- [36] K. E. Y. Creusen, G. Misios, J. S. Winkes, and M. Veljkovic, "Introducing the C1 Wedge Connection," Steel Construction, 1 2022.
- [37] DNV GL, "RECOMMENDED PRACTICE DNV-GL-AS Corrosion protection for wind turbines," Det Norske Veritas, Tech. Rep., 2016. [Online]. Available: <http://www.dnvgl.com>
- [38] T. Hague, "Climate Agreement," Dutch government, Tech. Rep., 2019.
- [39] L. Boogaart, "Early age cycling in the grout connection of an offshore wind jacket structure," Technical University Delft, Tech. Rep., 2020.
- [40] "NEN-EN-IEC 61400-1: Wind turbines - Design requirements," 2019.

- [41] Bart Ummels, "Expert interview," Delft, 12 2021.
- [42] Y. E. Liu, "Monopile Forever Overcoming the Technical Boundaries of Monopile Foundations in Deep Waters," Technical University Delft, Tech. Rep., 2021. [Online]. Available: <http://repository.tudelft.nl/>.
- [43] K. W. Hermans and J. M. Peeringa, "Future XL monopile foundation design for a 10 MW wind turbine in deep water," ECN, Tech. Rep., 2016.
- [44] G. Smith, "Decommissioning of Offshore Wind Installations - What we can learn," Det Norske Veritas, Tech. Rep., 2017. [Online]. Available: <https://www.researchgate.net/publication/318340068>
- [45] M. M. Luengo and A. Kolios, "Failure mode identification and end of life scenarios of offshore wind turbines: A review," pp. 8339–8354, 8 2015.
- [46] Dutch Government, "Borssele Wind Farm Zone Wind Farm Sites I and II Appendix A: Applicable Law Part of Project and Site Description," Dutch department of energy, Tech. Rep., 2016.
- [47] E. Topham, D. McMillan, S. Bradley, and E. Hart, "Recycling offshore wind farms at decommissioning stage," *Energy Policy*, vol. 129, pp. 698–709, 6 2019.
- [48] T. Adedipe and M. Shafiee, "An economic assessment framework for decommissioning of offshore wind farms using a cost breakdown structure," *International Journal of Life Cycle Assessment*, vol. 26, no. 2, pp. 344–370, 2 2021.
- [49] S. Walker, "Environmentally acceptable lubricants: Looking beyond the label," ExxonMobil, Tech. Rep., 2019.
- [50] Jan Gruijters, "Expert interview," 2022.
- [51] Ron van Wachem, "Finding the Ideal Biodegradable Marine Lubricant," 1 2014. [Online]. Available: <https://www.marinelink.com/news/biodegradable-lubricant362785>
- [52] C. Simons Januário, S. Semino, C. Januário, and M. Bell, "Offshore Windfarm Decommissioning: A proposal for guidelines to be included in the European Maritime Policy," Roskilde University, Tech. Rep., 2007. [Online]. Available: <https://www.researchgate.net/publication/228636135>
- [53] UNCLOS, "UNCLOS: Oceans and law of the sea Division for Ocean affair and the law of the sea." 12 2021. [Online]. Available: https://www.un.org/depts/los/reference_files/chronological_lists_of_ratifications.htm
- [54] —, "United Nations Convention on the Law of the Sea," United Nations, Tech. Rep., 1985.
- [55] IMO, "1989 Guidelines and standards for the removal of offshore installations and structures on the continental shelf and in the exclusive economic zone (IMO resolution A.672 (16))," International Maritime Organization, Tech. Rep., 1989. [Online]. Available: www.cil.nus.edu.sg
- [56] Orsted, "Decommissioning Programme Horn sea II," Orsted, Tech. Rep., 2015.
- [57] "Decommissioning programme greater gabbard offshore wind farm project," Tech. Rep., 2007.
- [58] Scira offshore energy, "Sheringham shoal offshore windfarm," Tech. Rep., 2014.
- [59] Dong energy, "Lincs offshore wind farm decommissioning plan," Tech. Rep., 2010.
- [60] OSPAR Commission, "OSPAR Guidance on Environmental Considerations for Offshore Wind Farm Development," OSPAR, Tech. Rep., 2008.
- [61] OSPAR, "98-03e decision disposal of disused offshore installations," OSPAR, Tech. Rep., 1998.
- [62] R. Q. Schothorst, "Buoyancy Lifting of Offshore Platform Jackets Modelling the economic viability of early stage concept designs," Technical University Delft, Tech. Rep., 2018. [Online]. Available: <http://repository.tudelft.nl/>.

- [63] e. BEIS (business and industrial strategy department UK), "Decommissioning of offshore renewable energy installations under the energy act 2004," Tech. Rep., 2019.
- [64] TNO, "Offshore wind farm decommissioning, an orientation of possible economic activity in the South-Holland region and the Rotterdam port area," Tech. Rep., 2020. [Online]. Available: www.smartport.nl
- [65] M. Kaiser and B. Snyder, "Offshore Wind Energy Installation and Decommissioning Cost Estimation in the U.S. Outer Continental Shelf," Tech. Rep., 2010. [Online]. Available: <http://www.mms.gov/tarprojects/>.
- [66] "Offshore Renewable Energy Installation Decommissioning Study," Tech. Rep., 2006.
- [67] "Price History Tables and Charts USA China Western Europe World Export," Tech. Rep. [Online]. Available: www.steelbenchmarker.com
- [68] Allan Skinner, "Expert interview," 2022.
- [69] N. Hinzmann, P. Stein, and J. Gattermann, "Decommissioning of offshore monopiles, occurring problems and alternative solutions," Technische Universität Brunschweig, Tech. Rep., 2018.
- [70] N. Hinzmann and P. Stein, "Measurements of hydro sound emissions during internal jet cutting during monopile decommissioning," Technische Universität Brunschweig, Tech. Rep., 2017. [Online]. Available: <https://www.researchgate.net/publication/322986958>
- [71] H. Askari, A. Halimah, M. Bentin, and S. Kotzur, "Decom Tools Vessel Design," Tech. Rep., 2021.
- [72] A. Cabboi, T. Kamphuis, E. van Veldhuizen, M. Segeren, and H. Hendrikse, "Vibration-assisted decommissioning of a slip joint: Application to an offshore wind turbine," *Marine Structures*, vol. 76, p. 102931, 3 2021.
- [73] B. Nielsen, "Feasibility Study of the Complete Removal of Monopiles Using Vibratory Pile Removal," Tech. Rep., 2022.
- [74] N. Bijkersma, "Grow Consortium - HyPE-ST," 12 2019. [Online]. Available: <https://grow-offshorewind.nl/project/hype-st>
- [75] Z. Jiang, "Installation of offshore wind turbines: A technical review," 4 2021.
- [76] R. Kikuchi, "Risk formulation for the sonic effects of offshore wind farms on fish in the EU region," *Marine Pollution Bulletin*, vol. 60, no. 2, pp. 172–177, 2 2010.
- [77] Maxim Segeren, "Gentle Driving of Piles progress presentation," 12 2019. [Online]. Available: <https://grow-offshorewind.nl/files/downloads/gdp-grow-side-event-winddays-2019-gentle-driving-of-piles.pdf>
- [78] A. Metrikine and M. Segeren, "GROW Consortium - Gentle Driving of Piles," 2 2022. [Online]. Available: <https://www.grow-offshorewind.nl/project/gentle-driving-of-piles>
- [79] R. J. Jardine, J. R. Standing, and F. C. Chow, "Some observations of the effects of time on the capacity of piles driven in sand," Imperial college, Tech. Rep. 4, 2006.
- [80] D. Fu, Y. Zhang, K. K. Aamodt, and Y. Yan, "A multi-spring model for monopile analysis in soft clays," *Marine Structures*, vol. 72, 7 2020.
- [81] K. Gavin, R. Jardine, K. Kartsrud, and B. M. Lehane, "Effects of pile ageing on shaft capacity in sand," in *Frontiers in Offshore Geotechnics III*. CRC Press, 5 2015, pp. 792–852. [Online]. Available: <https://www.taylorfrancis.com/books/9781315675510/chapters/10.1201/b18442-8>
- [82] Yenigul Buket, "Expert interview," 2022.
- [83] M. Y. Fattah, W. H. S. Al-Soudani, M. Y. Fattah1, and W. H. S. Al-Soudani2, "Bearing Capacity of Closed and Open Ended Pipe Piles Installed in Loose Sand with Emphasis on Soil Plug," Tech. Rep. 5, 2014. [Online]. Available: <https://www.researchgate.net/publication/266273656>

- [84] V. Karlowskis, "Soil Plugging of Open-Ended Piles During Impact Driving in Cohesion-less Soil," Tech. Rep., 2014.
- [85] F. Chen, Y. Lin, Y. Dong, and D. Li, "Numerical investigations of soil plugging effect inside large-diameter, open-ended wind turbine monopiles driven by vibratory hammers," *Marine Georesources and Geotechnology*, vol. 38, no. 1, pp. 83–96, 1 2020.
- [86] DNV GL, "STANDARD DNV-GL-AS Support structures for wind turbines," Det Norske Veritas, Tech. Rep., 2016. [Online]. Available: www.dnvgl.com.
- [87] Lloyd's, "Code for Lifting Appliances in a Marine Environment A guide to the Rules and published requirements Code for Lifting Appliances in a Marine Environment," Tech. Rep., 2019. [Online]. Available: <http://www.lr.org/entities>
- [88] W. Hu, "Cyclic axial behaviour of piles in sand: 3D FE modelling using SANISAND-MS," Tech. Rep., 2021.
- [89] H. G. Poulos, "Influence of cyclic loading on axial pile response," Tech. Rep.
- [90] Rob Eijkens, "Expert interview," 2022.
- [91] T. Wichtmann, A. Niemunis, and T. Triantafyllidis, "Strain accumulation in sand due to cyclic loading: Drained triaxial tests," *Soil Dynamics and Earthquake Engineering*, vol. 25, no. 12, pp. 967–979, 12 2005.
- [92] D. S. Stutts, "Analytical Dynamics: Lagrange's Equation and its Application-A Brief Introduction," Tech. Rep., 2011.
- [93] R. Van Der Valk, "Hoist and boom wire dynamics during offshore heavy lifting," Tech. Rep., 2017. [Online]. Available: <http://repository.tudelft.nl>.
- [94] M. Raoof and T. J. Davies, "Simple determination of the axial stiffness for large diameter independent wire rope core or fibre core wire ropes," Tech. Rep., 2003. [Online]. Available: <https://dspace.lboro.ac.uk/>
- [95] Maarten van den Berg, "Limits of Offshore Wind Turbine Installation with the Double Slip Joint," Ph.D. dissertation, 2020.
- [96] K. Feyrer, *Wire Ropes*, Stuttgart, 2007.
- [97] "Some Dynamic Properties of Axially Loaded Wire Ropes List of Symbols," Tech. Rep.
- [98] C. McGann and P. Arduino, "Laterally-Loaded Pile Foundation OpenSees Example," 3 2011. [Online]. Available: https://opensees.berkeley.edu/wiki/index.php/Laterally-Loaded_Pile_Foundation
- [99] "TzSimple1 Material, OpenSees," Tech. Rep.
- [100] M. O'Neil and L. Reese, "Drilled shafts: construction procedures and design methods," Office of infrastructure, Washington, Tech. Rep., 8 1999.
- [101] S. Kontoe, L. Zdravkovic, and D. M. Potts, "An assessment of time integration schemes for dynamic geotechnical problems," *Computers and Geotechnics*, vol. 35, no. 2, pp. 253–264, 3 2008.
- [102] N. Higham, *Accuracy and stability of numerical algorithms*, 1996, vol. 1.
- [103] W. M. Hassan, "Numerical error assessment in nonlinear dynamic analysis of structures," *HBRC Journal*, vol. 15, no. 1, pp. 1–31, 1 2019.
- [104] G. Mylonakis, G. E. Mylonakis, and C. Syngros, "Role of Soil Inhomogeneity in Pile Radiation Damping for SSI Applications," University of Bristol, Tech. Rep., 2008. [Online]. Available: <https://www.researchgate.net/publication/255607272>
- [105] R. Bruijne de, "Geological Ground Model Wind Farm Site I Hollandse Kust (zuid) Wind Farm Zone," Netherlands Enterprise Agency, Tech. Rep., 2018.

- [106] E. Kementzetzidis, F. Pisanò, and A. V. Metrikine, "A memory-enhanced p-y model for piles in sand accounting for cyclic ratcheting and gapping effects," *Computers and Geotechnics*, vol. 148, 8 2022.
- [107] T. Blad, "Challenge the future," Tech. Rep., 2019.
- [108] J. M. Sinke, "A probabilistic approach to sheet pile driveability predictions by vibro hammers," Tech. Rep. [Online]. Available: <http://repository.tudelft.nl/>.
- [109] Noordzeewind, "NUON Shell_201011_Operations report 2009," 2009.
- [110] G. Rajgor, "Offshore wind: Solid foundations for the future," 2012. [Online]. Available: <https://www.reutersevents.com/renewables/wind-energy-update/offshore-wind-solid-foundations-future>
- [111] K. S. Jensen, S. J. Petersen, and R. R. Pedersen, "European offshore wind engineering - Past, present and future," in *Proceedings of the Institution of Civil Engineers: Civil Engineering*, vol. 171, no. 4. ICE Publishing, 5 2018, pp. 159–165.
- [112] E. Reid, A. Rodger, and K. Taylor, "Disclaimer PROJECT 14020777-Spirit Energy-Morecambe Bay DP3 & DP4 Platforms-Grouted Lift Points Rev Description Original Review Worley Approval Revision Date Approval Date," Tech. Rep.
- [113] P. Dallyn, A. El-Hamalawi, A. Palmeri, and R. Knight, "Experimental testing of grouted connections for offshore substructures: A critical review," pp. 90–108, 8 2015.
- [114] J. Van der Tempel, "World's first full-sized submerged Slip Joint successfully installed," 12 2019. [Online]. Available: <https://grow-offshorewind.nl/project/sjor>
- [115] N.-E. O. Hansen, "Copenhagen Offshore Wind 2005 Experiences with simple and repetitive Offshore Foundations Topic: Offshore technology for wind energy application Subtopic: Foundation concepts-Series production, installation concepts and risks," Tech. Rep., 2005.
- [116] W. Khodabux, P. Causon, and F. Brennan, "Profiling corrosion rates for offshorewind turbines with depth in the North Sea," *Energies*, vol. 13, no. 10, 5 2020.
- [117] A. R. Black, L. R. Hilbert, A. R. Black, and F. Andersen, "Inspection and monitoring of corrosion inside monopile foundations for offshore wind turbines," Tech. Rep., 2011. [Online]. Available: <https://www.researchgate.net/publication/289631932>